Effect of Cyclic Deformation on the Corrosion of Coated AA6xxx Hem Flanges

Effect of Cyclic Deformation on the Corrosion of Coated AA6xxx Hem Flanges

BY SHIQI ZHENG, B. S.

A Thesis

Submitted to the Department of Materials Science & Engineering

and the School of Graduate Studies

in Partial Fulfilment of the Requirements

for the Degree

Master of Science

McMaster University

Master of Science (2016) McMaster University

(Materials Science & Engineering) Hamilton, Ontario, Canada

TITLE:	Effect of Cyclic Deformation on the Corrosion of Coated AA6xxx Hem Flanges
AUTHOR:	Shiqi Zheng, B. S.
SUPERVISORS:	Dr. Joseph R. Kish, Dr. Joseph R. McDermid
NUMBER OF PAGES:	153

Abstract

The cyclic corrosion and cyclic deformation behaviour of AA6022 and AA6111 coated automotive hem flanges were investigated. Neutron radiography, in conjunction with a gadolinium (III) nitrate ($Gd(NO_3)_3$) solution, was used to reveal the existence of an interconnected network of pores within the adhesive layer of the hem flange coupons. Cyclic corrosion tests revealed that the inner compressive surface of the outer sheet (area B) was the weak link in the corrosion resistance of a hem flange due to the high degree of plastic deformation combined with micro-cracking present in this area. Cyclic deformation test revealed that cyclic deformation caused cracking in the adhesive layer and subsequent loss of load bearing ability. The cyclic deformation of pre-exposed hem flange coupons showed that cyclic corrosion exposure resulted in adhesive embrittlement and an earlier initiation of cracking in the adhesive layer. The current evidence was not enough to demonstrate that the corrosion resistance of a hem flange coupon is altered by the damage accumulated during cyclic deformation. An imposed low-level static stress on pre-cracked hem flange coupons was found to have a synergistic effect with the cyclic corrosion environment and resulted in adhesive failure at the adhesive-metal interface, thereby exposing new sites for corrosion.

Acknowledgments

Before I started this work, I thought I was mentally and physically prepared for it. But I was wrong. In reality, the research work was an arduous endeavour, more arduous than I thought it would be. It was with the patient guidance and the expert instruction of Dr. Joseph Kish and Dr. Joseph McDermid that I was able to complete the task at hand. For this, I owe them the first and foremost gratitude. Dr. Kish and Dr. McDermid are flexible supervisors, who allowed me a great deal of latitude during the progression of my work. They also provided numerous opportunities for me to attend conferences and connect with other peer researchers around the world. My gratitude also goes to the colleagues in the Centre for Automotive Materials and Corrosion (CAMC) of the Department of Materials. They were helpful resources to my work as well as friendly companions to my social life. I would like to thank Joy Forsmark, Thomas Norton, and Niamh Hosking from Ford Motor Company. Ford provided funding to this work and periodic technical suggestions.

Many other people provided valuable assistance to this work. Josh Venderstelt from Nray inc. carried out all the neutron radiography work in McMaster Nuclear Reactor. The data he generated were instrumental to this work. Mike Bruhis, senior research engineer of CAMC group, was responsible for countless technical assistance in conducting the experiment and designing custom made parts. Connie Barry, research manager of CAMC group, provided valuable help in the daily operation of the labs and purchasing all the chemicals used in this work. Xiaogang Li and Doug Cully from MSE department provided routine

help whenever my work was conducted in their labs. A special thank goes to Kazi Badhon, who is a good friend of mine.

Finally, I would like to thank my parents. The supported my education financially and emotionally since I left home and started my bachelor's degree in the U.S.. Their support allowed me to pursue my goal without worrying the future.

Abbreviations and Symbols

List of Abbreviations

AA	**A**luminum **A**lloy
ACF	**A**dhesive **C**overage **F**raction
CT	**C**omputed **T**omography
EDS	**E**nergy **D**ispersive X-ray **S**pectrometer/**S**pectroscopy
FFC	**F**ili**f**orm **C**orrosion
GHG	**G**reen**h**ouse **G**as
ICP-OES	**I**nductively **C**oupled **P**lasma **O**ptical **E**mission **S**pectroscopy
LOM	**L**ight **O**ptical **M**icroscope/**M**icroscopy
NDE	**N**on-**D**estructive **E**valuation
NR	**N**eutron **R**adiography
OCC	**O**pen **C**ircuit **C**ondition
OCP	**O**pen **C**ircuit **P**otential
PBR	**P**aint-**b**ake **R**esponse
RH	**R**elative **H**umidity
SEM	**S**canning **E**lectron **M**icroscope/**M**icroscopy

List of Symbols

A	Ampere
at. %	Atomic percent
cm	Centimetre
E_b	Breakdown potential (V_{SCE})
E_{corr}	Corrosion potential (V_{SCE})
eV	Electron volt
g	Gram
h	Hour
Hz	Hertz
I	Current (A)
i	Current density (A/cm^2)
i_{corr}	Corrosion current density (A/cm^2)
keV	Kiloelectron volt
M	Mole per litre
m	Metre
min	Minute
mL	Millilitre
mm	Millimetre
mV	Millivolt
R^2	Coefficient of determination
s	Second
V	Volt
V_{SCE}	Volt versus a saturated calomel electrode
wt. %	Weight percentage
µm	Micrometre

Table of Contents

List of Tables

List of Figures

.

Chapter 1: Introduction

1.1. Aluminum Alloys in the Automotive Industry

Increased greenhouse gas (GHG) emissions due to the rising energy demand has become a global concern because of global warming. This concern has led to the formation of several international treaties aiming to curb increasing GHG emissions [1]. As a major contributor to GHG emissions, the transportation sector accounts for 26% of the total emissions in the USA, 59% of which is attributed to cars and light trucks [2]. For this reason, the transportation industry is constantly seeking new technological means to reduce its GHG emissions. One key strategy to reduce vehicular GHG emissions is by reducing the weight of automobiles through lightweight materials [3].

The low density of aluminum (Al) alloys (one-third the density of steel) makes them a promising candidate to substitute steel in automobile body structures. Over the past two decades, the use of Al alloys as a substitute for steel in the manufacture of light vehicles has seen a gradual increase: from 6% in 1995 to 10% in 2013 [2].

There are two types of Al alloys that are being used in automobile body structures: (i) non-heat-treatable solid solution alloys including the Al-Mn AA3xxx series, and Al-Mg AA5xxx series and (ii) heat-treatable precipitation-hardened alloys including the Al-Cu AA2xxx series, Al-Mg-Si AA6xxx series and Al-Zn-Mg-Cu AA7xxx series [3, 4, 5].

The heat-treatable AA6xxx series Al alloys have received considerable attention versus the other series from the automotive industry as the material of choice for auto body sheet enclosures, as shown in Figure 1.1 [6]. Despite having lower strength than the

AA2xxx and AA7xxx series Al alloys, the AA6xxx series Al alloys provide a favourable combination of cold formability, weldability, and corrosion resistance, while also providing a high surface quality [3]. Most importantly, this series can be artificially aged during the standard automotive paint-bake cycle, typically at 180°C for 30 minutes [7, 8]. Among the AA6000 series, the Cu-rich AA6111 alloy (0.7 wt. % Cu) is favoured by the North American automakers due to its high strength.

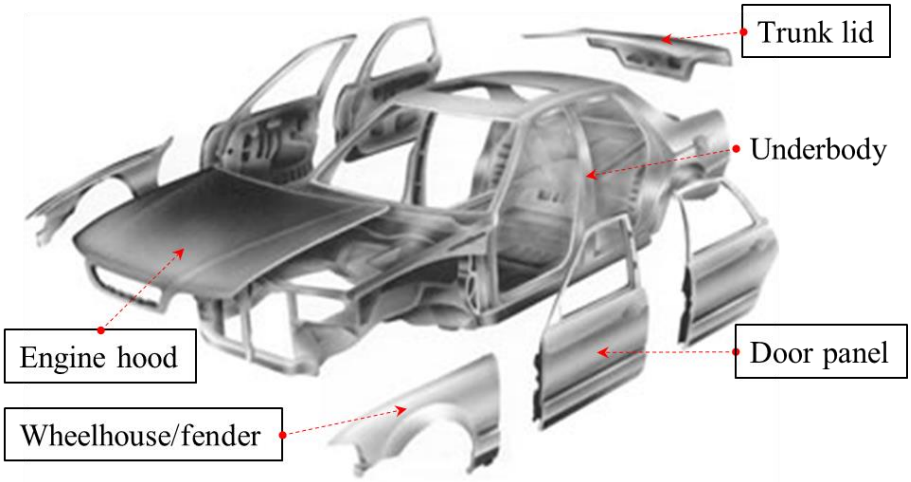

Figure 1.1: Schematic of an auto body showing the underbody and the different components of sheet enclosures including engine hood, wheelhouse, door panel, and trunk lid [9].

1.2. Adhesive Bonded Hem Flanges

Adhesive bonded hem flanges are a common component of auto body sheet enclosures and can be found on the edges of the engine hood, wheelhouse, door panels, and trunk lids [10]. An example of a door panel hem flange is shown in Figure 1.2.

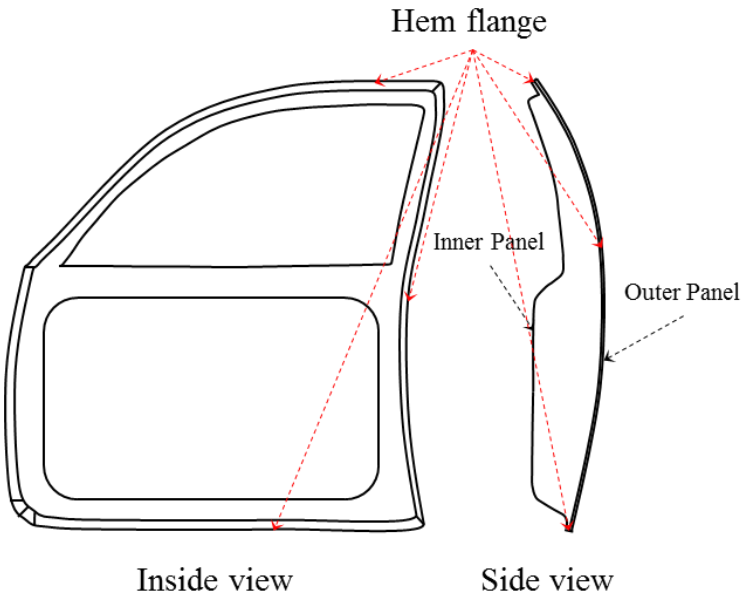

Figure 1.2: Schematics of a car door with the location of a hem flange indicated by the red arrows.

Hem flanges are manufactured in a sheet forming process in which the edge of one sheet, referred to as the outer sheet, is bent over the edge of another sheet, referred to as the inner sheet [11]. A layer of structural adhesive is applied between the inner and outer sheet in the joint area to create the mechanical bond. A generic three-step hemming operation is illustrated in Figure 1.3.

The structural adhesive layer in the hem flange is applied as a viscous liquid and is subsequently cured during the paint-bake cycle to form a solid epoxy layer that bonds the two sheets of metal together. This forms a continuous bond without the creation of localized stress concentrations, as oppose to mechanical fasteners, rivets, and resistance spot welds. Consequently, applied mechanical stresses are, in theory, distributed more uniformly across the hem flange, which is thought to increase fatigue resistance and shear strength [12, 13].

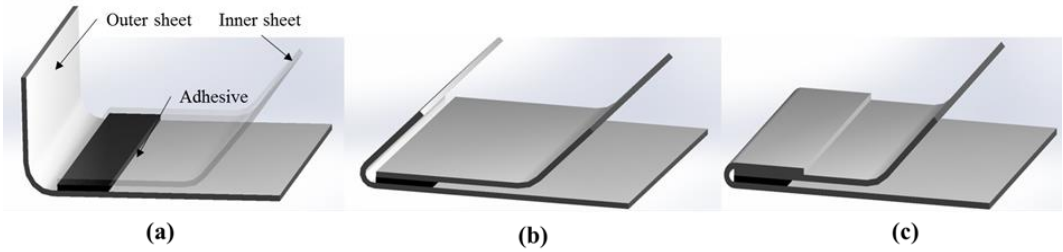

Figure 1.3: Schematics of a generic three-step hemming operation: (a) flanging, (b) pre-hemming, and (c) hemming.

1.3. Corrosion of Hem Flanges

In recent years, numerous new vehicle models featuring auto body enclosures, including hem flanges, made of aluminum alloys were introduced to the market, such as Ford “F-150”, Land Rover “Range Rover”, Tesla “Model S”, etc. [14]. The introduction of these new vehicle models raised concerns over the corrosion resistance of aluminum auto body enclosures, and by extension of aluminum hem flanges [15].

The corrosion resistance of wrought Al-Mg-Si sheet product in chloride (Cl^-) containing environments has received considerable attention. The critical factors influencing the corrosion resistance include Cu content, Mg/Si ratio, and ageing condition [16, 17, 18]. However, the corrosion resistance of Al alloy hem flanges has received significantly less attention in the literature. Nonetheless, the coated hem flanges of enclosures are susceptible to corrosion damage.

Figure 1.4 showcases an example in which blistering was found adjacent to a hem flange on the engine hood of a vehicle while the adjacent paint appeared to be intact and free from damage. Corrosion damage of this type is typical of filiform corrosion (FFC), which propagates along the metal-coating interface. FFC can embrittle the paint and, in severe cases, causes the paint to break, thereby exposing the base metal [19]. The mechanism of FFC has been studied on various coated metals, including steel, Al, Mg, etc. [19, 20, 21]. However, the mechanism of FFC on coated Al hem flanges has not been well studied.

Figure 1.4: Photograph of blistering adjacent to a hem flange on the engine hood.

Currently, there are various testing standards in place to evaluate the salt fog/spray atmospheric corrosion resistance of materials for automotive applications, for example, ASTM B117, ASTM G85, ISO 11997-1, SAE J2334, etc.. These accelerated protocols do not specifically address the effect of cyclic mechanical deformation on corrosion. As cyclic deformation, in the form of vibrations caused by road shock and routine mechanical vibrations, are indeed encountered during service, it is of interest to better understand how cyclic deformation can influence the corrosion resistance of coated adhesive bonded hem flanges and to determine whether cyclic deformation contributes to the corrosion damage similar to the one showcased in Figure 1.4. Thus, this study was focused on acquiring a better understanding of how cyclic deformation influences the localized corrosion resistance of coated Al alloys, namely AA6022 and AA6111, hem flanges subjected to cyclic salt fog exposure.

This thesis is composed of seven chapters. Chapter 2 provides a review of the relevant literature. Chapters 3 provides the research hypothesis and the detailed research objectives. Chapters 4 includes the documentation of the experimental methods used in this work. Chapter 5 provides the experimental results of this work. Chapters 6 and 7 are the interpretation of the results and final conclusion of this work.

Chapter 2: Literature Review

2.1. Corrosion of Automotive Al Alloys

2.1.1. Corrosion Environment Overview

Al alloy automotive components encounter various chemical environments during service, some of which are corrosive. Such corrosion environments include dissolved aqueous chlorides (Cl^-), sulfur oxides (SO_x), and nitrogen oxides (NO_x) [22]. Chlorides (Cl^-) are common chemical species found in urban and coastal environments that promote corrosion on various alloys, such as Al, Mg alloys, and steels [20]. In inland Canada, chlorides mostly come from the use of deicing salts (mostly NaCl and $MgCl_2$) during winter time [22]. SO_x and NO_x are both common urban air pollutants from the combustion of fossil fuel. Both acidic gases are involved in the corrosion of Al alloys primarily due to their hydrolysis reaction with various sources of water, such as humid air and rainwater, in the environment, which produce nitric acid (HNO_3) and sulfuric acid (H_2SO_4) [21, 23]. These acids, when in contact with the Al alloys, reduce the pH of their vicinity, which undermine the passivation of Al alloys and make them more vulnerable to corrosion [20, 21]. The presence of Cl^- and an oxidizing agent, such as dissolved O_2, in an aqueous environment also undermine the passivation of Al alloys, and subsequently promote localized corrosion attack [21, 24].

In order to evaluate the corrosion resistance of automotive materials, the most reliable way is to perform various field experiment, including stationary and mobile exposure,

which are time consuming and often costly. To this end, accelerated cyclic corrosion protocol was developed to obtain comparable corrosion of materials to the natural weathering conditions within a shorted time [25]. In order to mimic the corrosion environment of Al alloys in natural weathering conditions, aqueous solution containing Cl^-, sometimes combined with the addition of acid to reduce the pH, has been widely used by standards as well as by other researchers [17, 26, 27, 28].

2.1.2. Corrosion of AA6xxx in Chloride Containing Aqueous Media

2.1.2.1. Fundamentals of Corrosion for Al

The basic reaction associated with the corrosion of Al alloy is the anodic dissolution of Al as shown in Equation (2.1). When there is dissolved oxygen present, the cathodic reaction is shown in Equation (2.2), whereas the cathodic reaction without dissolved oxygen present is shown in Equation (2.3) [20].

$$Al \rightarrow Al^{3+} + 3e^- \quad (2.1)$$

$$O_2 + 2H_2O + 4e^- \rightarrow 4OH^- \quad (2.2)$$

$$2H^+ + 2e^- \rightarrow H_2 \quad (2.3)$$

The pH value of the aqueous medium plays an important role in the corrosion of Al alloy, as Al is passive in pH 4 – 8.5 and can react in either acidic or alkaline environment outside the passivation pH. The Pourbaix diagram of Al is shown in Figure 2.1 [21]. In

acidic environment (pH < 4.5), reaction (2.4) occurs, whereas in alkaline environment, reaction (2.5) occurs. In this work, the reaction that occurs in acidic environment is of interest due to the reason stated in Section 2.1.1. .

$$2Al + 6H^{+} \rightarrow 2Al^{3+} + 3H_2 \quad (2.4)$$

$$2Al + 6H_2O + 2OH^{-} \rightarrow 2Al(OH)_4^{-} + 3H_2 \quad (2.5)$$

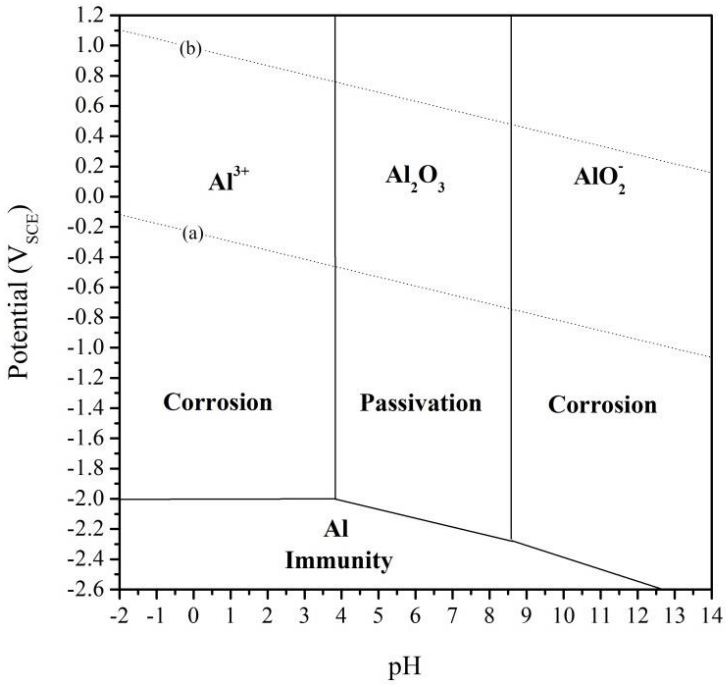

Figure 2.1: Pourbaix diagram (E-pH) of pure Al at 25°C in aqueous solution. The lines (a) and (b) correspond to water stability and its decomposed product [21].

2.1.2.2. Pitting Corrosion

Pitting Corrosion is a common form of localized corrosion for uncoated AA6xxx alloys. Pitting corrosion can happen when Al alloys are in the pH range where it is passive, pH 4 – 8.5 [21, 29, 30]. The daily use of automobile involves day-night temperature/humidity cycles and other natural weather conditions (rain, snow). As a result, chloride, and potentially other acid species, containing aqueous media are introduced onto the alloy surface during high humidity phase and evaporate during high temperature phase [21, 30].

In aerated conditions, the cathodic reaction is oxygen reduction, while the anodic reaction is Al oxidation. The rate of this process is influenced by Cl^- concentration, pH, temperature, and composition of the alloy. In the context of AA 6xxx which is a precipitation hardened alloy, the secondary phases of the alloy have significant influence of the corrosion resistance, which is explored in section 2.1.3.

The mechanism of pitting corrosion has been widely studied and reported. A recent work by Natishan et al. provides a comprehensive review on the mechanism [24]. The mechanism can be briefly summarized in the following steps:

1. Absorption and subsequent incorporation of Cl^- ions into the passive oxide film through micro-flaws.
2. Migration of Cl^- ions toward the interface between Al substrate and passive oxide film.
3. Reduction in thickness of the passive oxide film due to the interaction between Cl^- and the film.
4. Dielectric breakdown of the passive oxide film at weak points.

5. Oxidation of bare Al substrate producing soluble Al oxychloride complexes (AlOCl) at the location of the localized passive oxide film breakdown to form pits.
6. Propagation of pit due to autocatalytic processes occurring within the pit itself. [21, 24, 31]

A schematic showcasing this mechanism is shown in Figure 2.2.

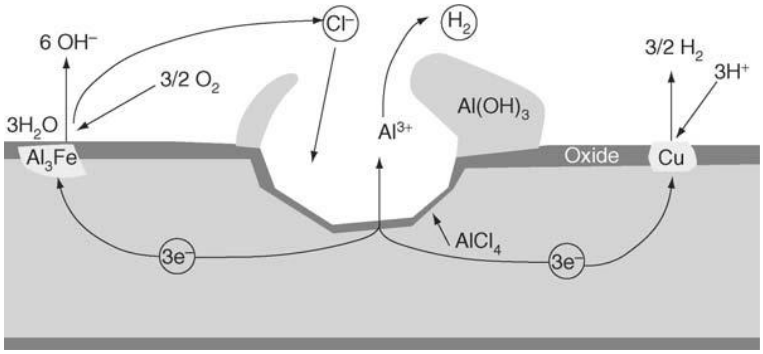

Figure 2.2: A schematic for the propagation of the pit in Al alloys [21].

In this mechanism, the presence of Cl^- plays a pivotal role, in which Cl^- chemically interacts with the passive oxide film to forms soluble oxychloride complexes (AlOCl). During the hydrolysis of oxychloride complexes, aluminum chlorohydrate ($Al(OH)_xCl_{(3-x)}$) and hydrochloric acid (HCl) are formed, which acidify the solution (to pH≈3). The acidification in-turn allows the pit to propagate further into the substrate, hence the autocatalytic nature.

The pitting potential (E_{pit}) indicates the potential above which pitting corrosion takes place. The average E_{pit} value for AA6xxx in 0.1 M NaCl is -0.670 ± 0.020 V_{SCE} [24, 28].

The pitting corrosion of AA6xxx is associated with the intermetallic particles that exist in the alloy. These intermetallic particles are typically the precipitation of various impurity elements due to their low solubility in the Al matrix. Studies have shown that the

intermetallic particles, enriched in Fe, Mn, Si, and Cu, are typically cathodic to the surrounding Al matrix. When these cathodic particles are positioned with in a grain, corrosion will take place in the surroundings of these cathodic particles in the form of "trenching", as shown in [32]. The progress of trenching leads to the formation of a primary pit around the particle and secondary pits adjacent to the particle.

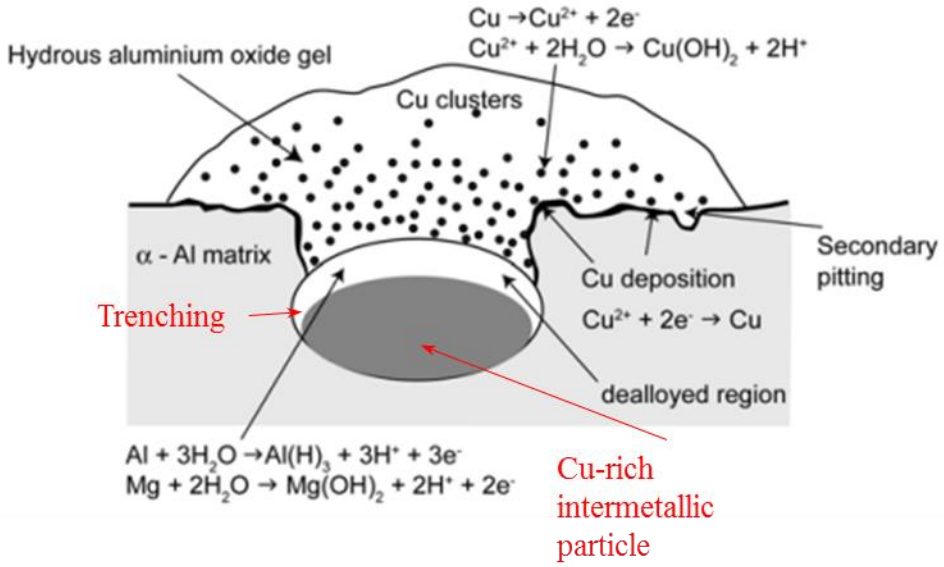

Figure 2.3: 8. Schematic of trenching around a Al_2CuMg particle with an Al matrix [32].

2.1.2.3. Intergranular Corrosion and Exfoliation Corrosion

Intergranular corrosion (IGC) is a form of corrosion that selectively attacks the grain boundary zone, while exfoliation corrosion is a form of severe IGC when the grains are elongated due to cold rolling. IGC takes place on the grain boundaries due to the formation of micro-galvanic cells between the Al matrix and secondary phases [30]. In the context of

AA6xxx, the secondary phases are various intermetallic phases include $Al_xCu_yFe_z$, Al_2Cu, Al(FeMn)Si, etc. that are not soluble in the Al matrix. These intermetallic phases are typically cathodic to the Al matrix, for example, in 0.1 M NaCl solution, Al_7Cu_2Fe and Al_2Cu have E_{corr} value of -0.551 V_{SCE} and -0.665 V_{SCE} in comparison with -0.823 V_{SCE} of the Al matrix [33]. Due to the cathodic nature of these intermetallic phases, when they are positioned near or on the grain boundary, the Al matrix grain boundaries surrounding them will corrode first, which leads to the subsequent IGC [30].

2.1.2.4. Filiform Corrosion

Filiform corrosion is a common form of localized corrosion for coated Al alloys. In practice, filiform corrosion is of importance since the external Al alloy automotive panels have a protective coating scheme applied.

Filiform corrosion takes place on the interface between the Al substrate and coating through a defect or a break on the coating, and produces a thread-like blister called a "filament" underneath the coating [21]. The filament can be divided into two parts, the "head" and the "tail". The propagation of filament occurs via an anodic reaction, Al oxidation, that takes place at the head and an accompanying cathodic reaction, oxygen reduction, that takes place in the tail [34]. This process is showcased in Figure 2.4.

The initial corrosion product formed in the head of filament has been shown to be aluminum chloride hexahydrate ($AlCl_3 \cdot 6H_2O$), which is highly hydroscopic [34, 35].. Upon further absorbing moisture from humid air, the aluminum chloride undergoes hydrolysis

and forms aluminum chlorohydrate ($Al(OH)_xCl_{(3-x)}$). This hydrolysis process produces osmotic pressure on the coating, which serves as the driving force of the coating separating from the metal substrate In the tail of filament, when combining with carbon dioxide (CO_2) in the air, aluminum chlorohydrate ($Al(OH)_xCl_{(3-x)}$) transforms to a carbonate-containing aluminum hydroxide gel ($Al(OH)_{3-x}(CO_3)_x$) and releases Cl^-.

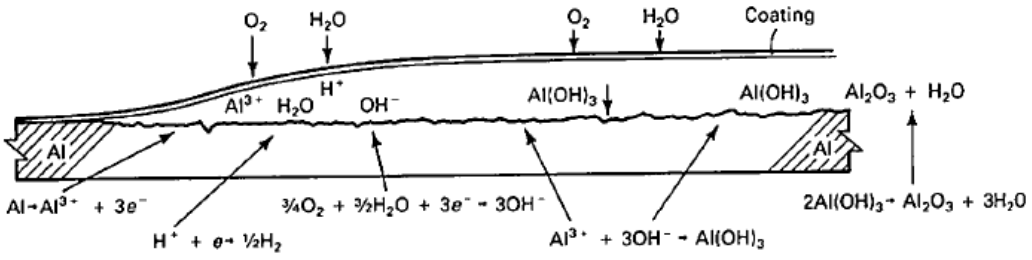

Figure 2.4: Schematic for filiform corrosion of Al [30].

It is noted that while it is possible for the filament to propagate at low relative humidity (RH), the filament propagates faster when the humidity increases above the deliquescence point, since more water will be absorbed by the electrolyte solution in the head, therefore creating a larger osmotic pressure [34].

The surface treatment of Al alloy substrate also affects the propagation of filament. Cold rolling creates a surface deformed layer that has elongated grain along the rolling direction. In addition, cold rolling also creates rolling lines on the surface, which are advantageous for the propagation of corrosion filaments. Multiple studies have observed that the direction of filament propagation aligns with the rolling direction of the Al alloy substrate [20, 36, 37, 38].

2.1.3. Effect of Alloying Elements

2.1.3.1. Magnesium and Silicon

Magnesium (Mg) and silicon (Si) are the main alloying elements of AA6xxx. Mg and Si are added to form Mg_2Si, which is the main strengthening precipitate of AA6xxx [7]. Studies have shown that Mg_2Si precipitates are less noble compared to the Al matrix (-1.2 V_{SCE} vs. -0.823 V_{SCE} in 0.1 M NaCl). After 10 minutes of immersion in 0.1 M NaCl, corrosion is observed on Mg_2Si precipitates. Further immersion results in the preferential dissolution of Mg in Mg_2Si, leaving Si-rich precipitates as remnant [39]. These Si-rich precipitates have relatively low conductivity and is often in the form of SiO_2 which is insulating. For this reason, the presence of Mg_2Si has very limited influence on the corrosion resistance of AA6xxx [39, 40, 41]. Si particles can also exist in AA6xxx when the Si concentration exceeds the stoichiometric amount required for Mg_2Si. Previous study by Bhattamishra et al. indicates that Si precipitates have a tendency to segregate at the grain boundaries and thereby posited to promote IGC [42]. However, recent studies have shown that when in contact with aqueous media, Si precipitates are covered by an insulating layer of SiO_2, which are not effective cathodes. Therefore, Si precipitates have limited influence on the overall corrosion property of AA 6xxx [28, 39, 41].

2.1.3.2. Copper

The addition of copper (Cu) in AA 6xxx promotes the formation of $Al_5Cu_2Mg_8Si_6$, known as the Q-phase, and other Cu-containing intermetallic phases, such as Al_2Cu and Al_7Cu_2Fe.

The presence of Q-phase has stronger strengthening effect on the alloy than Mg_2Si alone, and therefore is favored by some automakers [8]. However, the addition of Cu increases the cathodic branches of the polarization curves, indicating a higher current density, which increases the corrosion rate. Higher weight loss rate is observed among the Cu-rich AA6xxx in comparison with the Cu-lean ones [28]. Multiple sources also unanimously point out that Cu has adverse effect on the IGC resistance of AA6xxx, due the strong cathodic nature of Cu-bearing intermetallic phases [28, 41, 43, 44]. Various critical Cu contents for IGC are reported in literature ranging from 0.1 wt. % to 0.4 wt. % depending on the temper of the alloys [28, 41, 44].

2.1.4. Effect of Temper

For bare Al alloy, there are four main categories of temper: natural aging, under aging, peak aging, and over aging [20]. For coated Al alloy used in automotive industries, paint bake, otherwise known as bake hardening, is also used as a means to temper the Al alloy [7, 8].

Studies by Liang et al. and Kairy et al. provide a holistic overview on the effect of temper on the corrosion resistance of AA6xxx alloys. In all cases, natural aging after solutionization provided the highest corrosion resistance, due to the lack of secondary phases in the oversaturated Al matrix. As the aging time increases, the alloy transition from under aging to eventually over aging, the precipitation of intermetallic particles from the previously oversaturated Al matrix took place and eventually reached equilibrium at over aging state. The formation and growth of these intermetallic particles, particularly Fe/Mn and Cu bearing particles, reduced the corrosion resistance. At natural aging and under aging states,

the Al alloys were found to be immune to IGC, whereas IGC was observed primarily in the peak aging and over aging states [17, 28].

The paint bake after solutionization generally falls between under aging and peak aging due to the short duration and relatively low temperature [7, 8]. However, in this work, the Al alloy were first tempered to peak aging (T6) and then were subjected to paint bake. For this reason, the Al alloys used in this work should be considered to be between peaking aging and over aging.

2.1.5. Effect of Plastic Deformation

During hemming operation, the inner surface of the flange (outer sheet) is subject to compressive stress, while the outer surface is subject to tensile stress. A study by Muderrisoglu et al. on the hemming of AA1050, a low strength aluminum alloy, reports that the occurrence of micro-cracking is directly related to the bending radius of the sheet. For 1 mm thick AA1050 sheets, the critical bending radius below which micro-cracking occurs is 1 mm [10]. Micro-cracks have a negative impact of the localized corrosion resistance of the Al alloy, since micro-cracks weaken the integrity of the surrounding passive film and can serve as initiation sites for localized corrosion to take place [20, 21].

Residual stress due to plastic deformation also adversely affects the localized corrosion resistance of Al alloy. A study by Huang et al. reports that cold rolled AA5083 sheet has higher i_{corr} value than that of homogenized AA5083 sheet. Plastic deformation due to cold rolling creates a deformation-induced zone that has larger total area proportion and greater number of Al(Fe,Mn) intermetallic particles, which caused the plastically deformed

region to be more susceptible to pitting corrosion and IGC [45]. A study by Abdulstaar et al. shows similar result that plastic deformation near surface adversely affect the localized corrosion resistance of Al alloy by alternating the size and distribution of Fe-rich intermetallic particles. These Fe-rich intermetallic particles, in turn, increase the pitting corrosion and IGC susceptibility of the Al alloy [46].

2.2. Non-Destructive Evaluation of Adhesive Bonded Hem Flange

2.2.1. Neutron Radiography (NR)

Neutron radiography (NR) is an imaging technique that utilizes a beam of thermal neutron as its source of radiation. The resulting radiograph is recorded on a conventional photographic film. The theoretical basis of NR is the interaction between the nucleus of an atom and the incoming neutron, in which three types of possible outcomes are produced: scattering, absorption, or no interaction. The probability of a nucleus to absorb or scatter neutron is measured in neutron cross-sectional area, barn ($1\ b = 10^{-28}\ m^2$). Nuclei of different elements have different neutron cross-sectional areas, which enable them to be imaged on film with contrast, and thereby differentiating them [47]. The schematic of a typical NR facility is shown in Figure 2.5.

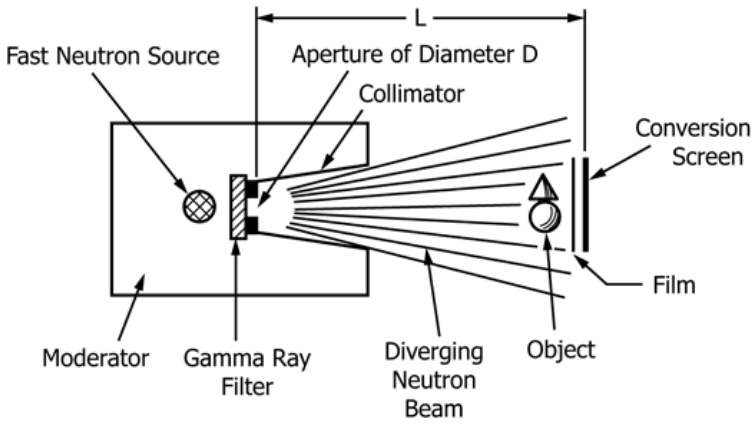

Figure 2.5: Schematic of a typical NR facility [48].

Due to the high construction and maintenance cost of a functional thermal neutron source for NR imaging, typically a nuclear reactor or an accelerator is required [47]. Therefore, NR is not a routine inspection technique utilized within the automotive industry [49]. However, the use of NR to evaluate adhesive bonded metal joints has been reported in the literature [50]. The NR image of a car door is shown in Figure 2.6.

Figure 2.6: NR image of a car door. Adhesive bonded hem flange is highlighted in the red box [50].

Various reports in the literature also suggest that using NR to image adhesive bonded metal joint is feasible. Common metals used in adhesive bonded metal joints include Al-based and Fe-based alloys, while the adhesive is typically an organic resin that contains large amount of hydrogen (H) atoms. As shown in Figure 2.7, the mass attenuation coefficient of the H atom is three orders of magnitude higher than that of either the Al atom or Fe atom [47].

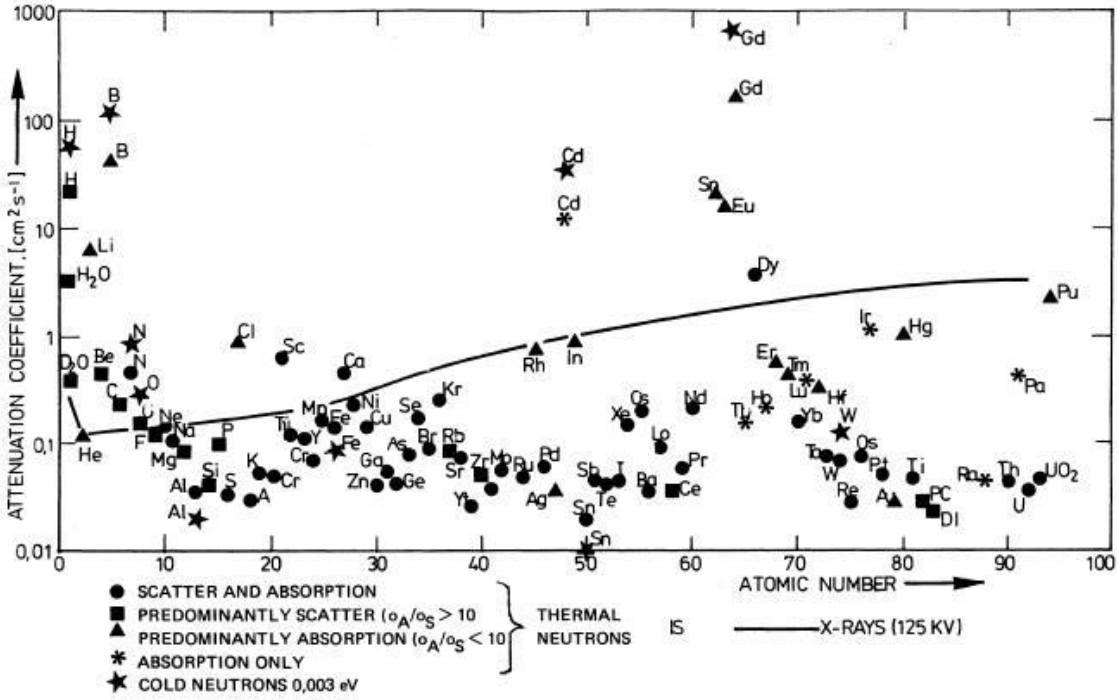

Figure 2.7: Neutron and X-ray mass attenuation coefficients for the elements [47].

The large differentiation of the mass attenuation coefficient between the H atom and other common metallic atoms gives NR technique a salient advantage for imaging the adhesive layer within an adhesive bonded metal joint; since the metal parts are almost neutron

transparent, and appear bright on the radiograph, whereas the adhesive layer is neutron opaque, and appears dark on the radiograph [51, 52, 53].

2.2.2. X-Ray Computed Tomography (CT)

X-ray computed tomography is a 3D NDE technique that uses computer algorithms to combine various 2D X-ray images of an object taken at different angles and create tomograms or reconstructed 3D models, based on individual tomograms, that allow the user to observe the internal structure of an object without cutting [54]. CT is of interest when the primary goal is to locate and size the volumetric detail of an object in 3D [55].

Due to the sample size limit of the commercial CT equipment and the large computing power required for data processing, no literature suggest that CT can be used by the automakers as a routine inspection technique for automotive hem flanges. However, various literature have demonstrated the capability of CT technique in imaging complicated organic materials as well as inorganic composite materials [56, 57].

2.3. Corrosion of Adhesive Bonded Al Alloy Joint

2.3.1. Mode of Failure

When an adhesive bonded joint fractures, there are three possible mode of failure: adhesive failure, cohesive failure, and adherend failure, as shown in Figure 2.8. In practice, when the adherends are common structural alloys like Al or steel, the strength of adherend is

typically 10 – 50 times higher than that of adhesive or the bond strength between adhesive and metal, therefore making adherend failure, Figure 2.8 (c), highly unlikely to occur [53].

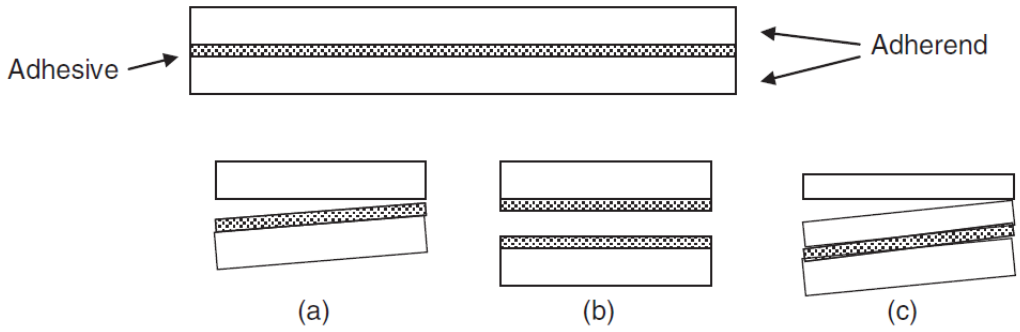

Figure 2.8: Schematics of three adhesive bond failure modes: (a) adhesive failure, (b) cohesive failure in the adhesive layer, and (c) adherend failure [53].

When the bond strength between adhesive and adherend, controlled by the chemical interaction between the adhesive and adherend, is lower than the strength of the adhesive, which is controlled by the strength of the polymer, bond failure occurs on the adhesive-adherend interface, which is called adhesive failure, Figure 2.8 (a). This type of failure results in one of the fracture surface having areas uncovered with adhesive. When the bond strength between adhesive and adherend is higher than the strength of the adhesive, bond failure occurs in the bulk of adhesive, which is called cohesive failure, Figure 2.8 (b). This type of failure produces two fracture surfaces that are both covered by the adhesive [53].

2.3.2. Influence of Corrosive Aqueous Media

The presence of corrosive aqueous media can affect three possible regions in an adhesive bonded Al alloy joint: the adhesive layer, the adhesive-Al oxide interface, and the Al alloy substrate [53].

2.3.2.1. Adhesive Layer

The adhesive layer, due to its polymeric nature, allows the permeation of water [58]. In a study by Bowditch et al., the influence of water on the adhesive strength is demonstrated. The retained tensile lap-shear joint strength of glass-reinforced plastic after various exposure duration in 70 °C and 90% RH is shown in Figure 2.9 [59]. It is worth mentioning that the glass-reinforced plastic is non-metallic and immune to environment that contains only water vapour (humidity). Therefore, the results of this study reflect the adverse effect on strength when adhesive absorbs water.

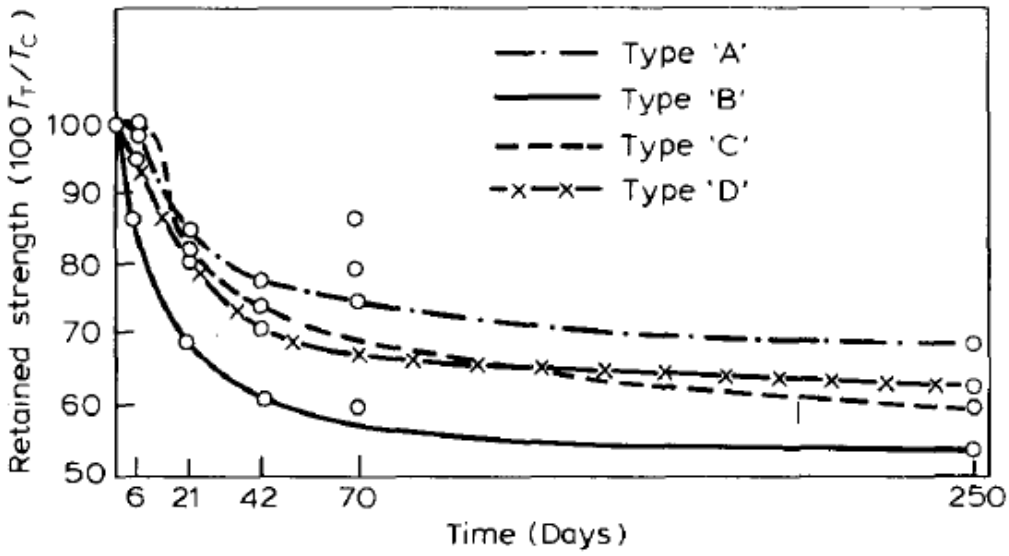

Figure 2.9: Effect of 70 °C and 90% RH exposure on tensile lap shear joint-strength. Type A, B, C, and D represent four different types of adhesive [59].

The adverse effect of water on the strength of adhesive layer, also known as "humid ageing", is explained by two mechanisms: swelling and plasticization [60]. Swelling indicates the volumetric expansion of adhesive upon absorbing water, which decreases the rigidity of the adhesive layer and, subsequently, reduces the strength. Plasticization indicates the process where the hydrogen bonding between the polymeric chains of the adhesive is disrupted when the adhesive absorbs water; this process, subsequently, also reduces the strength of the adhesive layer [58, 61].

2.3.2.2. Adhesive-Al Oxide Interface and Al Alloy Substrate

When exposed to a humid environment, water can permeate into the adhesive layer and adsorb onto the adhesive-Al oxide interface region [53]. If the environment is free of Cl^-, the adsorption of water molecules onto the adhesive-Al oxide interface has very limited impact on the bond strength. Study by Prolongo et al. suggests that adhesive bonded AA1050 lap-shear joint suffered no observable strength loss after 7 days of exposure at 23 °C and 98% RH in comparison with the non-exposed lap-shear joint [60]. In comparison with the humid ageing results by Bowditch et al., as shown in Figure 2.9, it is worth mentioning that the results by Prolongo et al. are from the lap-shear joints exposed in lower temperature and for shorter duration. The study by Gledhil et al. also reports that low temperature ($T < 70$ °C) exposure to humid environment for short duration produces very limited effect on the bond strength [62].

When the environment contains Cl^-, Prolongo et al. showed that the adhesive bonded AA1050 lap-shear joint suffered 26% strength loss after 7 days of exposure at 23 °C, 98% RH, and 0.5 wt. % NaCl in comparison with the non-exposed lap-shear joint [60]. The fracture surface of the lap-shear joint exposed in Cl^- containing environment indicates a combination of adhesive failure and cohesive failure, as shown in Figure 2.10.

The schematics of adhesive failure promoted by the corrosion of Al oxide layer and Al alloy substrate is shown in Figure 2.11. The corrosion mechanism of Al oxide and Al alloy substrate in Cl^- containing environment is consistent with the one provided in section 2.1.2. , where the Al oxide layer undergoes thinning and the Al substrate undergoes pitting corrosion, possibly in combination with IGC, in Cl^- environment [20].

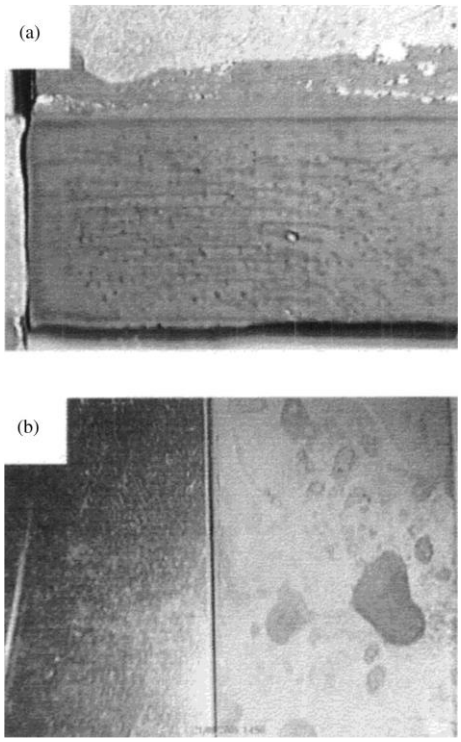

Figure 2.10: Macrographs of (a) the debonded area (adhesive failure) of the joint and (b) two Al substrates prior to corrosion (on the left) and after corrosion in a saline environment (on the right) [60].

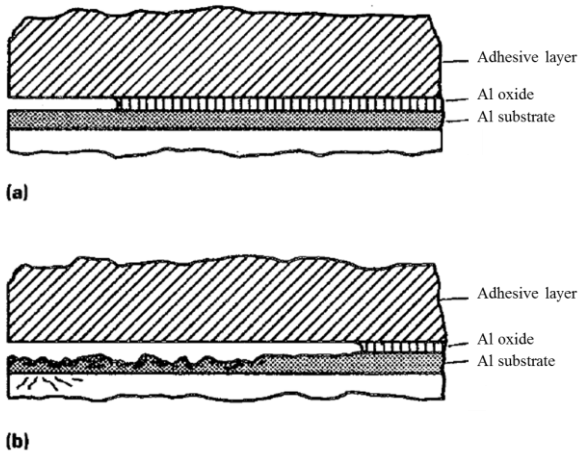

Figure 2.11: Schematics illustrating the causes of adhesive failure on an Al substrate. (a) Corrosion of adhesive-Al oxide interface. (b) Corrosion of interface and substrate [20].

2.4. Summary

In Section 2.1.1. , it is established that the corrosion of Al alloys in automotive components often occur in aqueous environment containing Cl^-, and possibly acidified due to the presence of acid gases (NO_x and SO_x). Current accelerated salt spray protocols widely used in the automotive industry are capable of producing comparable corrosion damage on automotive Al alloys in laboratory conditions compared to natural weathering conditions. However, the corrosion resistance of coated automotive Al alloy hem flanges was not previously reported. For this reason, it is of interest to study the corrosion resistance of Al alloy hem flanges using the existing accelerated salt spray protocols.

In Section 2.1.2. , various forms of localized corrosion related bare and coated AA6xxx are reported. The crucial factors influencing these localized corrosions of AA6xxx are also reported. In this work, Cu content was the only variable in the two alloys of interest, AA6022 and AA6111. For this reason, the comparison of the corrosion of AA6022 and AA6111 was well reported in the literature.

In Section 2.2. , a few cases of using NR and X-ray CT to characterize composite structure similar to Al hem flange, a composite consisting Al and adhesive, are reported. This provides theoretical support to the employment of NR and X-ray CT to characterize Al hem flange, which was not previously reported.

In Section 2.3. , the general corrosion behaviour of adhesive bonded Al alloy joint is reported. However, due to the large varieties of adhesive available in the market, it was difficult to pin point the corrosion behaviour of the kind of adhesive used in this work. To this end, it was of interest to study this behaviour as the adhesive is an important component in the hem flange assembly.

Chapter 3: Research Objective

Previous studies have shown that filiform corrosion on coated Al alloys can occur in humid environments when either of the following conditions is met: (i) the presence of defects or breaks in the coating exposing the base metal to the environment, or (ii) having a coating with a high permeability to water and oxygen [19, 63]. Today's automotive coating systems typically contain multiple layers of epoxy and acrylic resin and are highly impermeable by water, which significantly reduces the likelihood that condition (ii) is met [64]. For this reason, the mechanism by which filiform corrosion of coated Al alloys occurs is likely through condition (i); i.e. through defects or breaks in the coating. This mechanism has been widely reported in the literature [34, 35, 38]. However, filiform corrosion associated with coated Al alloy hem flanges (Figure 1.4) has not been reported in the literature.

This work, in association with Ford Motor Company Project Northern Star, seeks to provide a means to improve vehicle design, in particular, the design of hem flange and its surrounding area, by acquiring a better understanding of the corrosion resistance of coated hem flange testing coupons [15].

The working hypothesis underpinning the current research is that cyclic deformation works in combination with cyclic corrosion conditions (in this case, the FORD L-3190 testing protocol) to increase the susceptibility to of coated automotive Al alloy hem flange joints to localized corrosion damage [65]. The associated set of research objectives include the following:

i. Develop a laboratory methodology to characterize the adhesive coverage and the connectivity of air pores within an automotive hem flange joint.

ii. Develop a cyclic deformation testing protocol to accumulate such damage into the coated AA6xxx hem flange coupons.

iii. Evaluate the effect of prior cyclic corrosion damage on the cyclic deformation response of the coated AA6xxx hem flange coupons.

iv. Evaluate of the effect of prior cyclic deformation damage on the cyclic corrosion resistance of the coated AA6xxx hem flange coupons.

Chapter 4: Experimental Methods

4.1. Fabrication of Hem Flange Coupons

In this work, the influence of the combination of cyclic deformation and cyclic corrosion on coated AA6022 and AA6111 automotive hem flanges was investigated. The hem flange coupons used in this work were fabricated by Ford Research Laboratory using commercial AA6022 and AA6111 wrought 1 mm thick sheets in the T6 temper. Prior to the hemming operation, the aluminum sheets were pre-treated with a zinc phosphate conversion coating. The hem flange coupons were fabricated using the three-step hemming operation shown in Figure 1.3. The hem flange coupons were subsequently painted using a standard automotive e-coating process, which included a paint bake step for 30 minutes at 180°C. Upon receiving the hem flange coupons (20 cm wide), they were sectioned into smaller parts (3.5 cm wide) by the McMaster Engineering and Science Machine Shop. The top-view of an original hem flange coupon fabricated by Ford Research Laboratory and a sectioned "sub-size" hem flange coupon are shown in Figure 4.1(a) and (b), respectively. Figure 4.1(c) shows the hem flange in cross-section. During the sectioning of the original hem flange coupon, sacrificial wood blocks were inserted in-between the outer sheet and the inner sheet. The thickness of these wood blocks was the same with the spacing between the outer sheet and the inner sheet, so that, during sectioning of the original hem flange coupons, the vibration of the outer sheet and inner sheet was sufficiently damped by the sacrificial wood blocks. The sectioning was carried out with constant lubrication to prevent over-heating of the hem flange coupon and low cutting speed to prevent damaging the adhesive layer. Uncoated

versions of the hem flange coupons were also provided by Ford. All of the uncoated hem flange coupons were also baked for 30 minutes at 180 °C prior to any testing.

An intentional burr (Figure 4.1(c)) was place at the termination of the outer sheet during the manufacturing of the hem flange coupon by Ford. The burr was placed here due to reports of cosmetic corrosion happening around this region, so that the burr was designed to potentially break the coating layer around it during cyclic deformation, which, in turn, creates a defect in the coating that allow cosmetic corrosion to occur [15, 66].

The adhesive used during the fabrication of hem flange coupons was a structural epoxy based adhesive, product code CI-5698B, from PPG Revocoat. A sample of the adhesive was provided by Ford along with the hem flange coupons.

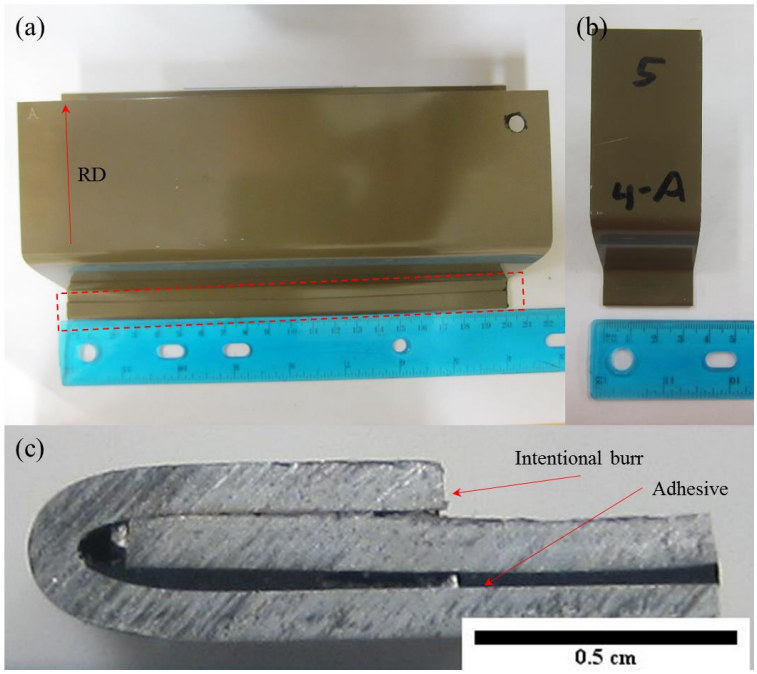

Figure 4.1: Top-view of (a) an as-received full-size coupon and (b) a sub-size coupon. (c) Cross-sectional view of a hem flange, taken from the section highlighted by the red frame in (a).

4.2. Characterization of Hem Flange Coupons

4.2.1. Chemical Composition

Small samples were removed from the uncoated AA6022 and AA6111 hem flange coupons by a sheet metal snip. The chemical composition of each alloy was determined by inductively coupled plasma optical emission spectroscopy (ICP-OES), the results of which are presented in Table 4.1. The major compositional difference between the two alloys was the concentration of Cu in each alloy; the AA6111 being the "Cu-rich" alloy contained 0.68 wt. % Cu whereas the AA6022 being the "Cu-lean" alloy contained 0.10 wt. % Cu. The compositions of both alloys were within their respective specifications [67].

Table 4.1: Chemical compositions (wt. %) of AA6111 and AA6022 determined by ICP-OES.

Alloy	Si	Mg	Cu	Mn	Fe
AA6111	0.70	0.81	0.68	0.20	0.27
AA6022	0.90	0.64	0.10	0.10	0.22

4.2.2. Microstructural Characterization

In order to examine the microstructures of each alloy and the adhesive, a cross-section of each alloy from the hem flange coupon was cold-mounted in epoxy. Prior to cold-mounting, the as-received hem flange coupons were cut using a band saw, then deburred and de-greased. The mounted surfaces were polished using standard metallographic techniques. The polished metallographic samples were imaged with a Keyence VHX-5000 light optical microscope (LOM) and a JEOL JSM-7000F scanning electron microscope (SEM). Prior to SEM analysis, a carbon film was deposited on the sample surfaces in order to prevent charging of the adhesive. To establish an electrical connection between the epoxy mount and the SEM sample mount, a strip of silver paint was applied onto the epoxy mount.

4.2.3. Vicker's Hardness Measurements

The Vicker's hardness of a cold-mounted hem flange sample at different locations was measured using a 50 gf load and a 10 second dwell time. The approximate locations, marked by red dots, where the measurements were taken are shown in Figure 4.2. The measurements near the surface were 0.025 mm away from the inner or outer surface, and the measurements in the center were taken at the mid-thickness point, which was 0.5 mm from the surface.

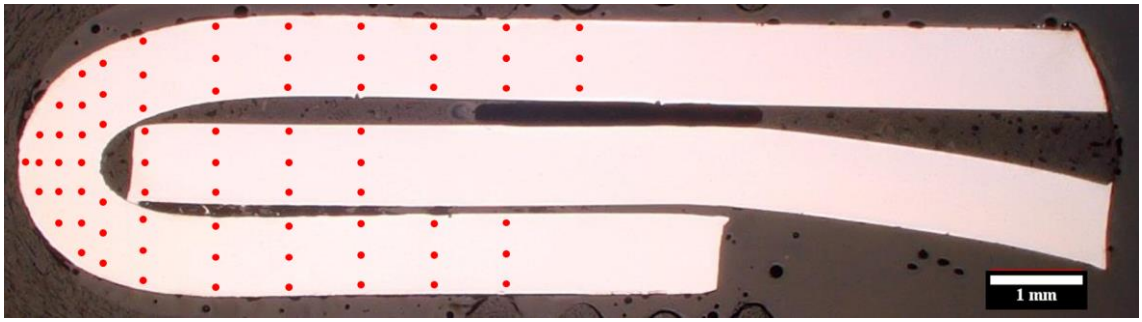

Figure 4.2: Cross-sectional LOM image displaying the approximate locations, using red dots, where Vicker's hardness measurements were taken.

4.2.4. Electrochemical Characterization

AA6022 and AA6111 sheets were removed from the un-deformed flat portion of the inner sheet of uncoated hem flange coupons and were subsequently cut to 1.0 cm × 1.0 cm square samples using an automatic precision saw. Aluminum tape was used to attach copper wires to the square samples. The samples were individually cold-mounted in epoxy such that the surface without wires attached to it was exposed and the wires were allowed to come out from the back side of the epoxy mount, as shown in Figure 4.2. The exposed surface was ground to remove all residual epoxy and then polished to a 1200-grit finish using SiC paper with water as the lubricant. Similar method was used to prepare samples cut from the tensile outer surface of the outer sheet of uncoated AA6022 and AA6111 hem flange coupons. The cutting location is shown in Figure 4.3(a), and the sample before cold mount in Figure 4.3(b).

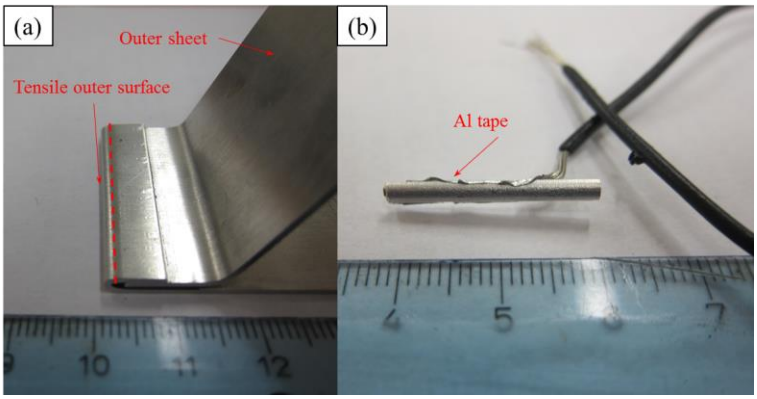

Figure 4.3: Photographs of (a) the tensile outer surface of an uncoated hem flange coupon, red line indicates the cutting line; (b) a sample of tensile outer surface before cold-mounting with copper wire attached.

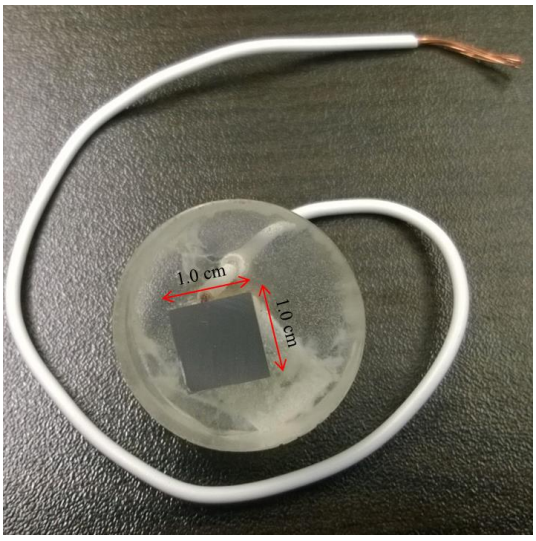

Figure 4.4: Epoxy-mounted 1.0 cm × 1.0 cm sample with copper wire attached.

Potentiodynamic polarization measurements were conducted on the mounted samples of AA6022 and AA6111 using a standard three-electrode cell configuration. The exposed surface of the sample acted as the working electrode; a saturated calomel electrode

was used as the reference electrode and a graphite rod as the counter electrode. The cell is illustrated in Figure 4.5. A Bio-Logic VSP-300 Potentiostat was used to carry out all electrochemical measurements in this work. Prior to the potentiodynamic polarization measurements, the potentiostat was calibrated according to ASTM G5-14 using an AISI 430 stainless steel sample [68].

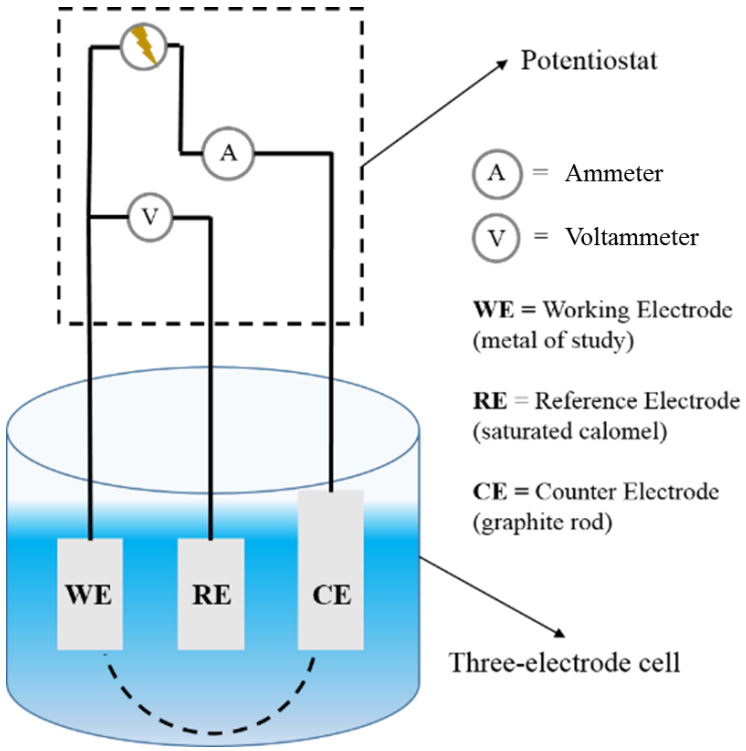

Figure 4.5: Schematic representation of the standard three-electrode setup used for open circuit and potentiodynamic polarization measurements.

An aqueous solution of 0.1 M NaCl at a near-neutral pH was used as the electrolyte for open circuit and potentiodynamic polarization measurements. This solution was selected based on a large volume of literature using the same solution [18, 24, 28, 33]. An aqueous solution of 0.1 M NaCl at pH 2.85 (± 0.05), adjusted by acetic acid, was also used

as an electrolyte for comparison to the near-neutral electrolyte. Prior to the measurements, all electrolytes were deaerated using N_2 via a frit glass tube for 45 minutes. The N_2 gas flow was maintained for the duration of the measurements.

Prior to potentiodynamic polarization measurements, all samples were held in the open circuit condition (OCC) for 10 minutes. The short OCC duration was chosen in order to reduce the effect of preferential dissolution of Mg_2Si precipitates on the overall polarization behaviour in the Cl^- containing electrolyte [28, 33, 39].

Potentiodynamic polarization measurements of each alloy were conducted immediately after the 10 minute OCC exposure for the purpose of comparing the electrochemical characteristics of AA6022 and AA6111. The working electrode potential was swept from 200 mV below OCP to 600 mV above OCP. The scan rate of all measurements was set to 1 mV/s for the purpose of replicating the experiments described in references [17, 28]. Each polarization measurement was repeated at least three times for each alloy using freshly-prepared electrolyte and freshly-polished samples to ensure reproducibility.

4.3. Non-Destructive Evaluation of the Hem Flange Coupons

4.3.1. Neutron Radiography (NR) Technique and Protocol

Neutron radiography (NR) is a 2D imaging technique that utilizes a thermal neutron beam as the radiation source. NR shows a strong ability to penetrate through relatively large cross-sections of most metals due to their relatively low neutron attenuation coefficient, while having a weak ability to penetrate organic materials due to the high neutron attenuation coefficient of protons (H^+) [69]. In this work, NR was considered an advantageous method to image the adhesive layer, an organic material, without needing to section the coupon.

The experimental setup of neutron radiography is illustrated in Figure 4.6. All NR experiments were carried out at the McMaster Nuclear Reactor (MNR), which is a 5 MW materials testing reactor with a core of low-enriched uranium. The neutrons produced by the reactor core were attenuated by a divergent collimator, which produced a neutron beam with angular divergence blow 2°, a cadmium ratio of 3.7, a collimation ratio of 141, and a flux of 3×10^6 n/cm^2/s [70].

Sub-size hem flange coupon samples were placed in an aluminum container box during irradiation. The positions of the coupons were fixed with tape. A vacuum cassette containing a gadolinium conversion screen and a conventional X-ray film was placed adjacent to the aluminum container box in order to intercept the neutron beam transmitted through the coupons. For simplicity, the schematic in Figure 4.6 only shows one hem flange

being imaged; in reality, the neutron beam was large enough to accommodate 20 coupons to be imaged in one shot.

After the neutron shot, the X-ray film was developed and subsequently digitized using a high-resolution Epson Expression 10000XL transmission scanner at 600dpi and 16 bit gray scale.

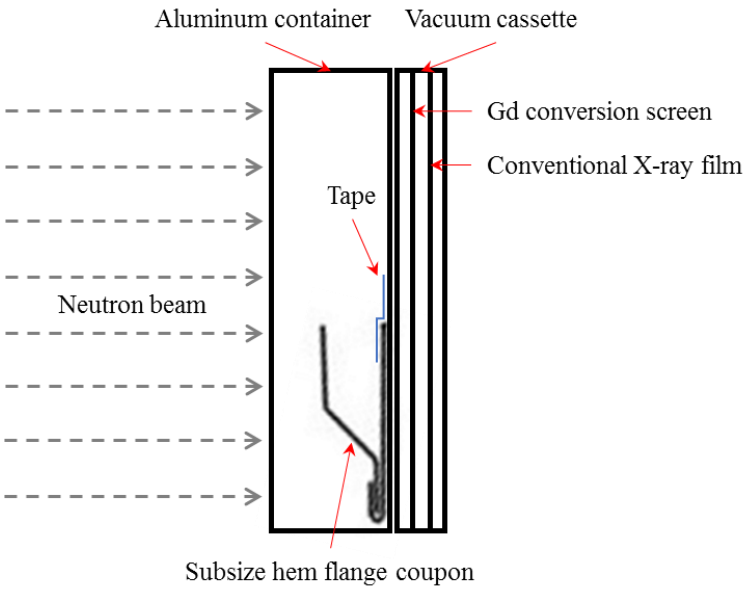

Figure 4.6: Side-view schematic illustrating the experimental setup for neutron radiography of the sub-size hem flange coupon.

4.3.2. Characterization of Air Pore Connectivity

The connectivity of the air pores in the adhesive was characterized using a dilute gadolinium(III) nitrate ($Gd(NO_3)_3$) solution, since Gd nuclei have the highest neutron attenuation coefficient amongst the elements.

In order to hold the $Gd(NO_3)_3$ solution in the hem flange coupons, the edges of the coupons were sealed with silicone gel, as shown in Figure 4.7(a), which served as a "dam". The $Gd(NO_3)_3$ solution was introduced into the cavity formed between the silicone gel. After the solution was introduced, the hem flange coupons were fixed onto a container box, as shown in Figure 4.7(b). The container box was held in the vertical position for 24 hours prior to NR, which allowed the solution to flow into any connected pores within the adhesive. The neutron shots were taken using the methods described in Section 4.3.1. .

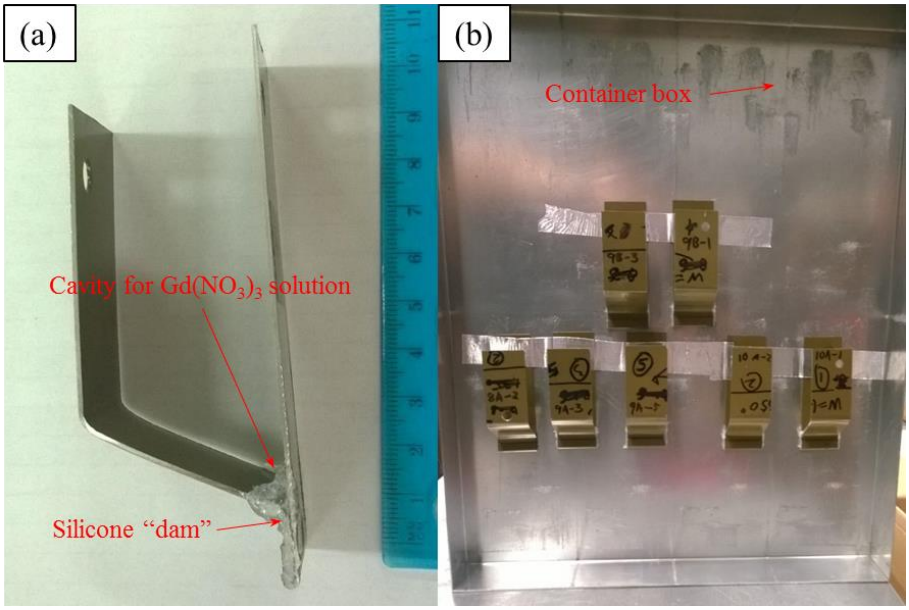

Figure 4.7: (a) Side-view image of a hem flange coupon with both edges sealed by silicone. (b) Photograph of the hem flange coupons fixed onto a container box and held in the vertical position.

4.3.3. X-ray Computed Tomography (CT) Technique and Protocol

X-ray computed tomography (CT) imaging provides an ideal examination technique whenever the primary goal is to locate and size planar or volumetric details in three dimensions (3D) for relatively small inspection volumes [71]. In this work, CT was used to study the 3D structure of the adhesive layer shown in Figure 4.1(c).

The X-ray images for CT reconstruction were produced by using a Bruker Skyscan 1172 CT machine. The X-rays were generated using an acceleration voltage of 85 keV with a total power of 10 W. A CCD camera was fiber-optically coupled to a scintillator with a

2000 × 1000 pixel array (2 mega-pixels) as the X-ray detector. The voxel size of the scan was set to 125 μm^3.

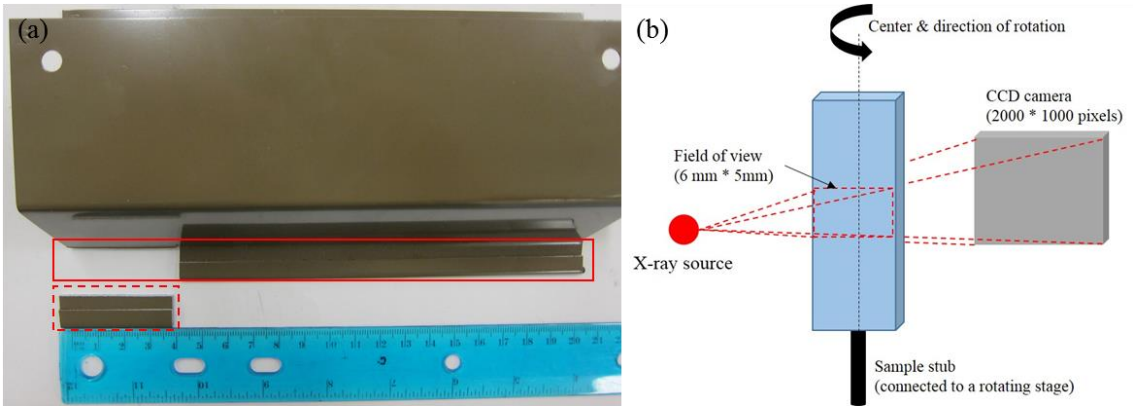

Figure 4.8: (a) Top view of the AA6111 full-size hem flange coupon showing a segment of the hem flange removed for CT imaging. (b) CT scan setup.

Hem flange coupons were sectioned to accommodate the size limits of the CT machine (Figure 4.8(a)). The sectioned coupon, as illustrated in Figure 4.8(b), was mounted vertically on a sample stub. One cross-sectional image was taken per 0.4° rotation of the coupon, resulting in 900 two dimensional images taken for a complete rotation (360°). Sample reconstruction was completed using Bruker NRecon software and the reconstructed slices were built into a 3D model using Bruker CTAn software.

4.4. Ford L-3190 Cyclic Corrosion Test

The aforementioned coated sub-size hem flange AA6022 and AA6111 coupons were subjected to cyclic corrosion testing in order to evaluate their corrosion resistance.

An Ascott CC1000 salt spray chamber was used for all Ford L-3190 testing. Prior to cyclic corrosion testing, the salt spray chamber was calibrated according to ASTM B117 [72]. The hem flange coupons were cleaned with soap and water, labeled, and photographed. The exposed edges of the hem flange were covered with multiple layers of nail polish lacquer to prevent solution ingress to the hem area. The layout of the hem flange coupons (Figure 4.9(b)) within the salt spray chamber is shown in Figure 4.9(a). A set of scribed AA6022 and AA6111 (Figure 4.9(c)) hem flange coupons were also included in the cyclic corrosion test. The scribe was made using a tungsten carbide scribing pen, and was 1 ~ 1.5 mm wide. The electrical conductivity of the scribe was measured using a multimeter to ensure that the scribe fully penetrated the coating layer.

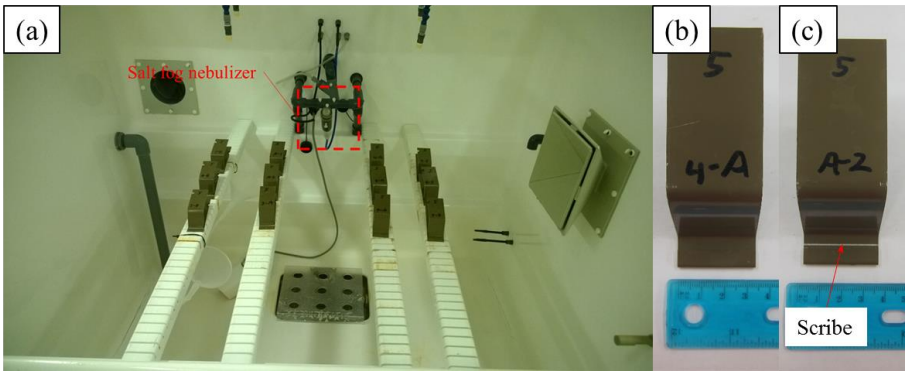

Figure 4.9: (a) Experimental setup for the Ford L-3190 cyclic corrosion testing of sub-size hem flange coupons. (b) Top-view photograph of a hem flange coupon. (c) Top-view photograph of a scribed hem flange coupon.

A schematic process flow diagram of the daily Ford L-3190 salt spray cycle is shown in Figure 4.10. The salt spray chamber was configured so that a linear humidity ramping was ensured during the transition phase. In addition to the daily salt spray cycle, the coupons were removed from the chamber and sprayed with a 0.5 wt. % NaCl pH 2.8 solution, acidified by acetic acid, on a weekly basis. After the acidified spray, the coupons were allowed to dry under ambient conditions for 1 hour before being transferred back to the salt spray chamber. The duration of exposure was 6 weeks for one group of coupons and 12 weeks for another group of coupons.

After exposure, several coupons were selected for metallographic examination while the remaining coupons were rinsed in DI water, dried, and retained for later testing. The coupons selected for metallographic examination were cross-sectioned and cold-mounted. The mounted cross-sections were polished using standard metallographic techniques and then analyzed using LOM to determine the extent of corrosion damage within the interior of the hem flange.

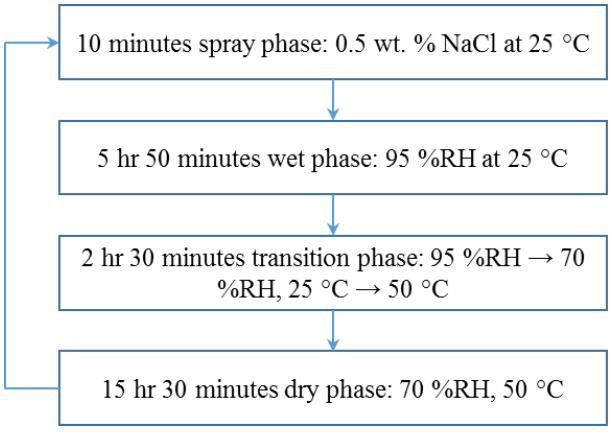

Figure 4.10: Flowchart of the daily repetitive Ford L-3190 salt spray cycle.

4.5. Cyclic Deformation Tests

In order to evaluate the effect of cyclic corrosion on the performance of hem flange coupons under cyclic deformation conditions, both the exposed coupons, as prepared using the Ford L-3190 procedure specified in Section 4.4. and as-received coupons were subjected to cyclic deformation testing. The testing conditions and the post-test characterization of the hem flange coupons are tabulated in Table 4.2. Each coupon in Table 4.2 had one AA6022 version and one AA6111 version.

Table 4.2: Testing conditions and characterization of the hem flange coupons

Coupon #	Testing Condition	Characterization
1-3	Cyclic deformation test for 250,000 cycles	Side-view LOM after 250,000 cycles
4-6	① Six-week exposure in Ford L-3190 test ② Cyclic deformation test for 250,000 cycles	Cyclic deformation test paused at 100,000 cycles for side-view LOM.
7, 8	① Twelve-week exposure in Ford L-3190 test ② Cyclic deformation test for 250,000 cycles	
9, 10	① Cyclic deformation test for 30,000 cycles ② Six-week exposure in Ford L-3190 test	Side-view LOM after ① and then after ② Metallographic examination on coupon #9, 12 of AA6022, and coupon #10, 12 of AA6111
11, 12	① Cyclic deformation test for 30,000 cycles ② Six-week exposure in Ford L-3190 test with static stress super-imposed	
13 (control)	① Cyclic deformation test for 30,000 cycles ② Six-week exposure in ambient lab air with static stress superim-posed	

4.5.1. Cyclic Deformation Test of Exposed and Unexposed Coupons

All cyclic deformation tests were carried out using an Instron hydraulic testing frame horizontally mounted in a salt spray chamber, Figure 4.11(b). The hem flange coupon was held in place by AISI 316L stainless steel fixtures, as shown in Figure 4.11(a).

During the cyclic deformation test, the hem flange coupon was first pulled to the +1 mm position from its neutral position. From the +1 mm position, the hem flange coupon was subject to displacement controlled cyclic loading of ±1 mm at 2 Hz for up to 250,000 cycles. The net displacement of the cyclic loading test was from 0 mm, the neutral position, to +2 mm.

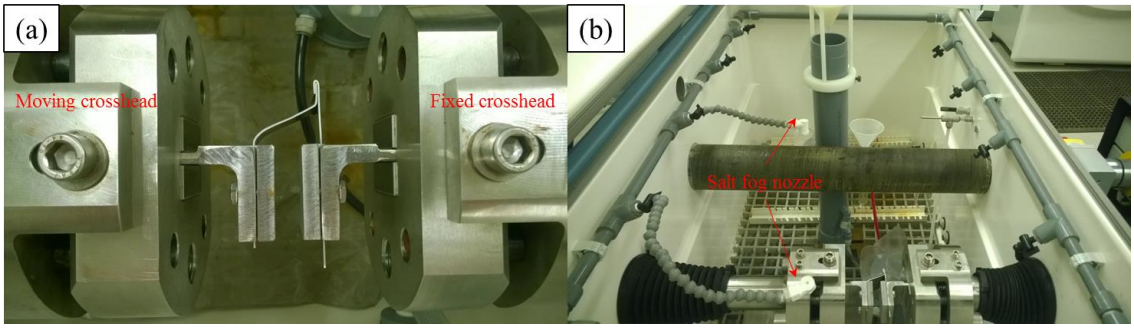

Figure 4.11: (a) Photograph of the experimental setup top-view for the cyclic loading test of sub-size hem flange coupons; (b) photograph of the testing frame and the salt spray chamber.

After cyclic deformation, the hem flange coupons were examined in side-view using LOM to determine the extent of adhesive failure.

4.5.2. Ford L-3190 Cyclic Corrosion after Cyclic Deformation

A selection of hem flange coupons of each alloy were cyclically deformed for 30,000 cycles (Table 4.2), using the same method specified in Section 4.5.1. After cyclic deformation, the hem flange coupons were transferred into the salt spray chamber and exposed for six-week duration to the Ford L-3190 cyclic corrosion test (Figure 4.10).

After the cyclic corrosion test, the hem flange coupons were removed from the salt spray chamber, cleaned in DI water and dried. One hem flange coupon of each alloy was cut in cross-section, cold-mounted and polished. The polished samples were metallographically examined using LOM.

4.5.2.1. Cyclic Corrosion Exposure with Static Stress Superimposed

In order to evaluate the effect of static stress on hem flange coupons with their adhesive pre-cracked during cyclic corrosion exposure, a selection of hem flange coupons of each alloy were cyclically deformed for 30,000 cycles. After cyclic deformation, two vertically aligned holes of 8 mm diameter were drilled through the grip sections of these coupons, as shown in Figure 4.12(a). A plastic bolt of 6.3 mm diameter with two plastic nuts was placed through the two holes (Figure 4.12(b)). By adjusting the spacing between the two plastic nuts, the hem flange coupon was held statically at the +2 mm displacement position (Figure 4.12(c)), thereby imposing a static stress on the assembly during cyclic corrosion testing.

The statically stressed hem flange coupons were then placed in the salt spray chamber (Figure 4.12(d)) and were subjected to a six-week Ford L-3190 cyclic corrosion test per Figure 4.10 .

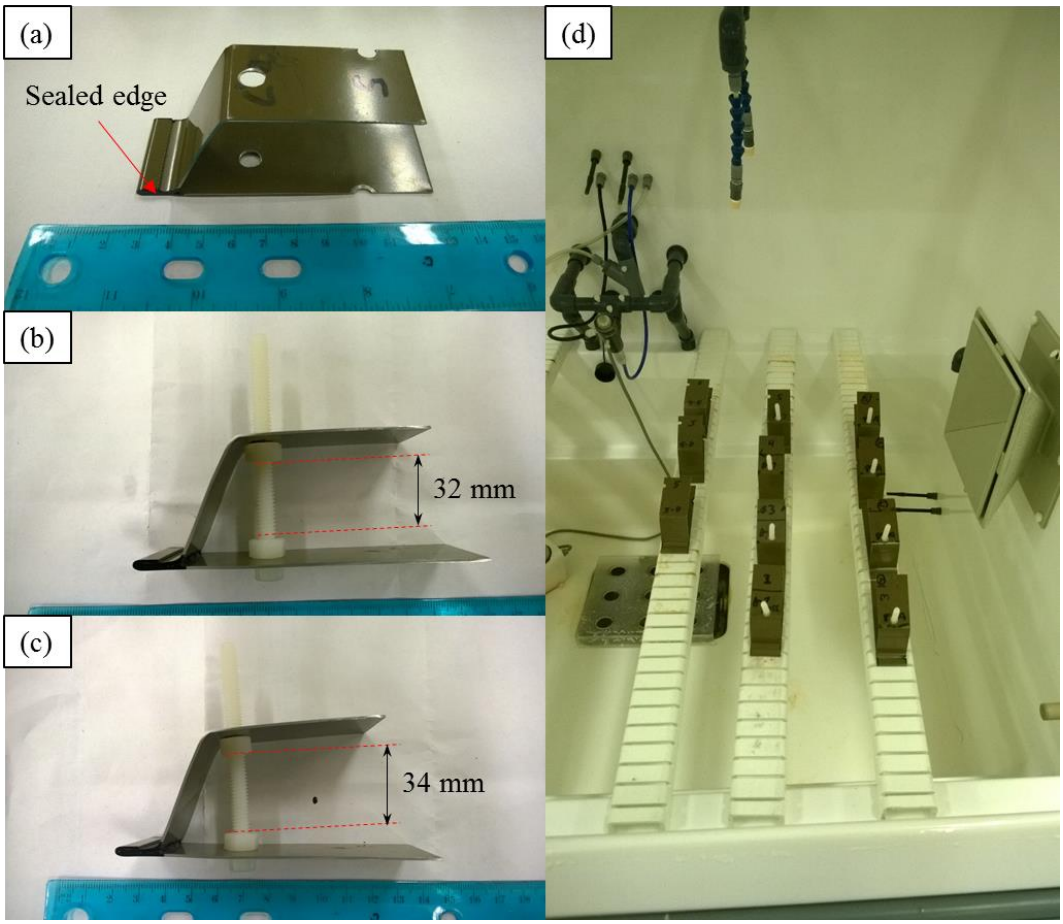

Figure 4.12: Photograph of (a) a hem flange coupon with two holes drilled, (b) a hem flange coupon at neutral position with a plastic bolt placed through the holes, (c) a hem flange coupon held at +2 mm position, and (d) the layout within the chamber.

Side-view images were taken using LOM after cyclic deformation but prior to the cyclic corrosion test in order to record the initial extent of adhesive damage. After six weeks

of exposure, the hem flange coupons were removed from the salt spray chamber, cleaned in DI water and dried. The nail polish lacquer on the sample edges was dissolved by rinsing the coupons in acetone. The plastic bolts were removed and the coupons imaged in side-view using LOM in order to determine whether the adhesive damage propagated under the static stress in the corrosive environment. In order to provide a control group, a selection of hem flange coupons held at the +2 mm position were placed in ambient lab air for 6 weeks and analyzed using the same method.

Chapter 5: Results

5.1. Hem Flange Coupon Characterization

5.1.1. LOM and SEM images of Hem Flange

The general characteristics of a sub-size hem flange coupon, referred to simply as "hem flange coupon" in later sections, are shown in Figure 5.1 (a). A hem flange coupon consisted for two sections, the actual hem flange section and the grip section where the machine crossheads were fixed onto the sample during cyclic deformation testing. The terminologies for the different regions of a hem flange coupon, i.e. areas A, B, C, and D are shown in Figure 5.1 and Figure 5.2(b). A higher magnification view of each area is shown in Figure 5.2.

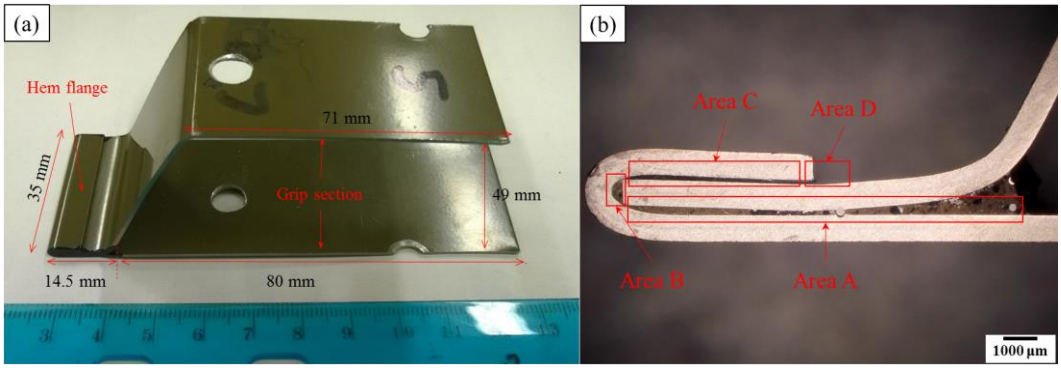

Figure 5.1: (a) Photograph of a hem flange coupon. (b) Side-view LOM image of a hem flange coupon, showcasing areas A, B, C, and D, highlighted by the red frames.

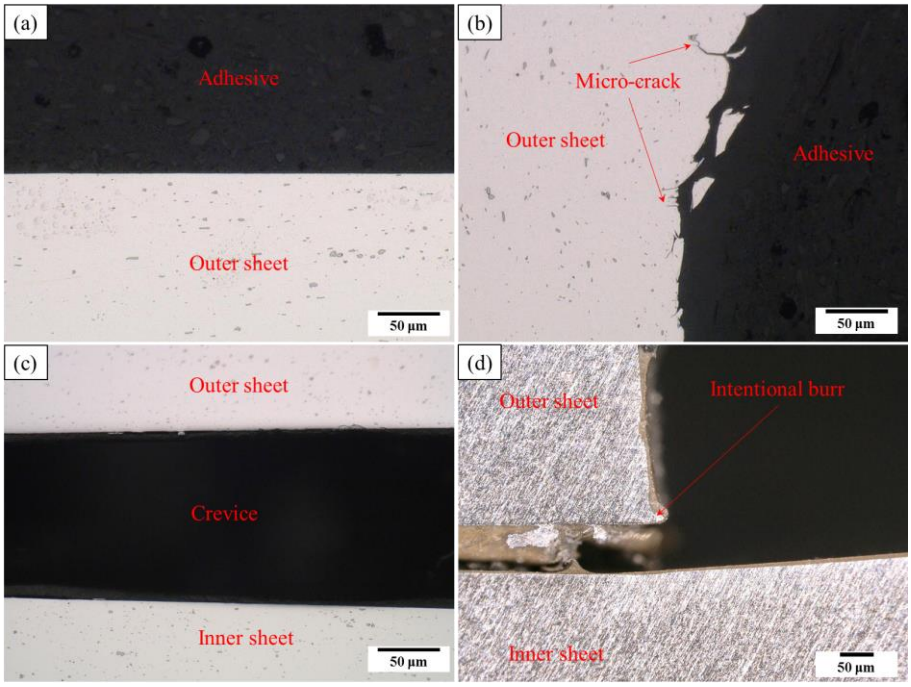

Figure 5.2: Cross-sectional LOM images of the four areas within a hem flange coupon: (a) area A, (b) area B, (c) area C, and (d) area D.

Based on numerous cross-sectional examinations using LOM, areas A, B and C can be generalized as follows: area A, where the adhesive was initially applied during manufacturing, was typically covered by adhesive. Area B comprises the semi-cylindrical cavity that was enclosed by the U-shaped outer sheet and the inner sheet; micro-cracks were usually observed in this region (Figure 5.2(b)) due to the high degree of plastic deformation arising from the hem flange manufacturing operation. Area C was found to consist of the crevice that was formed after the outer sheet was folded onto the inner sheet. This area typically had no adhesive.

Areas A and B were observed at higher magnification, as shown in Figure 5.3 and Figure 5.4, respectively. Due to the lack of plastic deformation in area A (Figure 5.3), the base metal had a smooth interface with the adhesive. By comparison, the base metal in area B featured a rough interface with the adhesive due to the high compressive plastic deformation in this area, Figure 5.4(a) and(c). The micro-cracks observed in area B (Figure 5.4(b) and (d)) ranged from 5 to 25 μm in length.

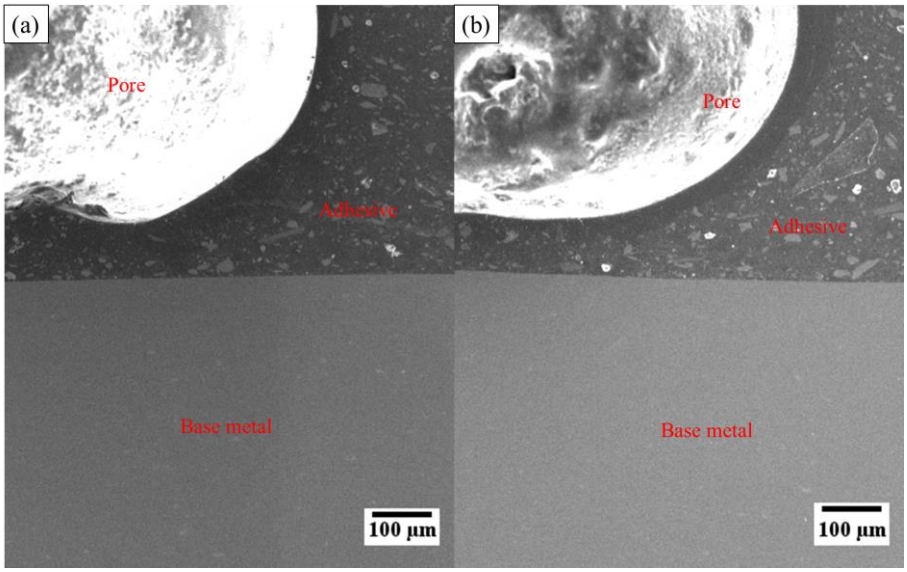

Figure 5.3: Cross-sectional secondary electron images of area A. (a) AA6022, (b) AA6111.

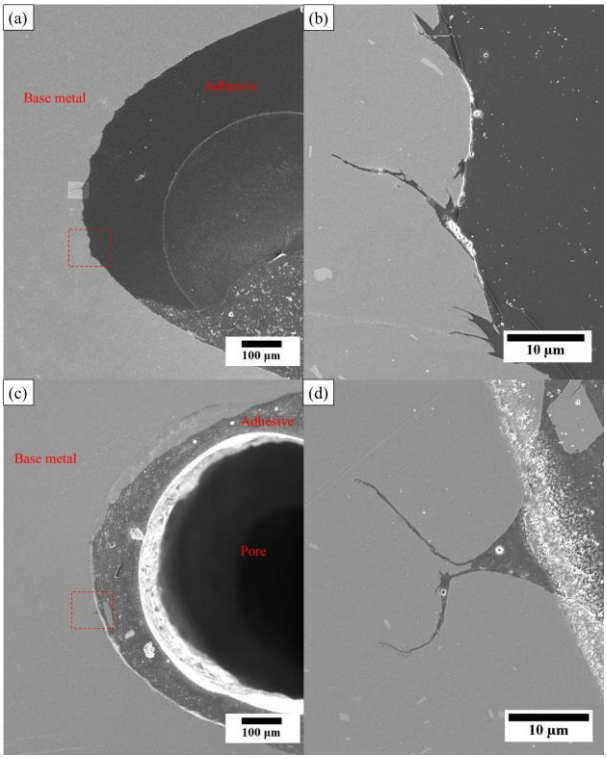

Figure 5.4: Cross-sectional secondary electron images of area B. (a) AA6022, (b) zoomed-in view of area highlighted in (a). (c) AA6022, (d) zoomed-in view of area highlighted in (c).

5.1.2. Hardness Measurements

A set of typical Vicker's hardness (HV) measurements, taken 0.025 mm away from the surfaces and at half-thickness points, of AA6022 and AA6111 hem flange coupons cut in cross-section are shown in Figure 5.5. Due to the significant plastic deformation on the outer sheet, the hardness inner compressive surface at area B was significantly larger than that of area A and area C. Rise in hardness was also observed on the outer tensile surface of the outer sheet due to plastic deformation.

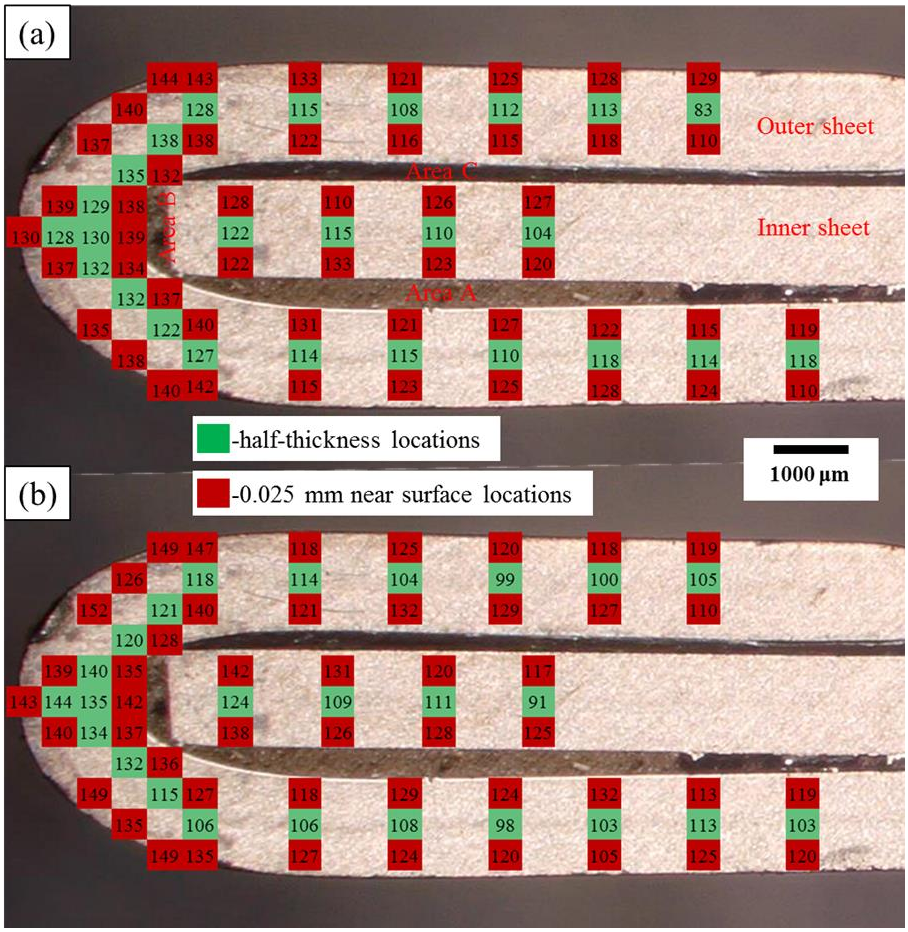

Figure 5.5: Vicker's hardness (HV) measurements of an (a) AA6022 and (b) AA6111 hem flange coupon.

A bar chart summarizing the average hardness, and the 95% CI, of the inner surface of the outer sheet at areas A, B, and C is shown in Figure 5.6. The hardness in area B was significantly higher than that of other areas of the half-thickness location in both alloys.

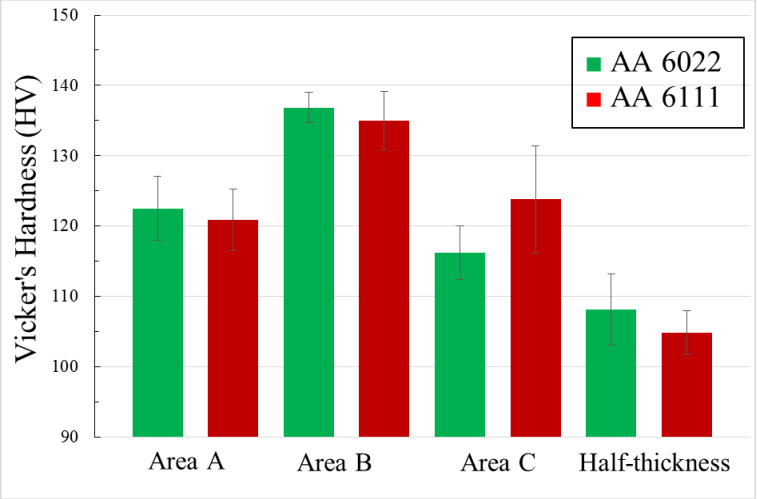

Figure 5.6: Average hardness of the inner surface of the outer sheet at area A, B, and C taken at the half-thickness locations. Errors bars represent the 95% CI.

5.1.3. Chemical Composition and Base Metal Microstructure

The chemical compositions of each alloy, as determined by ICP-OES, is presented in Table 5.1. The major compositional difference between the two alloys was the copper (Cu) concentration; the AA6022 contained 0.1 wt.% Cu, which is referred to as the "Cu-lean" in latter sections, and the AA6111 contained 0.7 wt.% Cu, referred to as "Cu-rich" in subsequent sections.

Table 5.1: Chemical composition (wt%) and 95% CI of AA6022 and AA6111.

Alloy	Si	Mg	Cu	Mn	Fe
6111	0.70 ± 0.02	0.81 ± 0.02	0.70 ± 0.01	0.20 ± 0.01	0.27 ± 0.01
6022	0.90 ± 0.02	0.64 ± 0.02	0.10 ± 0.01	0.10 ± 0.01	0.22 ± 0.01

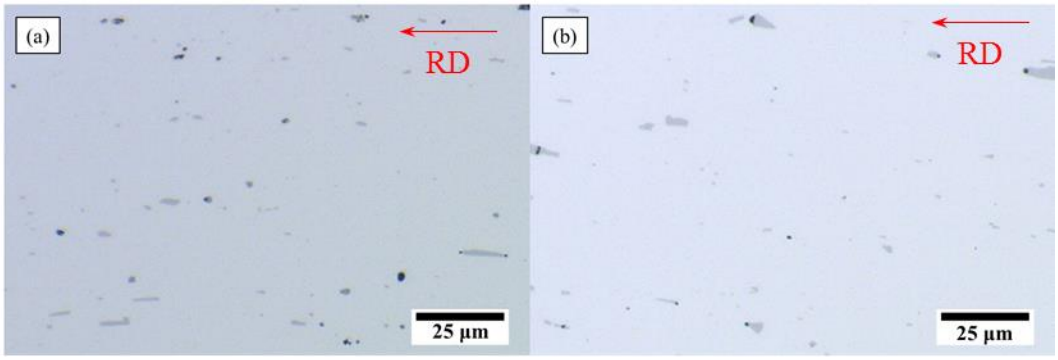

Figure 5.7: Plan-view LOM images of (a) AA6022, and (b) AA6111 revealing coarse intermetallic particles in the inner sheet of both alloys.

Representative LOM images of both alloys are shown in Figure 5.7. Intermetallic particles of various sizes were observed in both alloys. The microstructure was further observed using SEM and analysed using EDS, as shown in Figure 5.8. The corresponding

EDS spectra are shown in Figure 5.9(a), (c) for matrix (blue circles) and Figure 5.9(b), (d) for intermetallic particles (red circles).

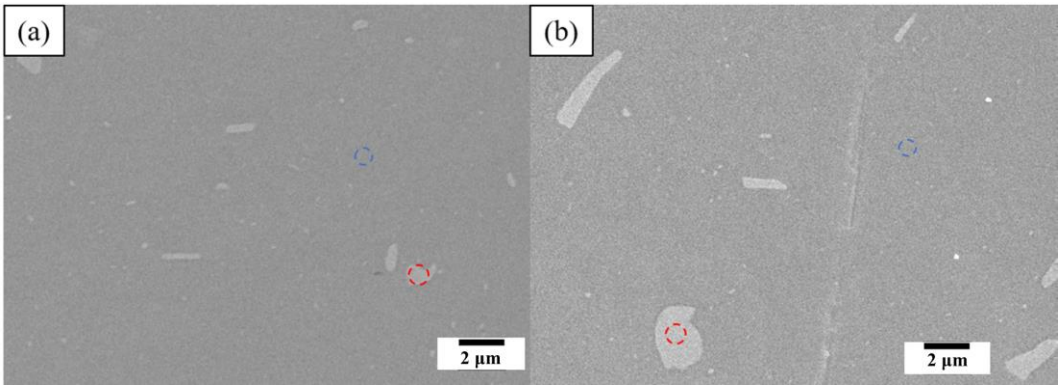

Figure 5.8: Plan-view secondary electron images of (a) AA6022, and (b) AA6111 inner sheet at 8 keV. Sites for EDS analysis are superimposed: red circles for intermetallic particles and blue circles for the Al matrix.

Enrichment of Fe/Mn, Si, and Cu was observed in the intermetallic particles (Figure 5.9(b) and (d)). The level of Cu enrichment was higher in AA6111 than was observed for AA6022. In the case of the AA6022 matrix, all elements except Si and Mg were under the detection limit (Figure 5.9(a)). For the AA6111 matrix, Cu was also detected aside from Si and Mg (Figure 5.9(c)). In all spectra, the peaks at 0.3 keV and 3 keV were due to the carbon coating and silver paint used to prevent samples charging, respectively.

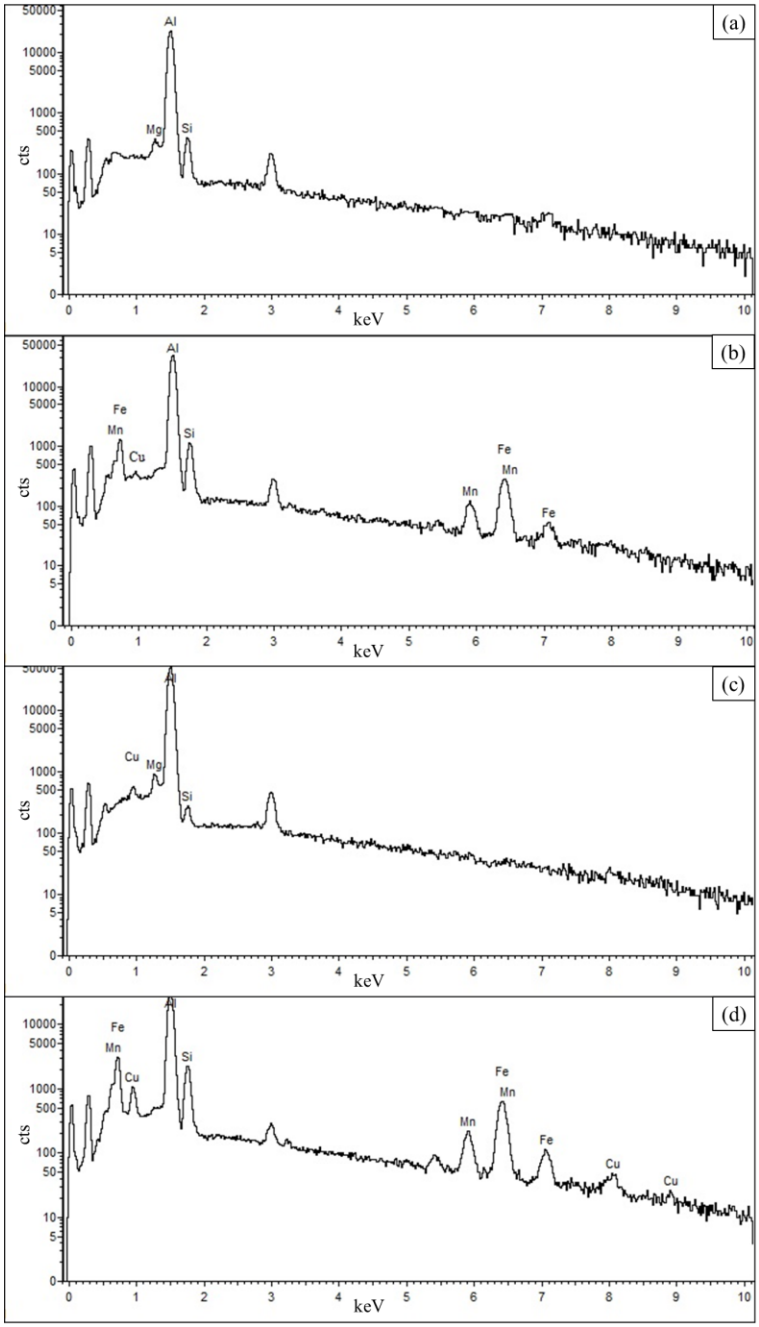

Figure 5.9: EDS spectra (counts vs. keV) of (a) AA6022 matrix and (b) AA6022 inter-metallic particle; (c) AA 6111 matrix and (b) AA6111 intermetallic particle.

5.1.4. Non-destructive Evaluation of the Adhesive Layer

5.1.4.1. Neutron Radiography (NR)

Neutron radiography (NR) was used to characterize the adhesive layer in the hem flange coupons non-destructively. After the neutron radiographic films were generated, they were subsequently digitized. The digitized images were converted to 8-bit greyscale and then a threshold was applied to separate the area of high transmission (air pores) and the area of low transmission (adhesive). After thresholding, the images were converted to 1-bit monochrome images where the air pores are shown in black and the adhesive in white. Only one thresholding algorithm was used for all digitized neutron images in order to ensure consistency [73]. Typical neutron images of AA6022 and AA6111 hem flange coupons and the associated images after thresholding are shown in Figure 5.10 and Figure 5.11, respectively. The adhesive coverage fraction (ACF) was determined by the ratio of white pixels (adhesive) to the total number of pixels within the analyzed area. Subsequently, the effective contact area of each coupon could be calculated by multiplying the total area (500 mm^2) and the adhesive coverage fraction. Sample calculations are shown in Equations (5.1) and (5.2).

$$\text{Adhesive Coverage Fraction (ACF)} = \frac{\#\ of\ white\ pixel}{\#\ of\ total\ pixel} = \frac{102{,}375}{262{,}500} = 0.39 \quad (5.1)$$

$$\text{Effective Contact Area} = \text{Total Area} \times \text{ACF} = 500\ mm^2 \times 0.39 = 195\ mm^2 \quad (5.2)$$

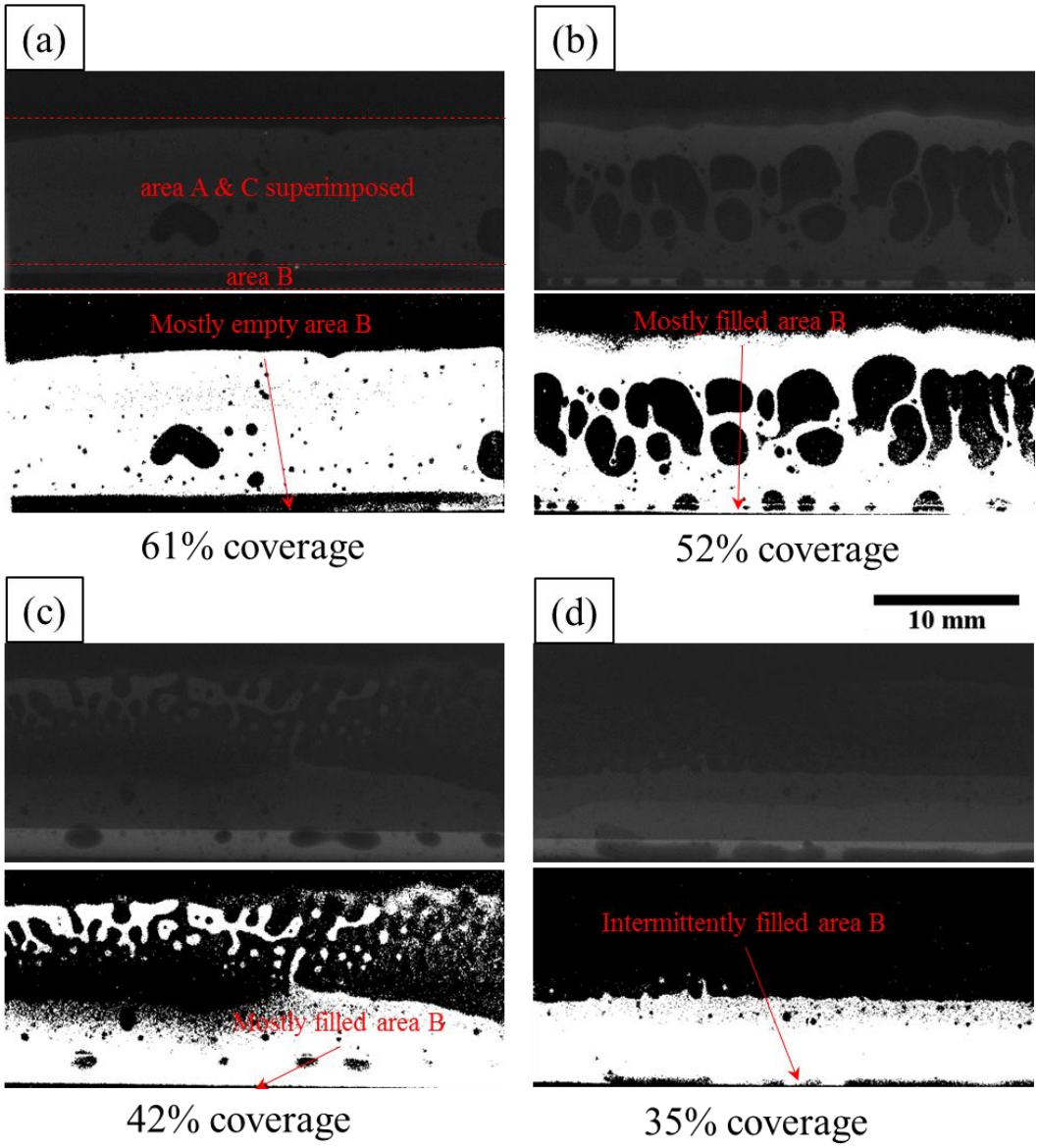

Figure 5.10: Typical neutron images of AA6022 hem flange coupons and the associated images after thresholding.

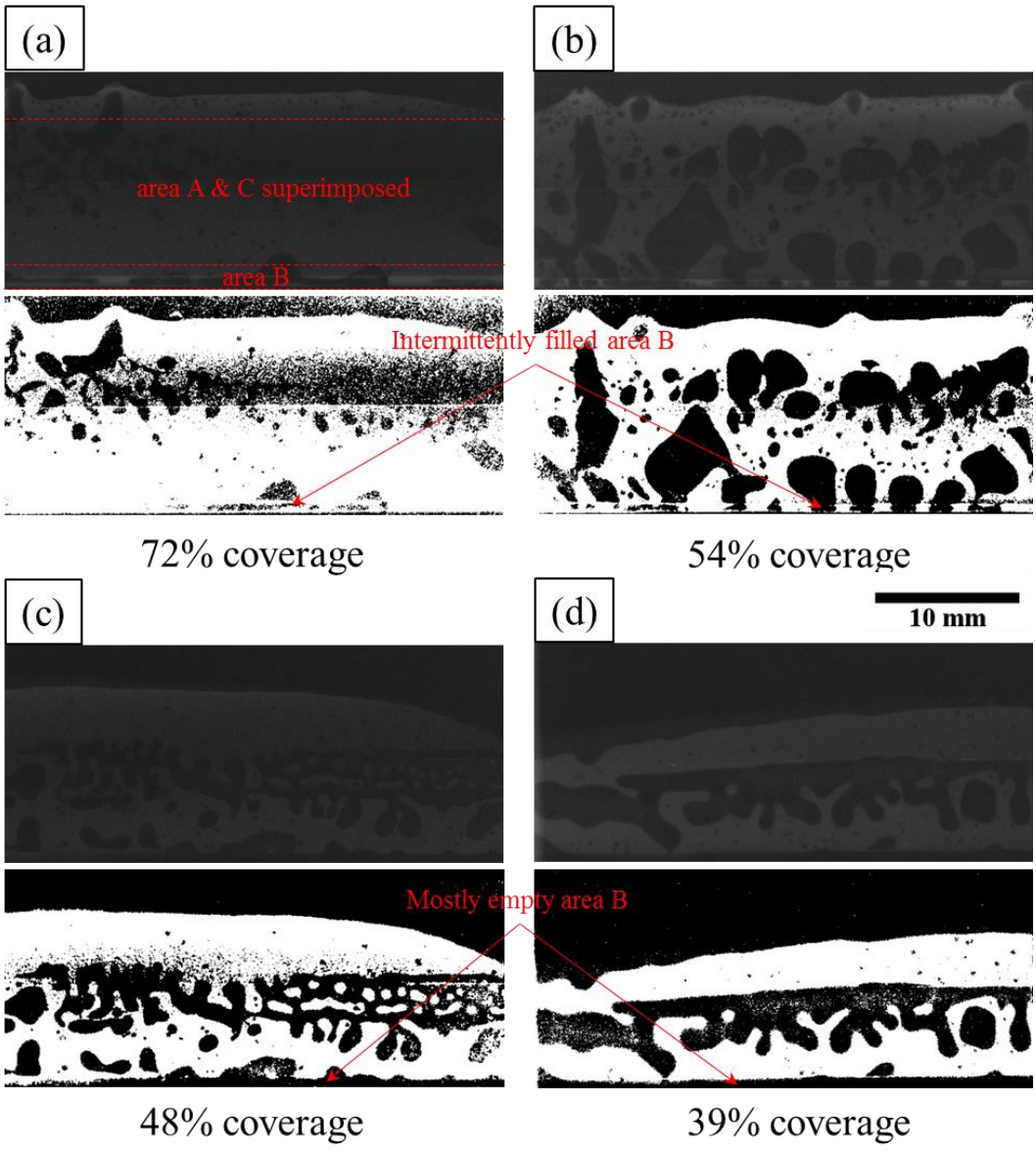

Figure 5.11: Typical neutron images of AA6111 hem flange coupons and the associated images after thresholding.

Due to NR being a two-dimensional imaging technique, the neutron radiographs represent the two-dimensional projection of a three-dimensional hem flange coupon. For this reason, area A and area C of the hem flange were superimposed on the neutron images,

as exemplified in Figure 5.10(a) and Figure 5.11(a). However, due to the lack of adhesive presence in area C, as mentioned in Section 5.1.1. , area C was transparent to the neutron beam and, therefore, did not interfere with the imaging of area A. Area B in the hem flange coupons had various adhesive coverage conditions. Empty "tunnels" were found in the hem flange coupons with intermittently filled or empty area B, Figure 5.10(a) (d) and Figure 5.11.

The neutron images, Figure 5.10 and Figure 5.11, revealed a large variation in the ACF as well as a wide distribution in the size and shape of the air pores. The average ACF value of the AA6022 hem flange coupons was 0.58±0.02, and AA6111 hem flange coupons was 0.55±0.02; thus, there was no significant difference between the ACF for the two sets of hem flange coupons.

5.1.4.2. Characterization of Air Pore Connectivity by Gadolinium(III) Nitrate ($Gd(NO_3)_3$)

Due to the high neutron attenuation coefficient of Gd^{3+}, a $Gd(NO_3)_3$ solution serves as an effective contrast enhancement agent in NR for imagining small crevices or holes. The extent of $Gd(NO_3)_3$ solution ingress into the hem flange coupon provided a qualitative determination of the connectivity of the pores in the adhesive layer. Neutron images of a sub-set of AA6022 and AA6111 hem flange coupons with $Gd(NO_3)_3$ solution ingress (as-exposed) are shown in Figure 5.12 and Figure 5.13 , respectively; the associated images without $Gd(NO_3)_3$ solution ingress (as-received) are included for reference.

On the neutron images, Figure 5.12 and Figure 5.13, the pore network that appears white were filled with the $Gd(NO_3)_3$ solution, indicating that ingress of the solution had occurred. Various degrees of pore connectivity were observed. Figure 5.12 (a) and Figure 5.13(a) and (b) show examples of an interconnecting pore network that exposed both areas A and area B to the $Gd(NO_3)_3$ solution. Figure 5.12(b) shows an interconnecting pore network that exposed just area A to solution ingress. Figure 5.12(c) and Figure 5.13(c) show examples where an interconnecting pore network was not present at all, as exemplified by the lack of $Gd(NO_3)_3$ solution ingress.

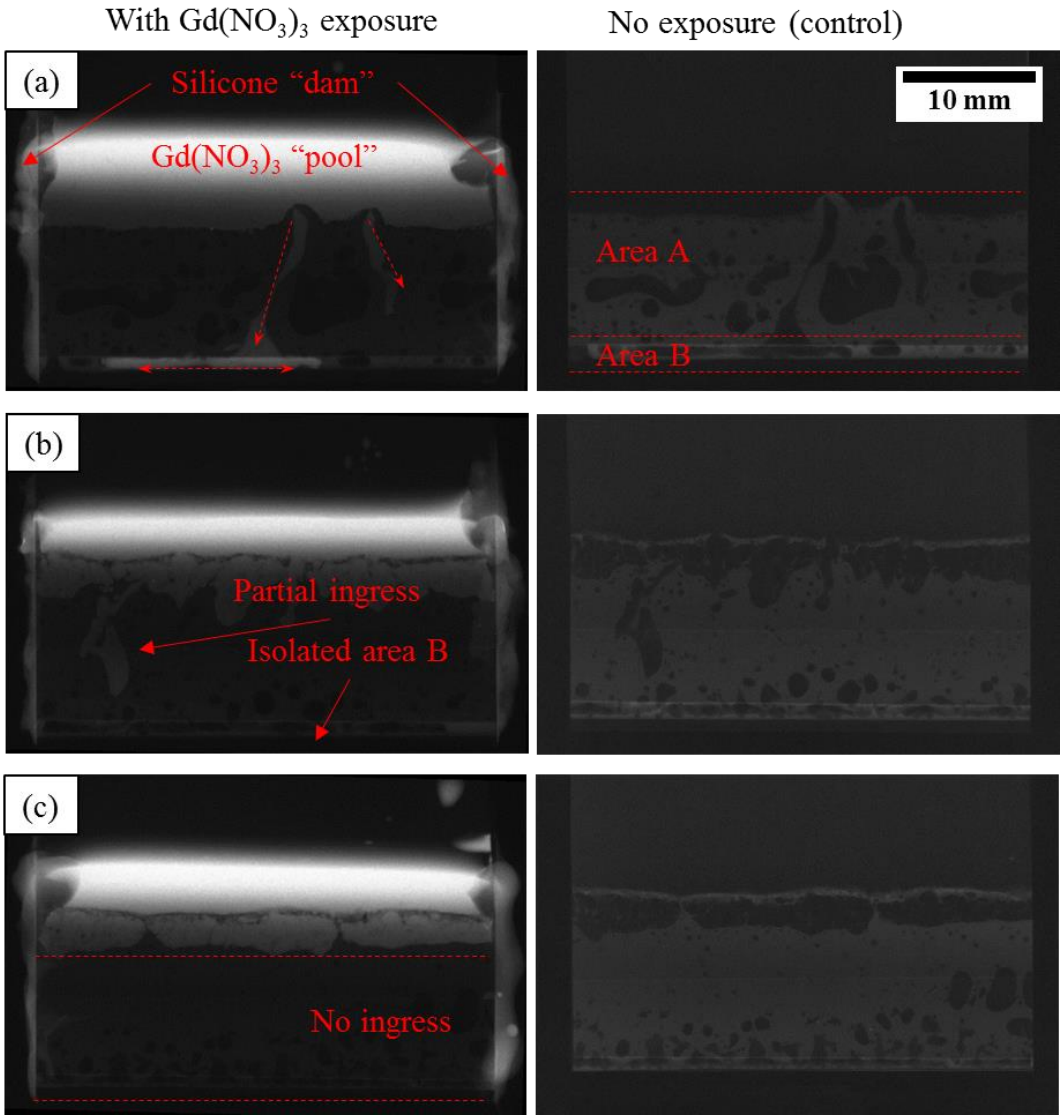

Figure 5.12: Neutron images of AA6022 hem flange coupons filled with $Gd(NO_3)_3$ solution showing various extents of solution ingress through an interconnected pore network: (a) both areas A and B showing solution ingress, (b) area A showing solution ingress and (c) neither areas A nor B showing ingress.

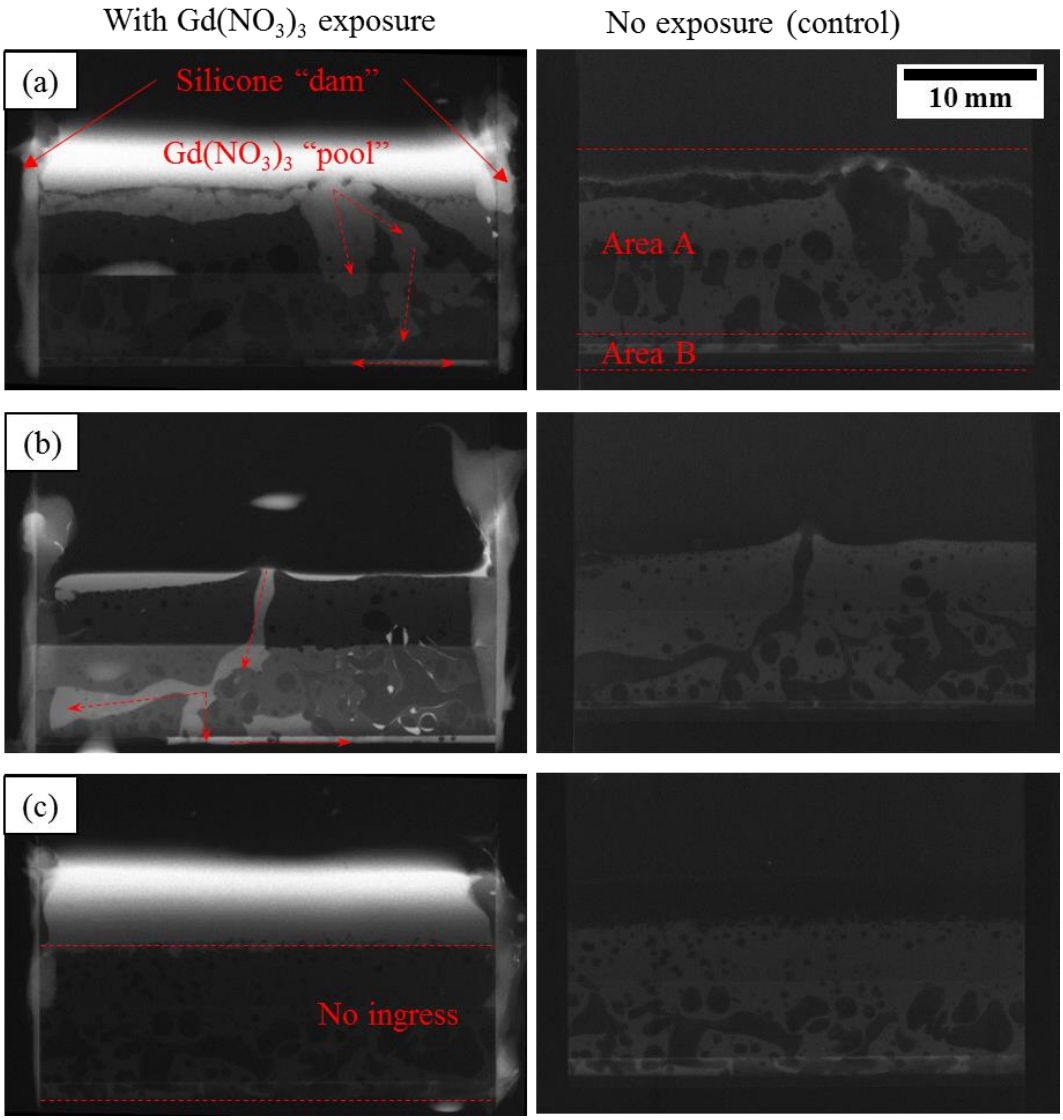

Figure 5.13: Neutron images of AA6111 hem flange coupons filled with $Gd(NO_3)_3$ solution showing various extents of solution ingress through an interconnected pore network: (a) and (b) both areas A and B showing solution ingress, (c) neither are A nor B exposed

5.1.4.3. X-Ray Computed Tomography (CT)

A direct comparison between a 2D neutron image and a reconstructed 3D model from X-ray CT is shown in Figure 5.14. The size, shape and location of the pores in both images were consistent. The existence of an empty "tunnel" in area B, which was established previously by NR, was confirmed by X-ray CT. By applying a volumetric analysis to the reconstructed 3D model, it was determined that the total volume fraction of the adhesive was 0.62 (0.38 pore volume fraction). By applying thresholding method to the neutron image, it was determined that the ACF was 0.64, which is consistent with the total volume fraction of the adhesive determined by the X-ray CT technique.

The X-ray CT technique did not serve as an analytical tool that can be applied to all of the coupons in this work. However, the result from X-ray CT (Figure 5.14(c) and (d)) did confirm the result from NR technique (Figure 5.14(a)), which was applied to all of the coupons in this work. Therefore, the role of X-ray CT in this work can be viewed as a validation to NR in this work.

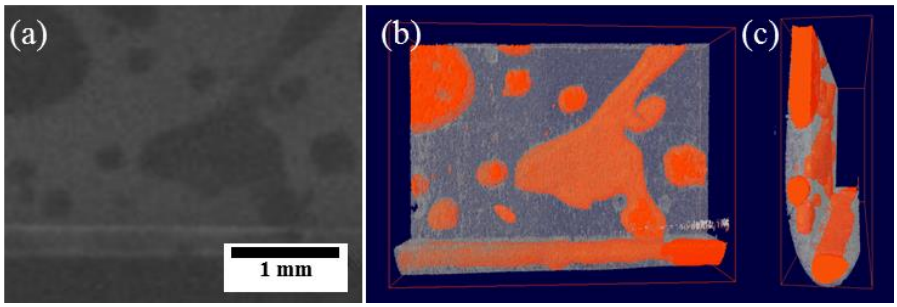

Figure 5.14: (a) Neutron image of a small section of an AA6111 hem flange coupon. (b) Reconstructed 3D model from X-Ray CT scans for the same area. (c) Side view of (b). Air pores are shown in orange and the adhesive is shown in light grey.

5.1.5. Potentiodynamic Polarization Behaviour of the Base Metal

Typical potentiodynamic polarization curves for samples taken from the AA6022 and AA6111 inner sheet normal plane after 10 minutes of immersion at the open circuit condition are presented in Figure 5.15. Typical potentiodynamic polarization curves for the tensile outer surface of AA6022 and AA6111 outer sheets after 10 minutes of immersion at the open circuit condition are presented in Figure 5.16.

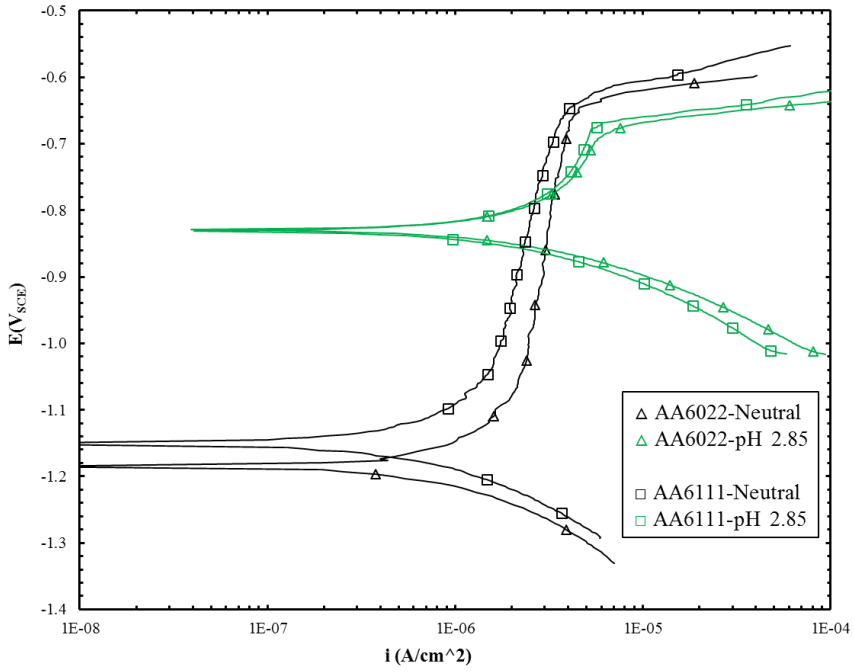

Figure 5.15: Typical potentiodynamic polarization curves for AA6022 and AA6111 in 0.1 M deaerated neutral and pH 2.85 NaCl solution.

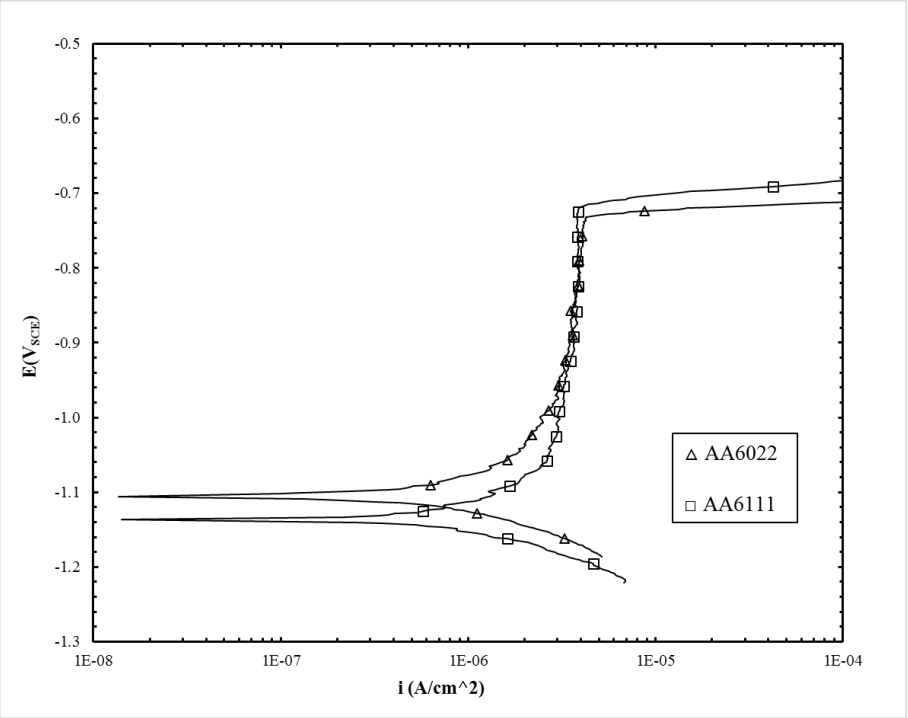

Figure 5.16: Typical potentiodynamic polarization curves for the tensile outer surface of AA6022 and AA6111 outer sheet in 0.1 M deaerated neutral NaCl solution.

The detailed statistics of the potentiodynamic polarization curves are shown in Figure 5.17. The average values and corresponding 95% CI as error bars of the breakdown potential (E_b), corrosion potential (E_{corr}) and corrosion current density (i_{corr}) were calculated based on at least three repetitions of the polarization test. For the un-deformed AA6022 and AA6111 samples (Figure 5.17(a) and (b)), the acidic condition reduced the passivation window by increasing the OCP of both alloys from approximately -1.15 to -0.82 V_{SCE}, whereas the breakdown potential, E_b, remained unchanged. The acidification also increased the cathodic and anodic current density by approximately 300%. The E_b and E_{corr} values of AA6022 and AA6111 were not significantly different for all experimental conditions.

AA6111 had slightly higher i_{corr} value than that of AA6022; (0.561 ± 0.05) μA/cm^2 vs. (0.532 ± 0.04) μA/cm^2 in the neutral condition, and (2.103 ± 0.08) μA/cm^2 vs. (1.973 ± 0.08) μA/cm^2 in the acidic condition.

For the AA6022 and AA6111 tensile outer surface samples (Figure 5.17(c)), E_b values were slightly lower than that of the un-deformed samples (-0.73 V_{SCE} vs. -0.65 V_{SCE}). A slight increase of the i_{corr} values were also observed on both alloys compared to the un-deformed samples.

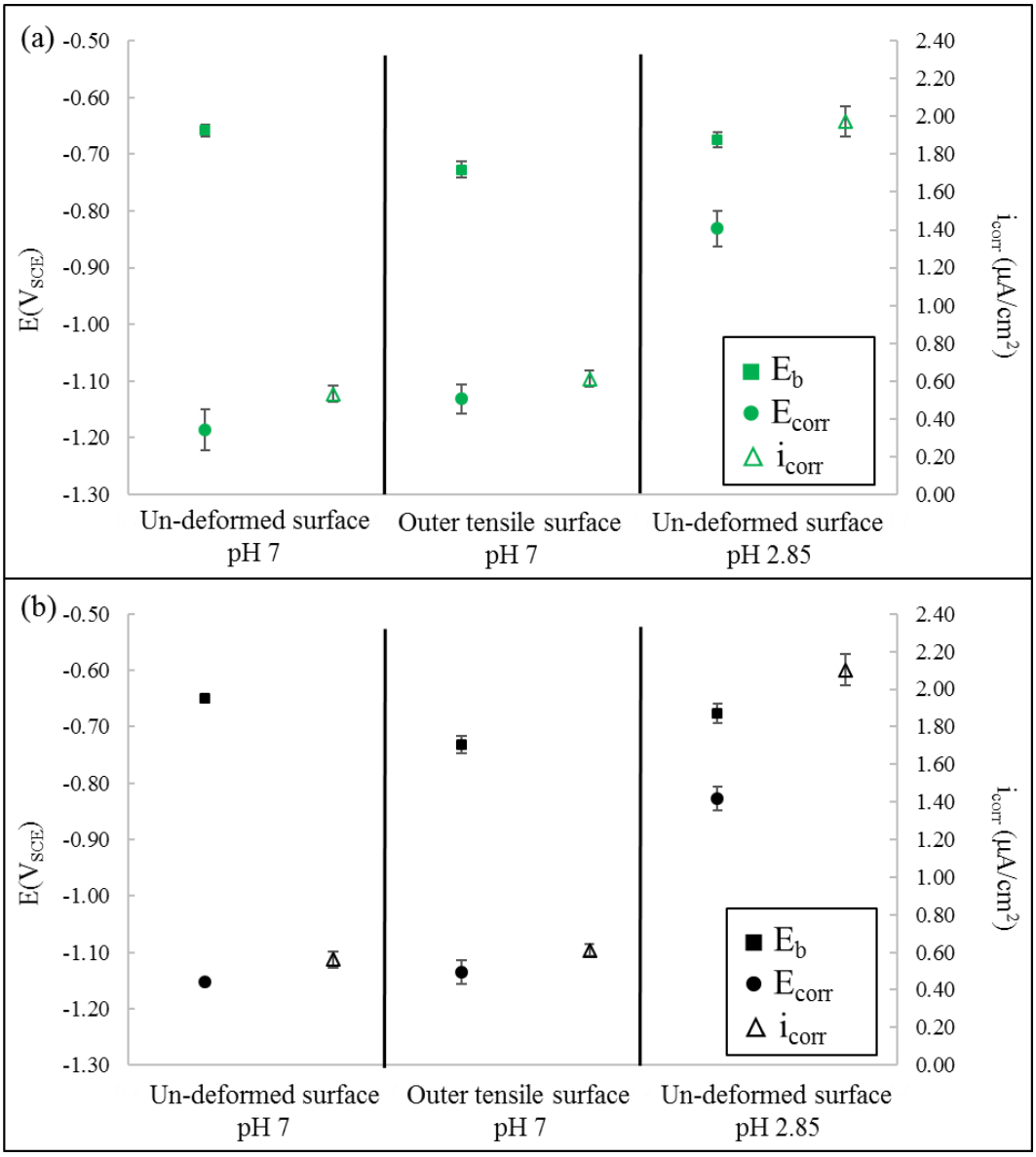

Figure 5.17: Statistics of breakdown potential (E_b), corrosion potential (E_{corr}), and average corrosion current density (i_{corr}) of (a) un-deformed surface (pH 7 and 2.85) and outer tensile surface of AA6022, and (b) un-deformed surface (pH 7 and 2.85) and outer tensile surface of AA6111 in 0.1 M NaCl solution.

5.2. Effects of Cyclic Corrosion and Cyclic Deformation

5.2.1. Cyclic Corrosion Damage

Typical plan-view images of hem flange coupons after a six-week and twelve-week Ford L-3190 cyclic corrosion exposure are shown in Figure 5.18, respectively. No corrosion damage was observed on the outer surfaces of both the inner and outer sheet for both exposure durations and all coupons.

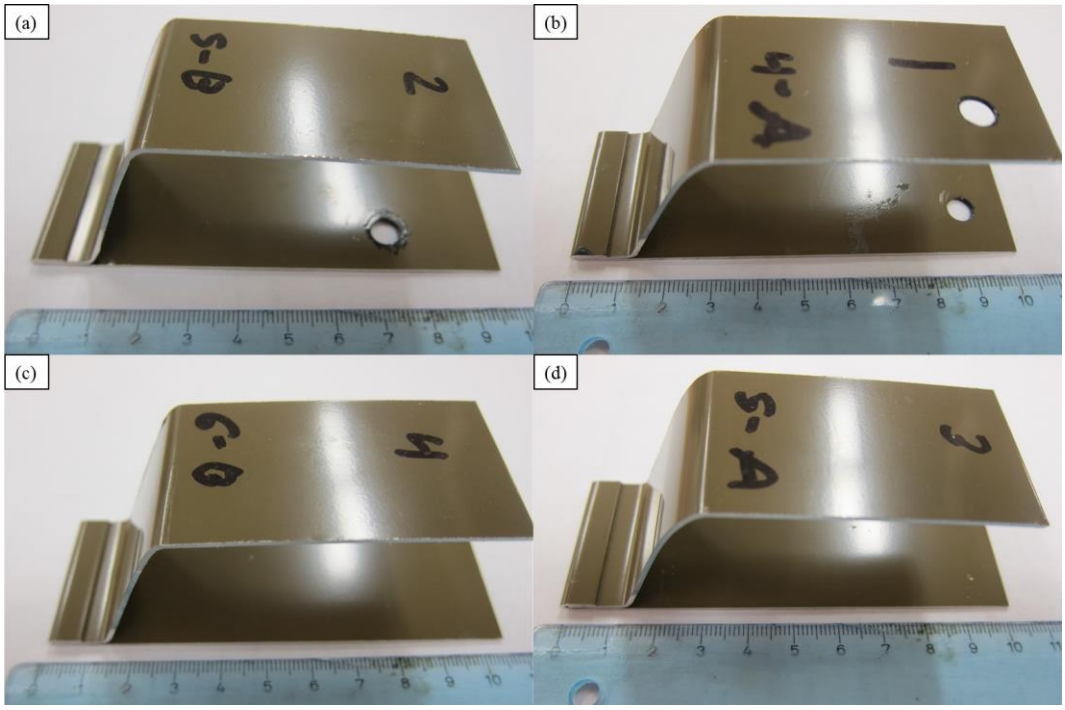

Figure 5.18: Photographs of hem flange coupons (a) AA6022 and (b) AA6111 after six-week Ford L-3190 cyclic corrosion exposure; (c) AA6022 and (d)AA6111 after twelve-week Ford L-3190 cyclic corrosion exposure.

Typical cross-sectional LOM images of the AA6022 and AA6111 hem flange coupons after six and twelve weeks of Ford L-3190 exposure are shown in Figure 5.19 and Figure 5.20, respectively. Only minor pitting damage was observed for both AA6022 and AA6111, where the corrosion damage was restricted to the inner surface of the outer sheet (area B). No corrosion damage was found in area A and area C for either alloy. No corrosion damage was found in area D associating with the intentionally placed burr for either alloy.

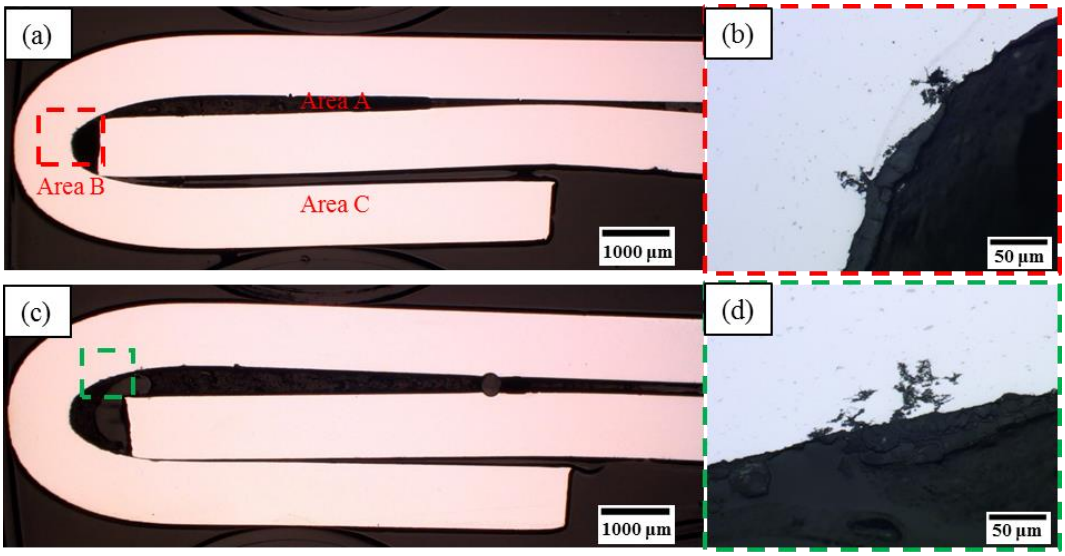

Figure 5.19: Cross-sectional LOM images of hem flange coupons after six weeks of Ford L-3190 exposure (a) AA6022 hem flange coupon, (b) higher magnification view of red frame; (c) AA6111 hem flange coupon and (d) higher magnification view of green frame.

In the coupons exposed for twelve weeks, the corrosion damage was more extensive in the affected area for both alloys. As was observed for the six-week coupons, the majority of the corrosion damage was found in area B. Minor corrosion damage was found in area

C and on the inner sheet adjacent to area B, as shown in Figure 5.20(e) and (f). Intergranular corrosion (IGC) was observed for both alloys. The IGC in AA6111 was more pronounced. No corrosion damage was found in area D associating with the intentionally placed burr for either alloy.

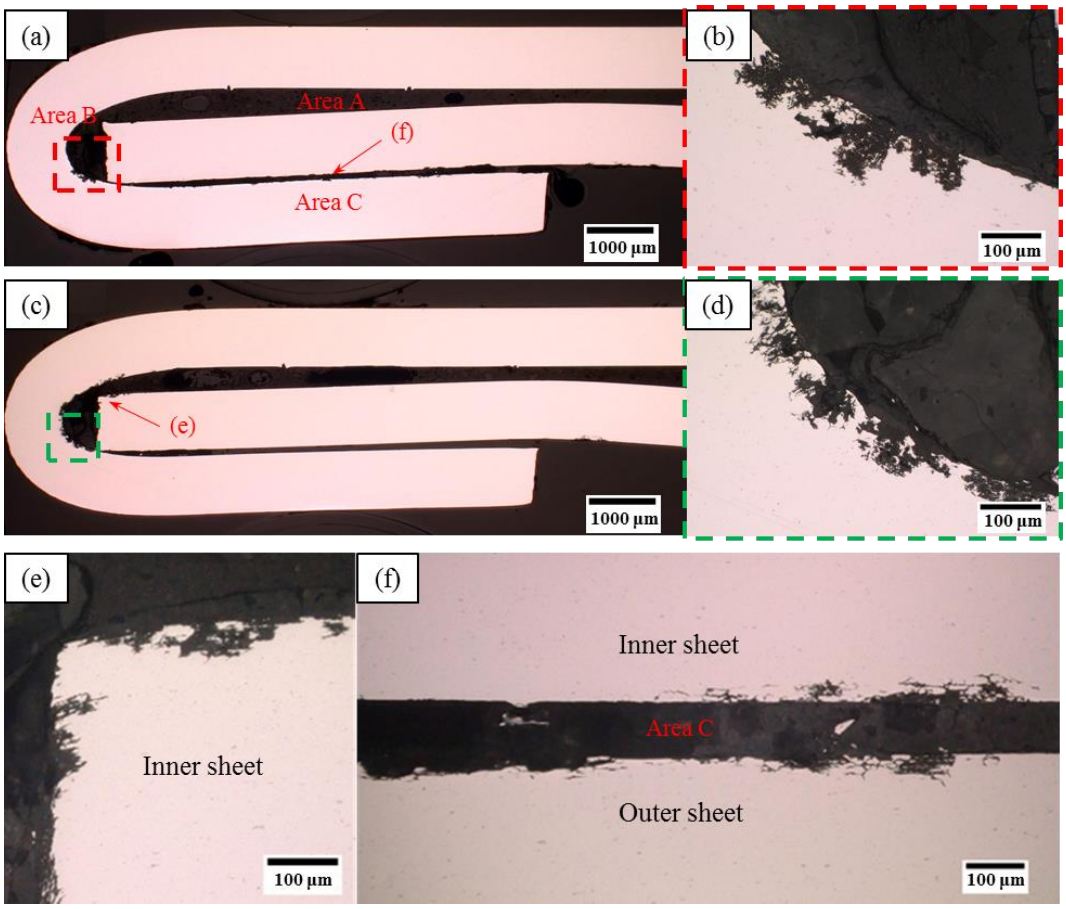

Figure 5.20: Cross-sectional LOM images of hem flange coupons after twelve weeks of Ford L-3190 exposure (a) AA6022 hem flange coupon, (b) higher magnification view of red frame; (c) AA6111 hem flange coupon, (d) higher magnification view of green frame; (e) higher magnification of AA6111 inner sheet adjacent to area B and (f) higher magnification of AA6111 inner sheet adjacent to area C.

The cross-sectional LOM images of the scribe in area D is shown in Figure 5.21. Minor pitting damage was observed in the six-week coupons (Figure 5.21(a) and (c)). Deeper pitting damage and minor IGC were observed in the twelve-week coupons (Figure 5.21(b) and (d)). No corrosion creepage under the coating layer was observed in any of the coupons. Due to the low depth of corrosion attack on the scribe areas, no obvious difference was observed between AA6022 coupons and AA6111 coupons

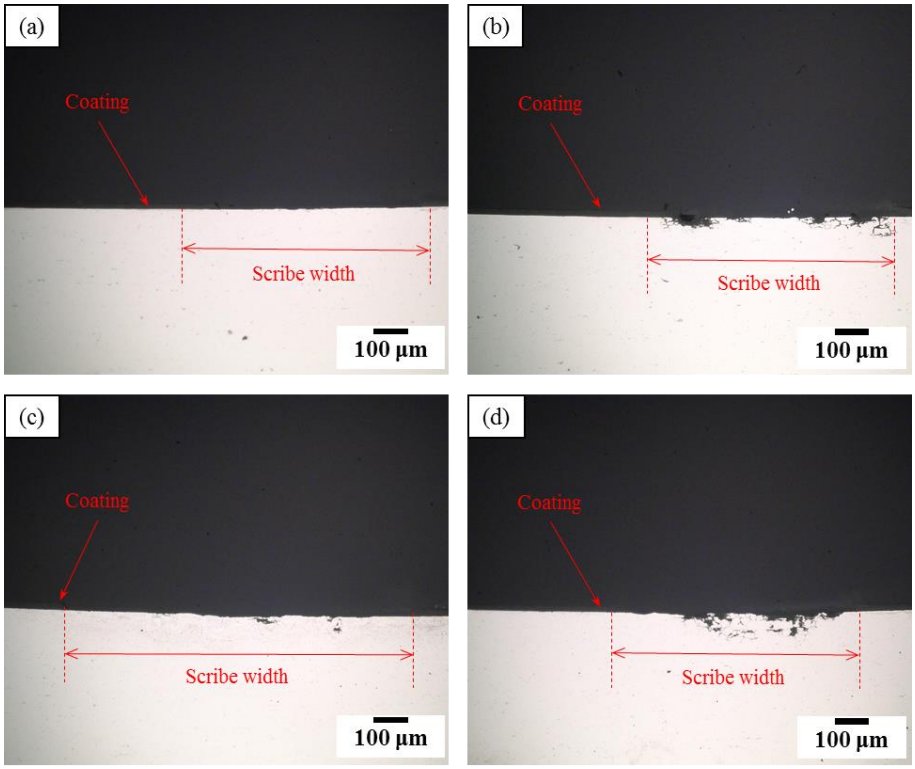

Figure 5.21: Cross-sectional LOM images of the scribe in area D. (a) AA6022 hem flange coupon after six-week exposure, and (b) after twelve-week exposure; (c)AA6111hem flange coupon after six-week exposure, and (d) after twelve-week exposure.

The maximum depth of attack found on the inner surface of the outer sheet at area B for both alloys is summarized in Figure 5.22. For both exposure times, the AA6111 coupons had a significantly deeper depth of attack (on average) relative to the AA6022 coupons, which indicates that AA6111 was more susceptible to corrosion in this test.

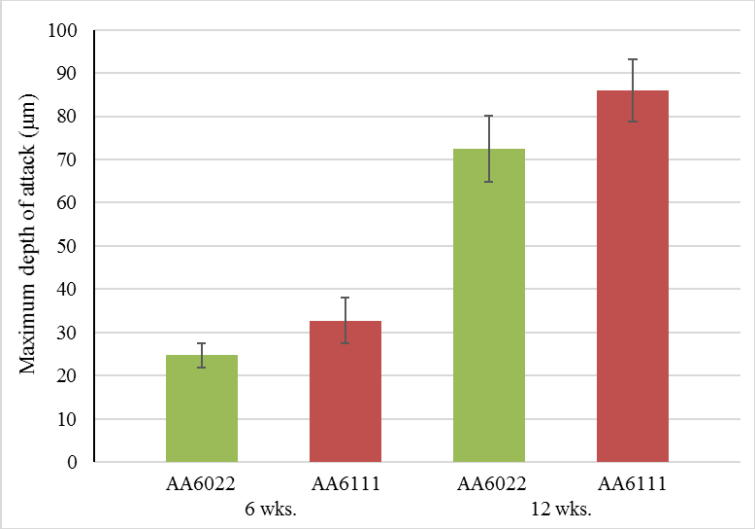

Figure 5.22: Maximum depth of attack in area B of AA6022 and AA6111 hem flange coupons after six and twelve weeks of Ford L-3190 exposure. Error bars represent 95% CI.

The maximum depth of attack found on the scribe of the outer sheet at area D for both alloys is summarized in Figure 5.23. For twelve-week exposure, the maximum depth of attack in scribed area D was lower than that of area B with six-week exposure. No statistical difference on the depth of attack was found between the two alloys.

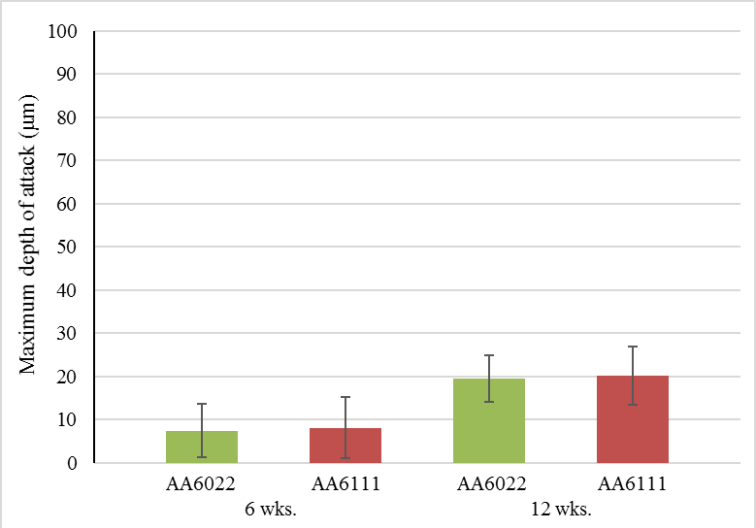

Figure 5.23: Maximum depth of attack in area D of AA6022 and AA6111 hem flange coupons after six and twelve weeks of Ford L-3190 exposure. Error bars represent 95% CI.

5.2.2. Cyclic Deformation Damage

During the cyclic deformation testing, the maximum and minimum loads on the hem flange were recorded every cycle. The load value was converted to a nominal stress based on the effective contact area (Equation 5.2) of each hem flange coupon, as determined using NR imaging. A sample calculation of the load converting to a nominal stress is shown in Equation (5.3).

$$\text{Nominal Stress} = \frac{Max.\ load - Min.load}{Effective\ contact\ area} = \frac{91.5\ N - 4.1\ N}{305\ mm^2} = 0.28\ MPa \qquad (5.3)$$

The nominal stress versus cycle curves for a triplicate set of as-received AA6022 and AA6111 hem flange coupons are shown in Figure 5.24. The corresponding side-view LOM images of each coupon after 0 cycles and 250,000 cycles are shown in Figure 5.25 (for AA6022 coupons) and Figure 5.26 (for AA6111 coupons).

The displacement cycle from 0 to +2 mm required the application of an initial nominal stress ranging from 0.3 MPa to 0.4 MPa. In general, the applied nominal stress decreased gradually with increasing cycle count. From Figure 5.24, it can be seen that AA6022 coupon #2 had a higher rate of stress decrease near 100,000 cycles, which was not observed for any other coupon. The side-view LOM images of the AA6022 coupon #2, Figure 5.25(c) and (d), revealed a well-developed crack in area B, which was not observed in any other coupon. For other coupons in this set, the cracks propagated through approximately half of area A after 250,000 cycles.

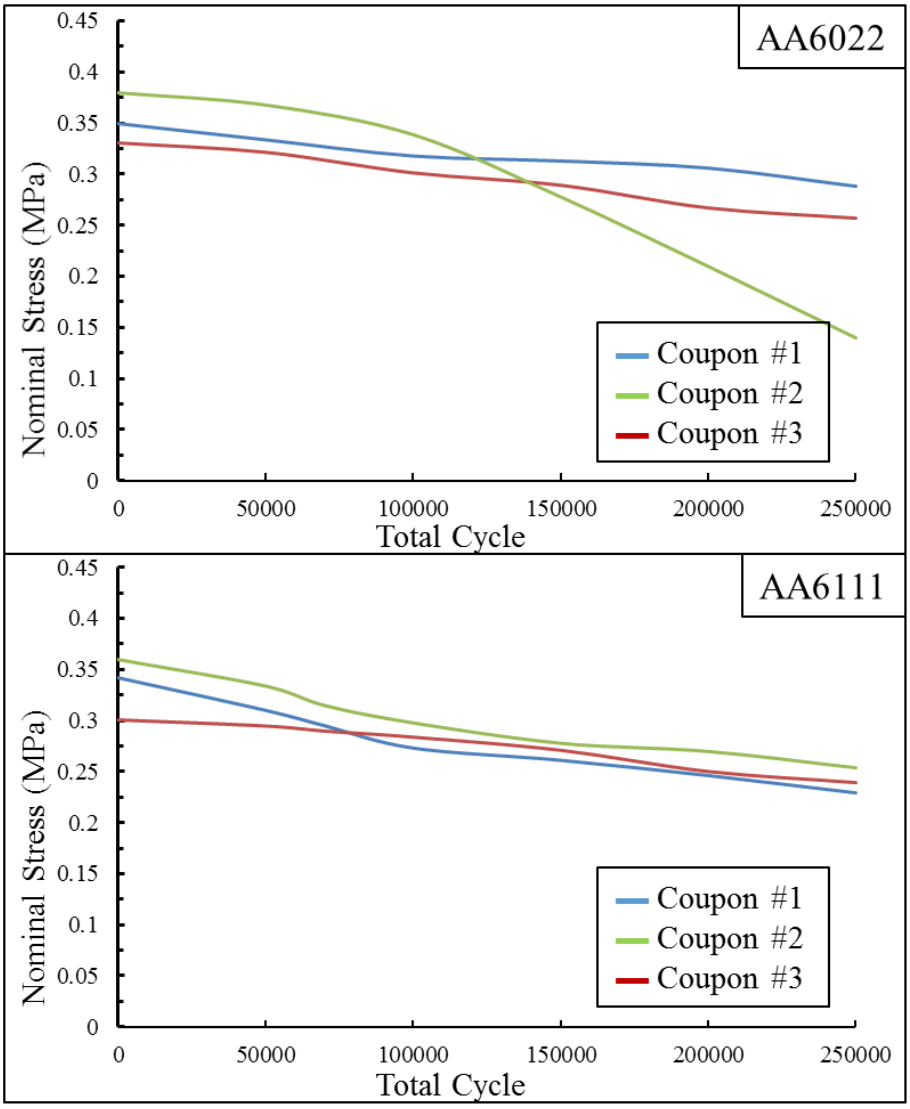

Figure 5.24: Applied nominal stress versus total cycle curves for a triplicate set of as-received AA6022 and AA6111 hem flange coupons.

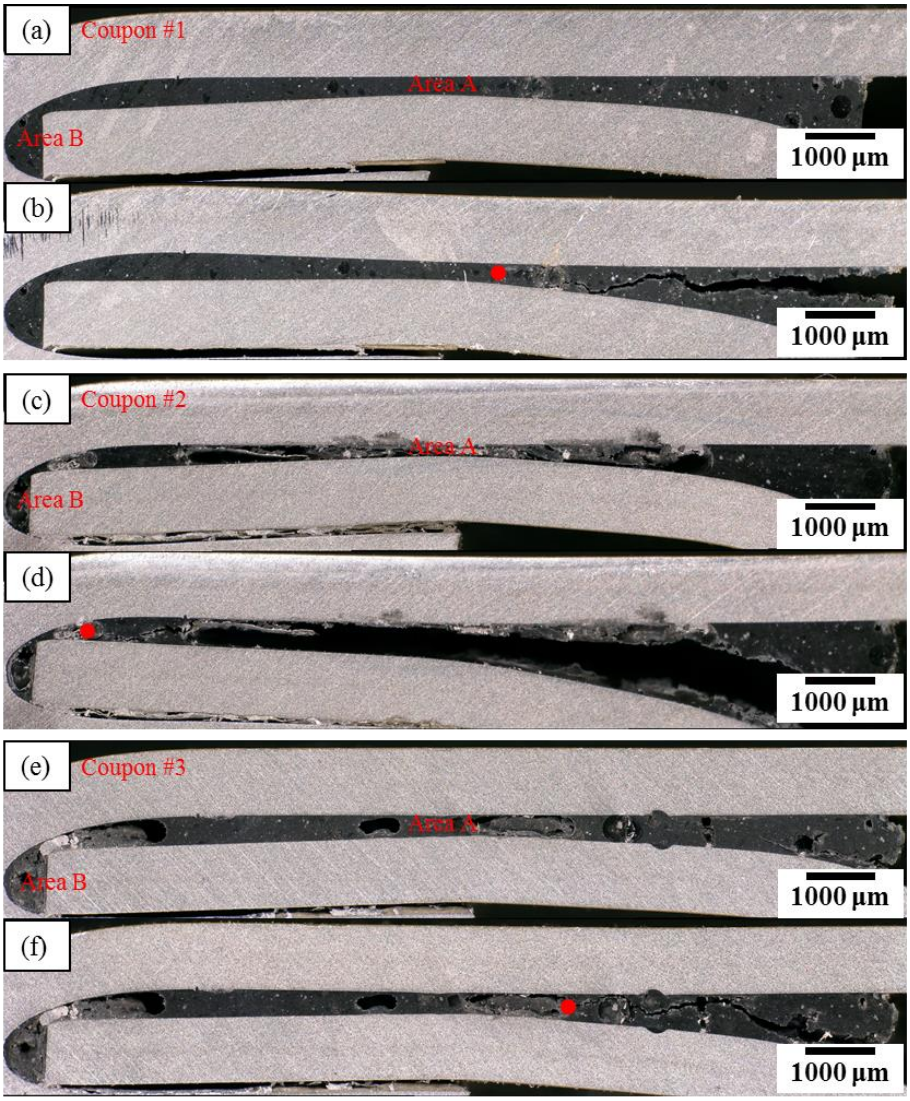

Figure 5.25: Side-view LOM images of the triplicate set of AA 6022 coupons subjected to cyclic deformation: coupon #1 after (a) 0 cycles and (b) 250,000 cycles; coupon #2 at (c) 0 cycles and (d) 250,000 cycles; coupon #3 at (e) 0 cycles and (f) 250,000 cycles. Crack tips are marked by red dots (●).

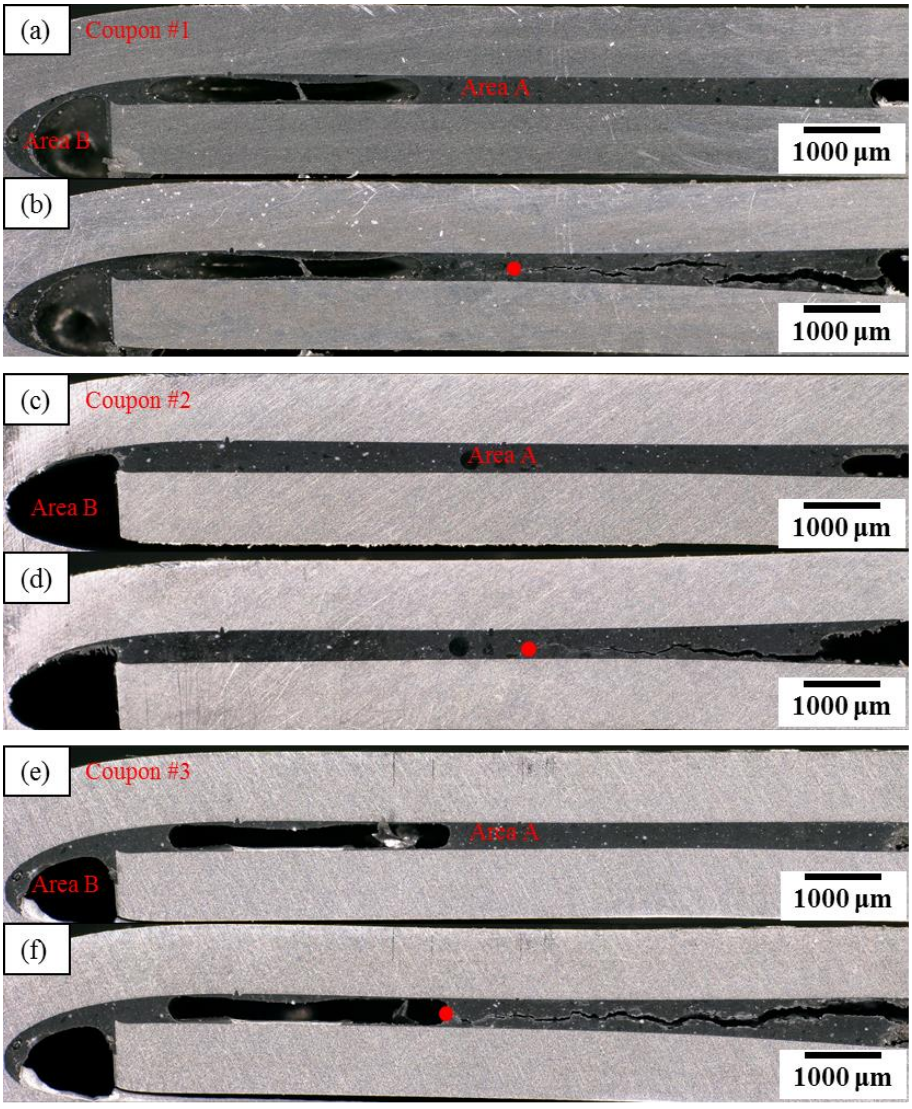

Figure 5.26: Side-view LOM images of the triplicate set of AA6111 coupons subjected to cyclic deformation: coupon #1 after (a) 0 cycles and (b) 250,000 cycles; coupon #2 at (c) 0 cycles and (d) 250,000 cycles; coupon #3 at (e) 0 cycles and (f) 250,000 cycles. Crack tips are marked by red dots (●).

5.3. Combined Effects of Cyclic Corrosion and Cyclic Deformation

5.3.1. Effect of Prior Cyclic Corrosion Followed by Cyclic Deformation

Photographs of a triplicate set of previously corroded (Ford L-3190 for six weeks) hem flange coupons (#4-6) of each alloy are shown in Figure 5.27. No corrosion damage was observed on the outer surface of both the inner and outer sheets of these coupons.

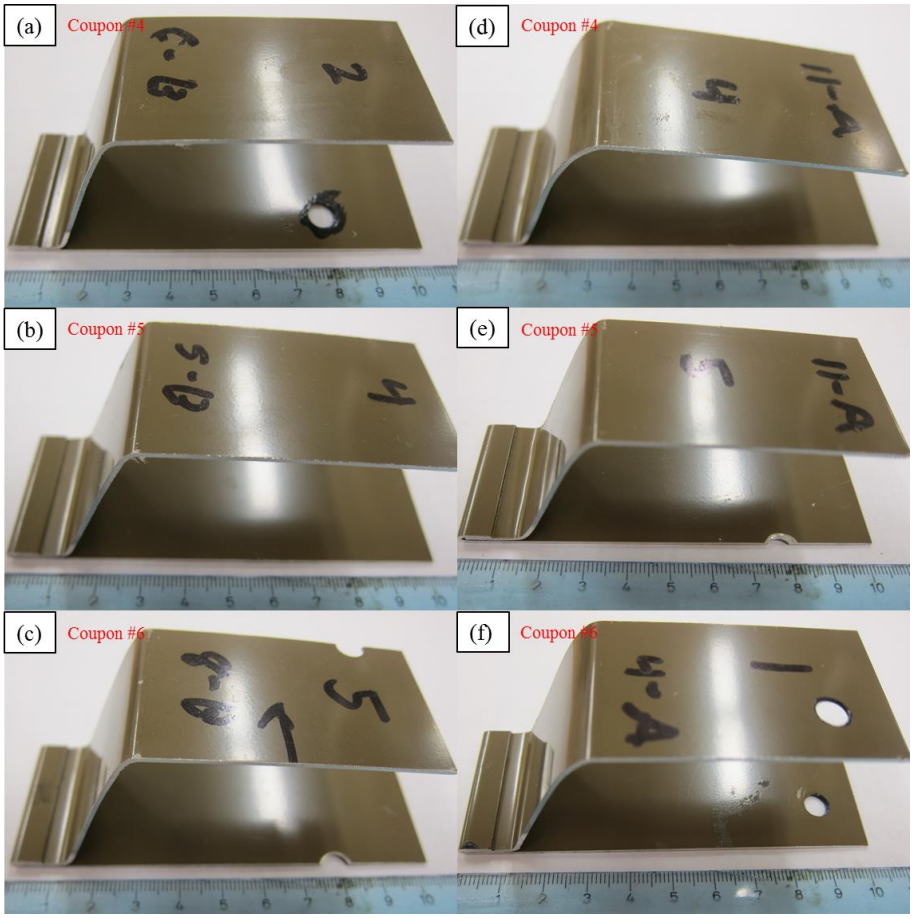

Figure 5.27: Photographs of previously corroded (Ford L-3190 for six weeks) hem flange coupons (#4-6) of (a)-(c) AA6022 and (d)-(f) AA6111.

The nominal applied stress versus cycle curves for these coupons are shown in Figure 5.28. The corresponding side-view LOM images of each coupon after 0 and 100,000

cycles are shown in Figure 5.29 (for the AA6022 coupons) and Figure 5.30 (for the AA6111 coupons).

The initial nominal applied stress of the previously corroded coupons ranged from 0.35 to 0.39 MPa. All coupons exhibited a sharp drop in nominal applied stress before or at approximately 100,000 cycles. In comparison, no sharp drop in nominal applied stress was observed in the as-received coupons. The corresponding side-view LOM images revealed that all samples had cracks which had largely penetrated through the adhesive layer after 100,000 cycles. In comparison, the as-received coupons had significantly lower crack propagation speed.

The six-week exposure reduced the strength of the adhesive, resulted in abrupt drop of nominal applied stress, which indicated the sudden crack opening, as well as an overall higher rate of crack propagation. This set of coupons exhibited different nominal stress drop behaviours. AA6022 coupon #4 and AA6111 coupon #6 had two distinct steps on their nominal stress vs. cycle curves (Figure 5.28), whereas other coupons only had one step. The difference in the observed nominal stress drop behaviours were likely related to the difference in the ACF of each coupon.

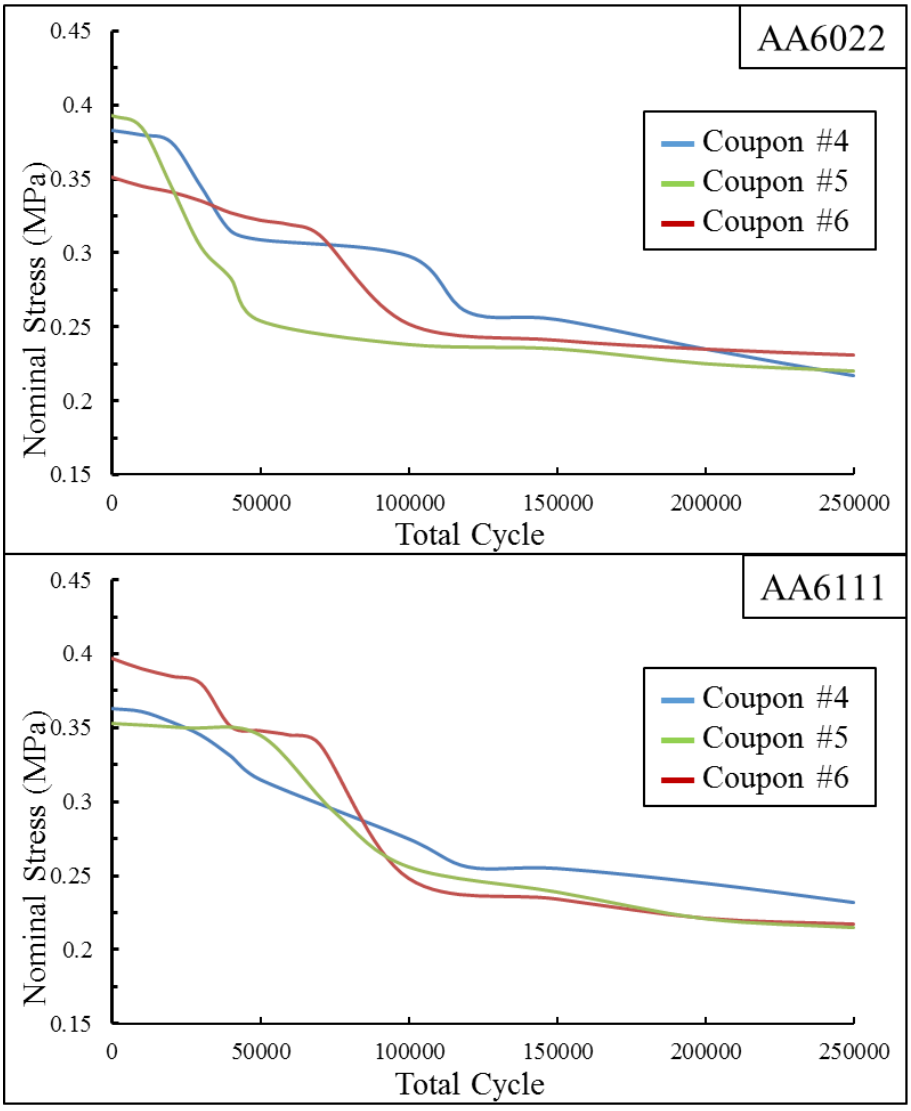

Figure 5.28: Applied nominal stress versus total cycle curves for set of triplicate set of AA6022 and AA6111 hem flange coupons that were previously corroded (Ford L-3190 for six weeks)

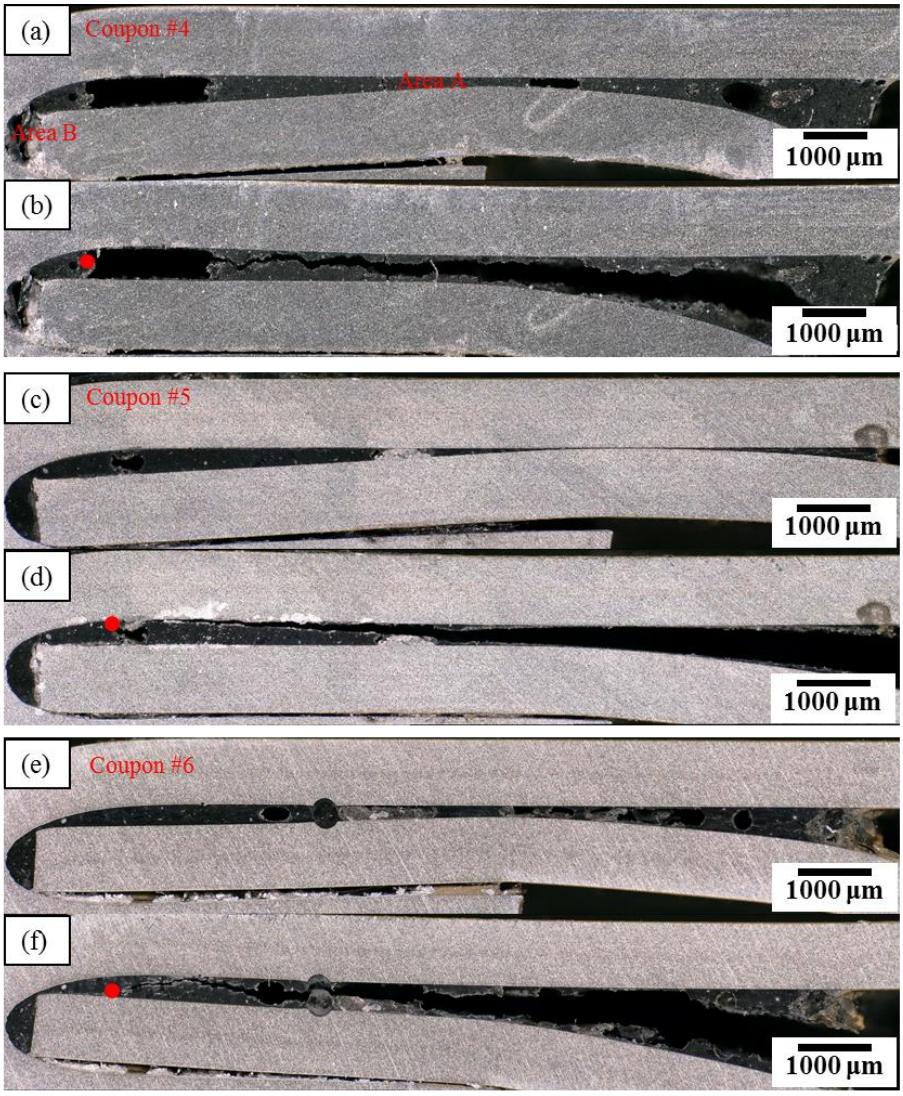

Figure 5.29: Side-view LOM images of the triplicate set of AA6022 coupons that were previously corroded (FORD L-3190 for six weeks): coupon #4 after (a) 0 cycles and (b) 100,000 cycles; coupon #5 after (c) 0 cycles and (d) 100,000 cycles; coupon #6 after (e) 0 cycles and (f) 100,000 cycles. Crack tips are marked by red dots (●).

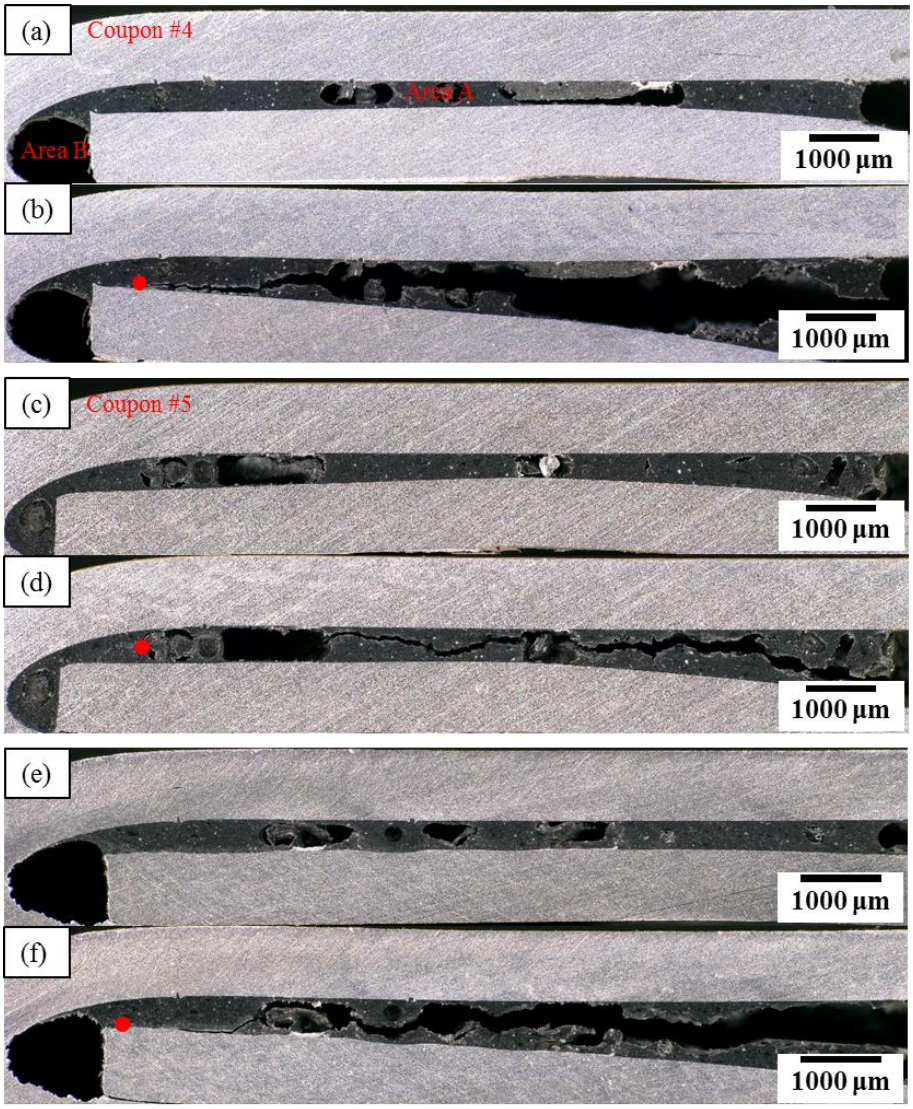

Figure 5.30: Side-view LOM images of the triplicate set of AA6111 coupons that were previously corroded (FORD L-3190 for 6 weeks): coupon #4 after (a) 0 cycles and (b) 100,000 cycles; coupon #5 after (c) 0 cycles and (d) 100,000 cycles; coupon #6 after (e) 0 cycles and (f) 100,000 cycles. The crack tips are marked by red dots (●).

Photographs of a duplicate set of previously corroded (Ford L-3190 for twelve weeks) hem flange coupons (#4-6) of each alloy are shown in Figure 5.31. No corrosion damage was observed on the outer surface of both the inner and outer sheets of these coupons.

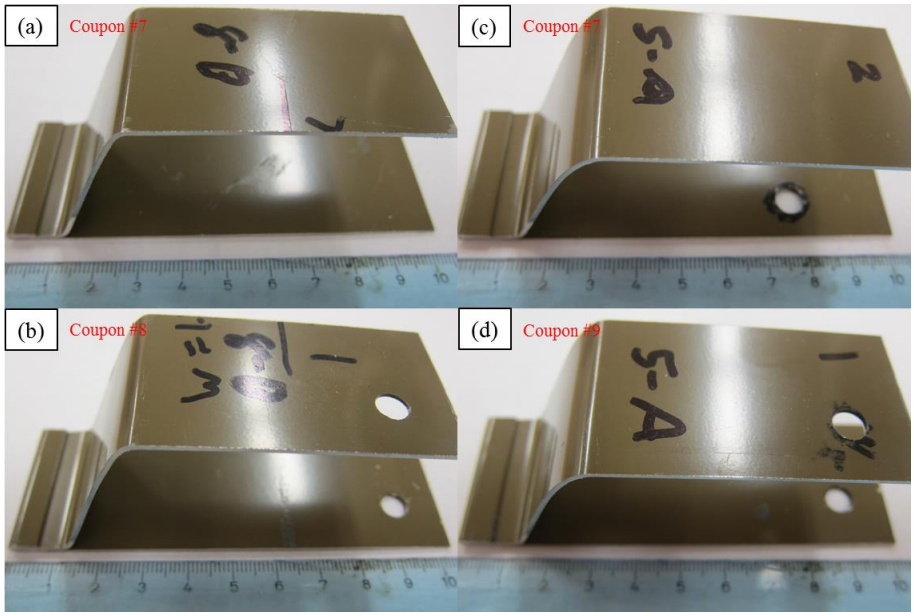

Figure 5.31: Photographs of previously corroded (Ford L-3190 for twelve weeks) hem flange coupons (#7 and #8) of (a), (c) AA6022 and (c), (d) AA6111.

Nominal applied stress versus cycle curves for these coupons are shown in Figure 5.32. The corresponding side-view LOM images of each coupon after 0 and 100,000 cycles are shown in Figure 5.33 (for AA6022 coupons) and Figure 5.34 (for AA6111 coupons).

The initial applied nominal stress for this set of previously corroded coupons varied from 0.36 MPa to 0.40 MPa. All the coupons exhibited a sharp drop in nominal stress before

50,000 cycles. Similar drop in nominal stress was observed to take place around 100,000 cycles for the six-week coupons (Figure 5.28).

The corresponding side-view LOM images revealed that the crack in each case had largely penetrate through the adhesive layer after 100,000 cycles. AA6111 coupon #8 had a clean delamination along the adhesive-metal interface, indicating adhesive failure, Figure 5.34 (d). This mode of failure was not previously observed in coupon #1 – #7. AA6111 coupon #7 had a fracture in the outer sheet after 210,000 cycles.

The twelve-week exposure further decreased the strength of the adhesive comparing with six-week exposure. New mode of failure (Figure 5.34(d)) was observed, which indicated the reduction in the bonding strength between the Al base metal and the adhesive due to cyclic corrosion.

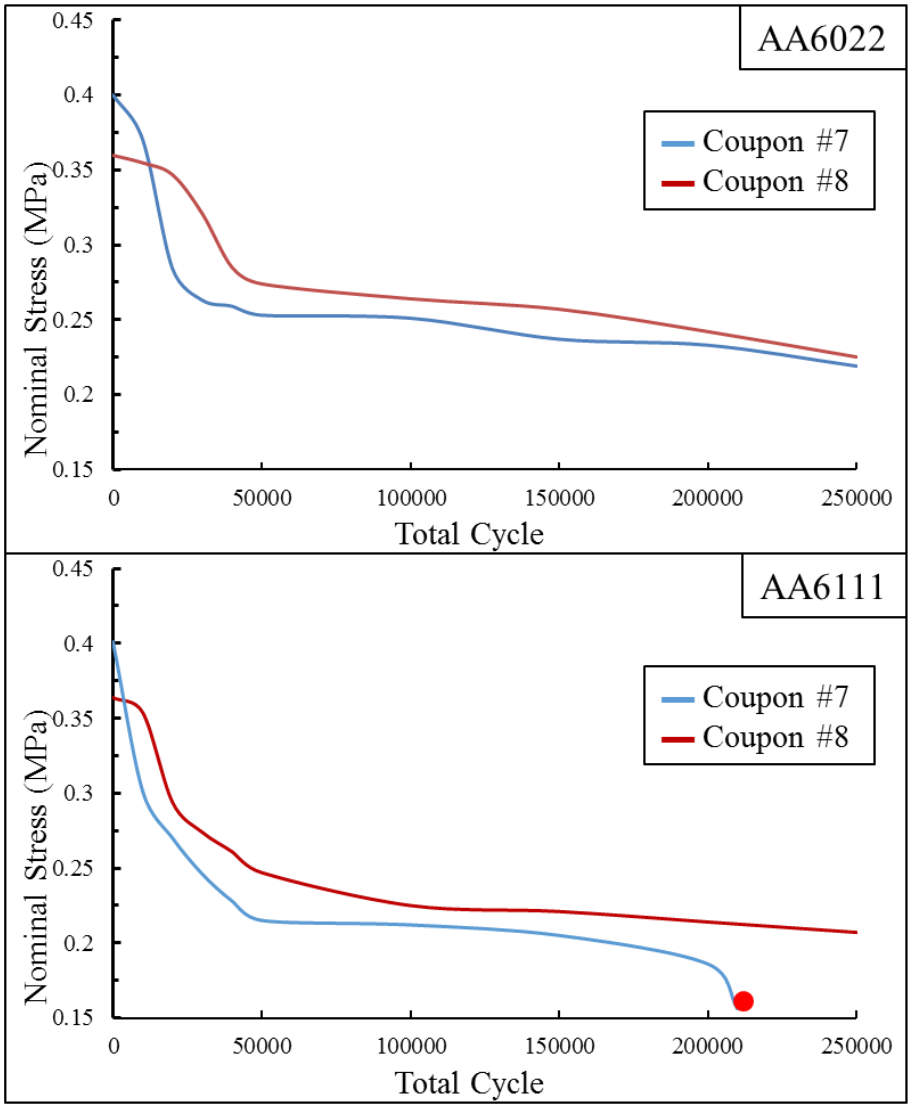

Figure 5.32: Applied nominal stress versus total cycle curves a duplicate set of AA6022 and AA6111 hem flange coupons that were previously corroded (Ford L-3190 for 12 weeks). The red dot indicates the point of fracture.

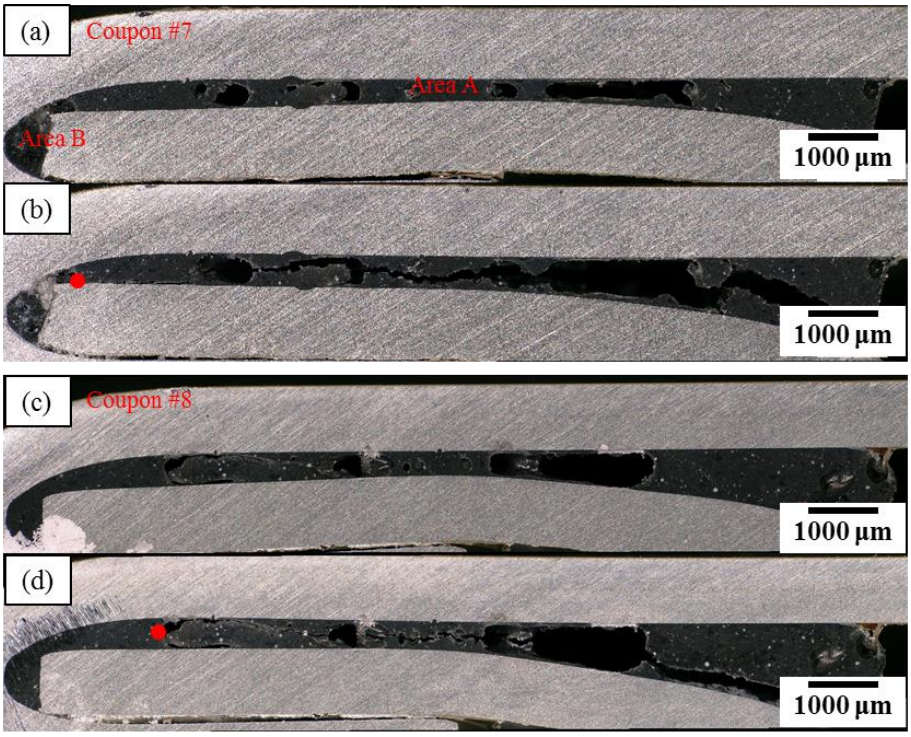

Figure 5.33: Side-view LOM images of the duplicate set of AA6022 coupons that were previously corroded (FORD L-3190 for 12 weeks): coupon #7 after (a) 0 cycles and (b) 100,000 cycles; coupon #8 after (c) 0 cycles and (d) 100,000 cycles. The crack tips are marked by red dots (●).

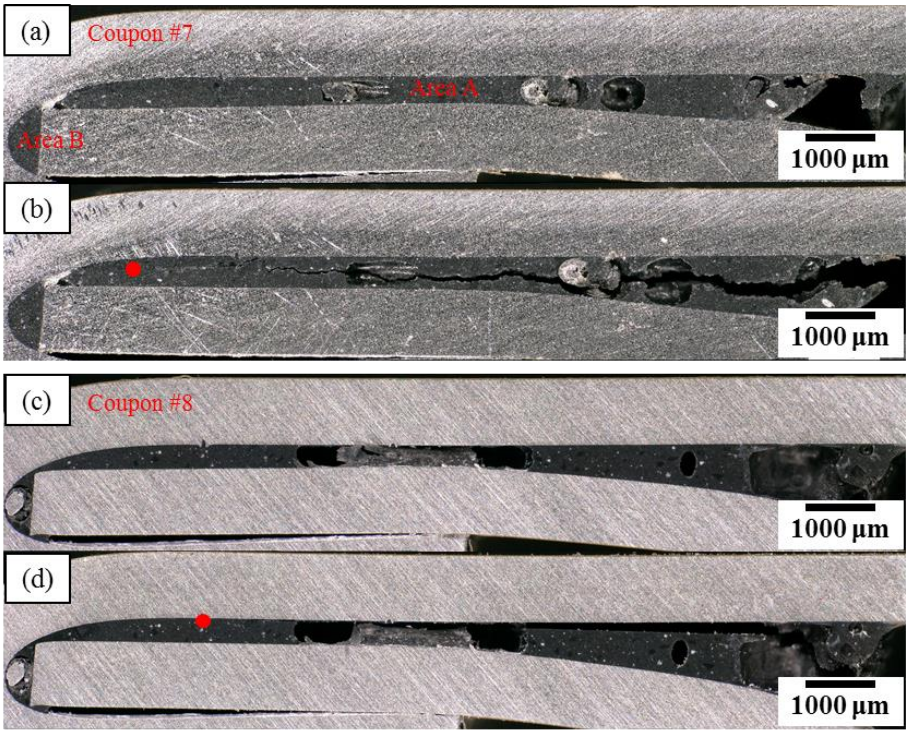

Figure 5.34: Side-view LOM images of the duplicate set of AA6111 coupons that were previously corroded (FORD L-3190 for 12 weeks): coupon #7 after (a) 0 cycles and (b) 100,000 cycles; coupon #8 at (c) 0 cycles and (d) 100,000 cycles. The crack tips are marked by red dots (●).

5.3.2. Effect of Prior Cyclic Deformation Followed by Cyclic Corrosion

The applied nominal stress versus cycle curves (30,000 cycles) for a duplicate set of as-received AA6022 and AA6111 hem flange coupons are shown in Figure 5.35. The corresponding side-view LOM images of the coupons after 0 cycles without cyclic corrosion exposure, 30,000 cycles without cyclic corrosion exposure and 30,000 cycles with subsequent cyclic corrosion exposure (Ford L-3190 for six weeks) are shown in Figure 5.36 (for AA6022) and Figure 5.37 (for AA6111).

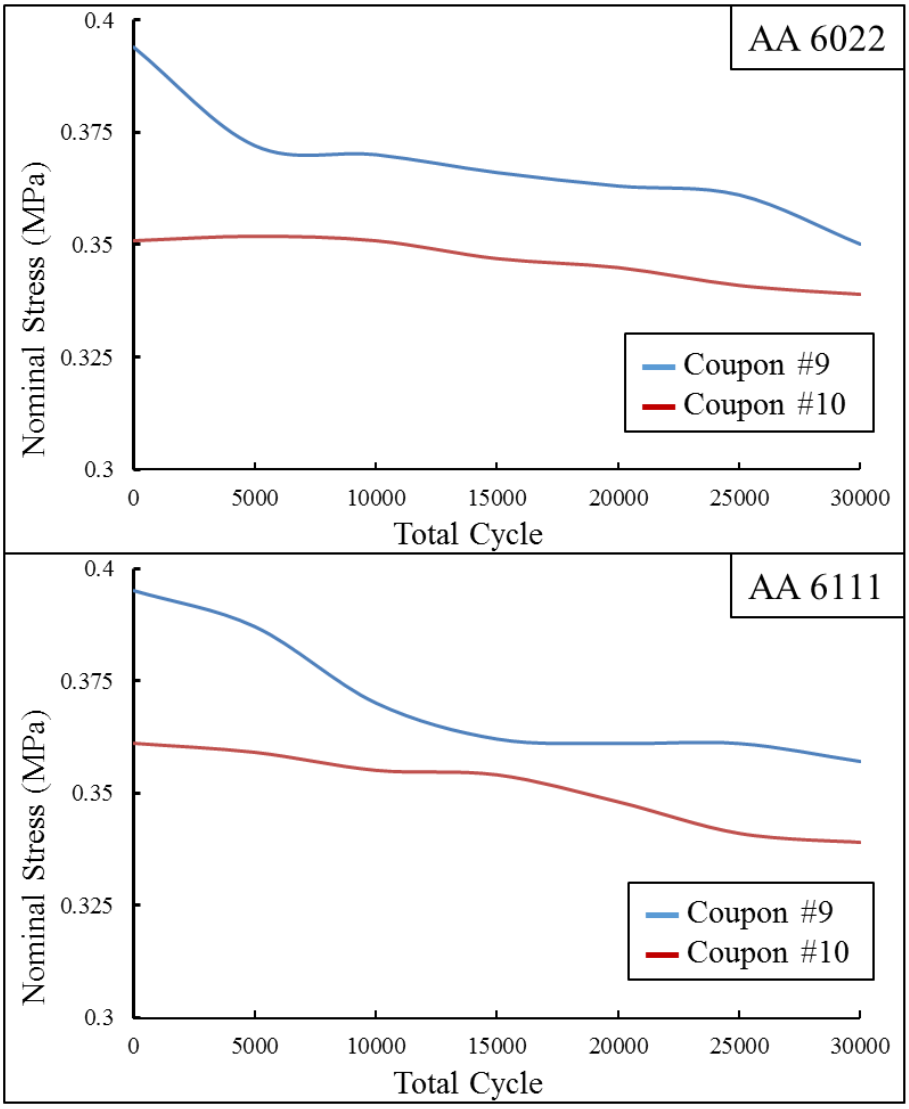

Figure 5.35: Applied nominal stress versus total cycle curves of 30,000 cycles for a duplicate set of as-received AA6022 and AA6111 hem flange coupons.

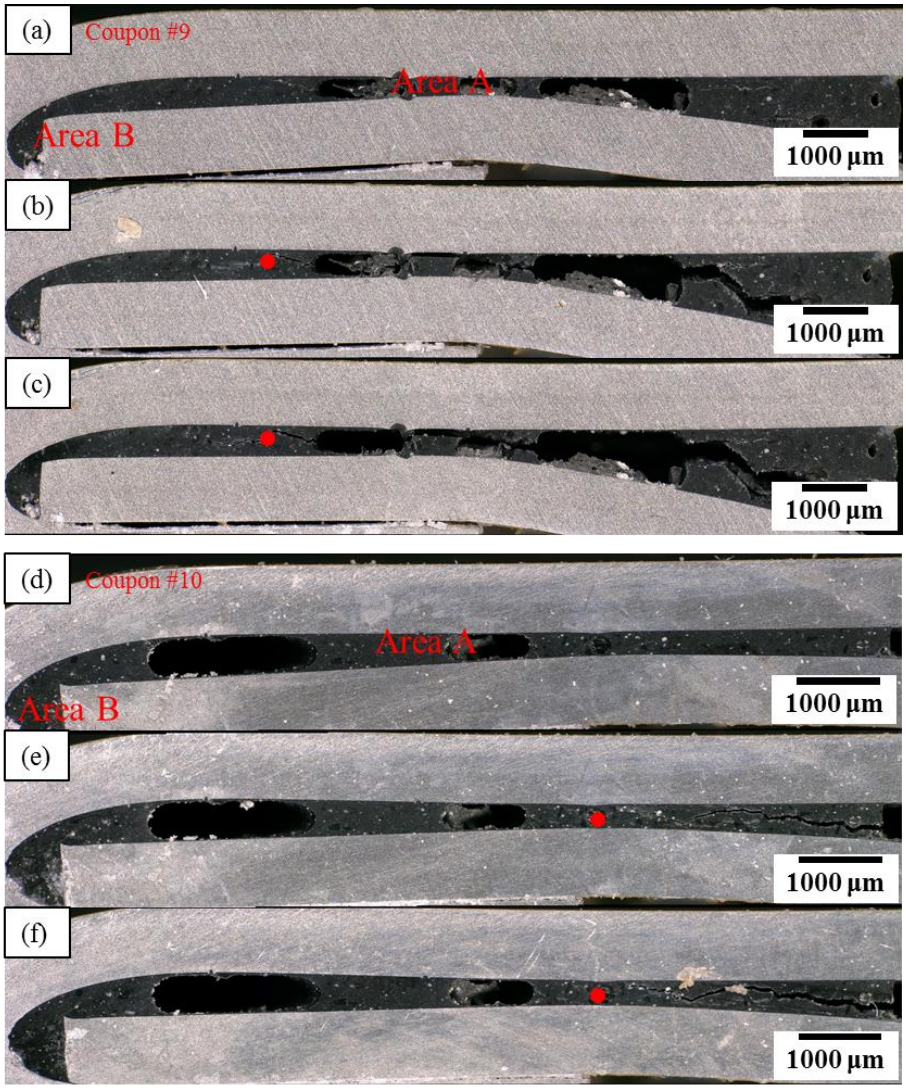

Figure 5.36: Side-view LOM images of the duplicate set of AA6022 coupons: coupon #9 after (a) 0 cycles without cyclic corrosion exposure, (b) 30,000 cycles without cyclic corrosion exposure and (c) 30,000 cycles with subsequent cyclic corrosion exposure (Ford L-3190 for six weeks); coupon #10 after (d) 0 cycles without cyclic corrosion exposure, (e) 30,000 cycles without cyclic corrosion exposure and (f) 30,000 cycles with subsequent cyclic corrosion exposure (Ford L-3190 for 6 weeks). The crack tips are marked by red dots (●).

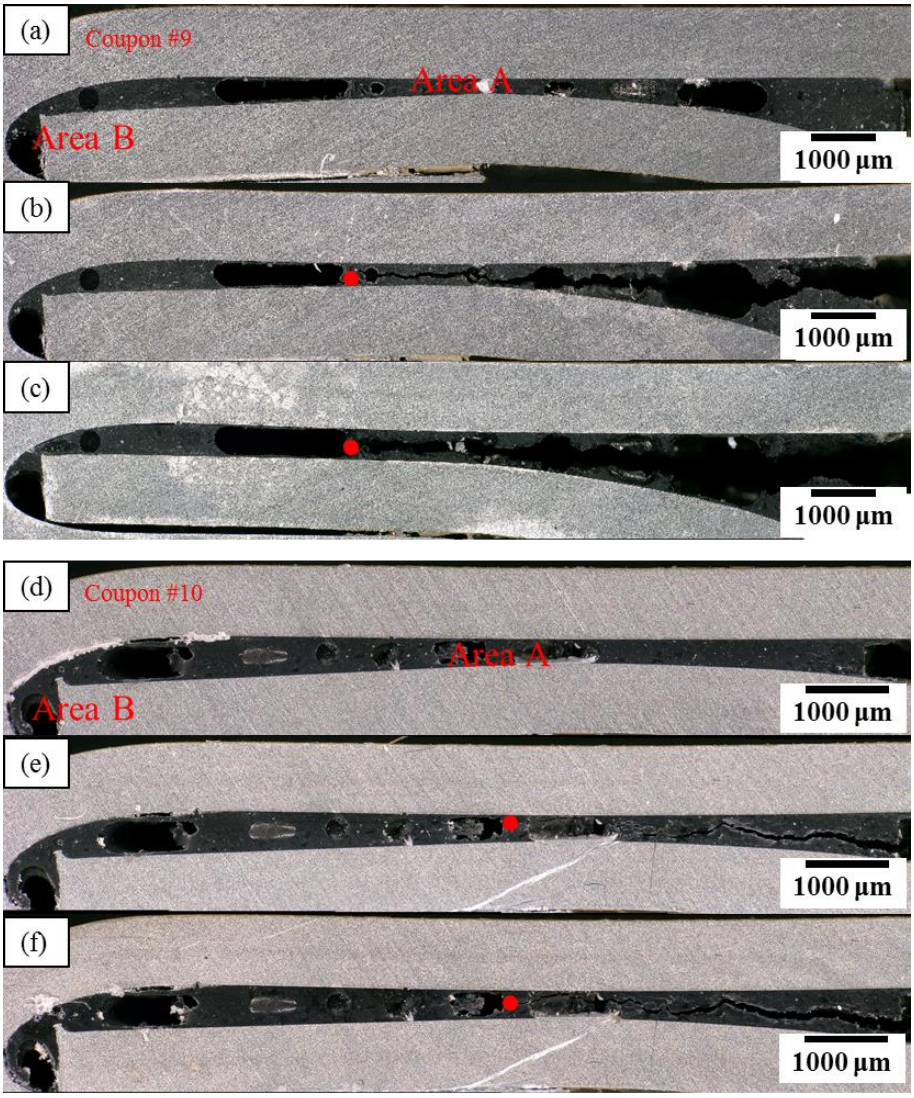

Figure 5.37: Side-view LOM images of the duplicate set of AA6111 coupons: coupon #9 after (a) 0 cycles without cyclic corrosion exposure, (b) 30,000 cycles without cyclic corrosion exposure and (c) 30,000 cycles with subsequent cyclic corrosion exposure (Ford L-3190 for 6 weeks); coupon #10 after (d) 0 cycles without cyclic corrosion exposure, (e) 30,000 cycles without cyclic corrosion exposure and (f) 30,000 cycles with subsequent cyclic corrosion exposure (Ford L-3190 for 6 weeks). The crack tips are marked by red dots (●).

All coupons exhibited adhesive cracking after 30,000 cycles. The crack lengths were not significantly different after the six-week Ford L-3190 exposure for this set of coupons (Figure 5.36 and Figure 5.37), which indicated that the cyclic corrosion did not promote crack growth.

The photograph of these coupons after six weeks of exposure are shown in Figure 5.38. No corrosion damage was observed on the outer surface of both the inner and outer sheets of these coupons.

Polished cross-sectional LOM images revealing the corrosion damage accumulated are shown in Figure 5.39. Only minor pitting damage was observed in area B for both alloys.

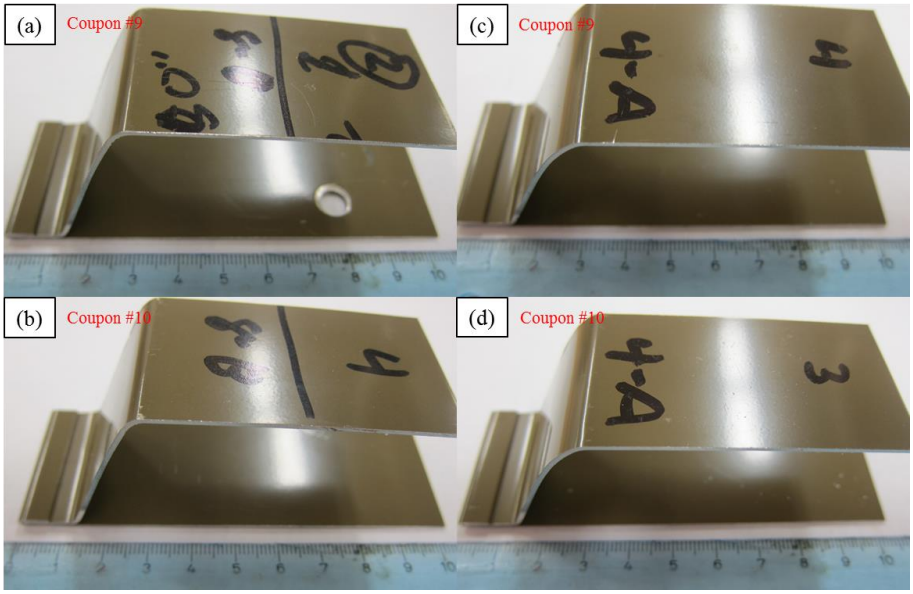

Figure 5.38: Photographs of as-received hem flange coupons (#9 and #10) of (a), (b) AA6022 and (c), (d) AA6111 after six weeks of Ford L-3190 exposure.

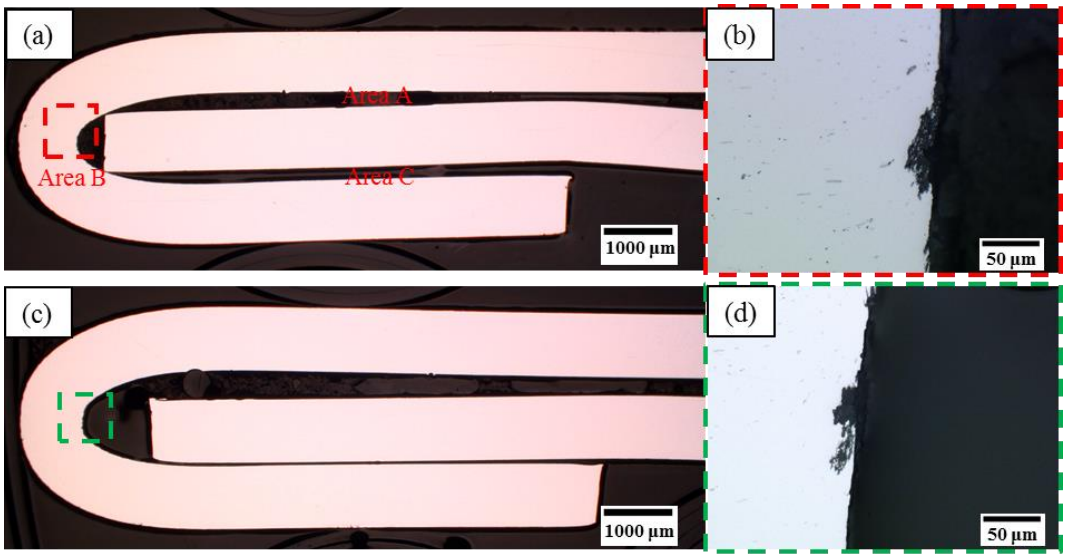

Figure 5.39: Cross-sectional LOM images of coupons after 30,000 cycles of deformation then 6 weeks of Ford L-3190 exposure: (a) AA6022 coupon #9 (b) higher magnification view of red frame, (c) AA6111 coupon #10 and (d) higher magnification view of green frame.

5.3.2.1. Effect of Superimposed Static Stress on Cyclic Corrosion

A static stress was superimposed onto a set of pre-cracked (30,000 cycles) hem flange coupons that were subjected to a six-week FORD L-3190 exposure. The applied nominal stress versus cycle curves to 30,000 cycles for the as-received AA6022 and AA6111 hem flange coupons used for this purpose are shown in Figure 5.40. The corresponding side-view LOM images of each coupon after 0 cycles without cyclic corrosion exposure, 30,000 cycles without cyclic corrosion exposure and 30,000 cycles with subsequent cyclic corrosion exposure (Ford L-3190 for 6 weeks) with a static stress superimposed are shown in Figure 5.41 (for AA6022) and Figure 5.42 (for AA6111).

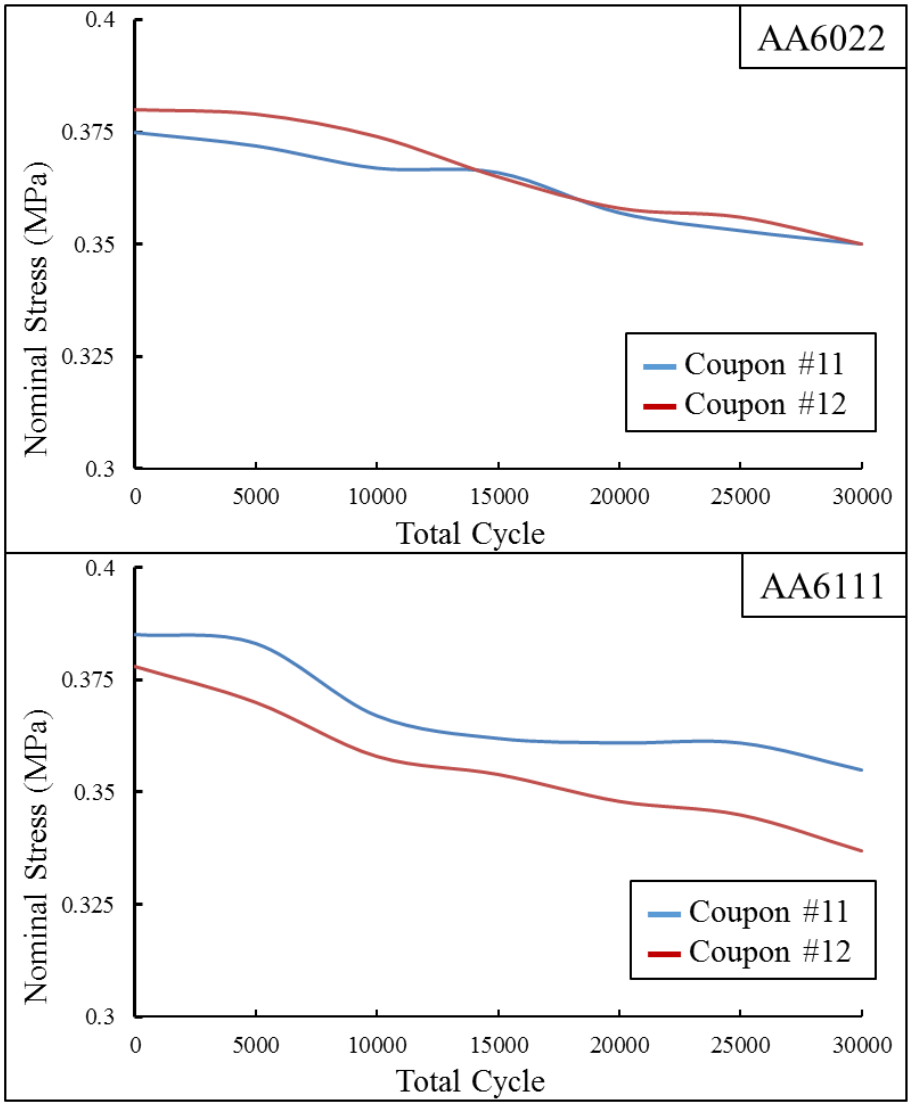

Figure 5.40: Applied nominal stress versus total cycle curves associated with the pre-cracking of a duplicate set of as-received AA6022 and AA6111 hem flange coupons.

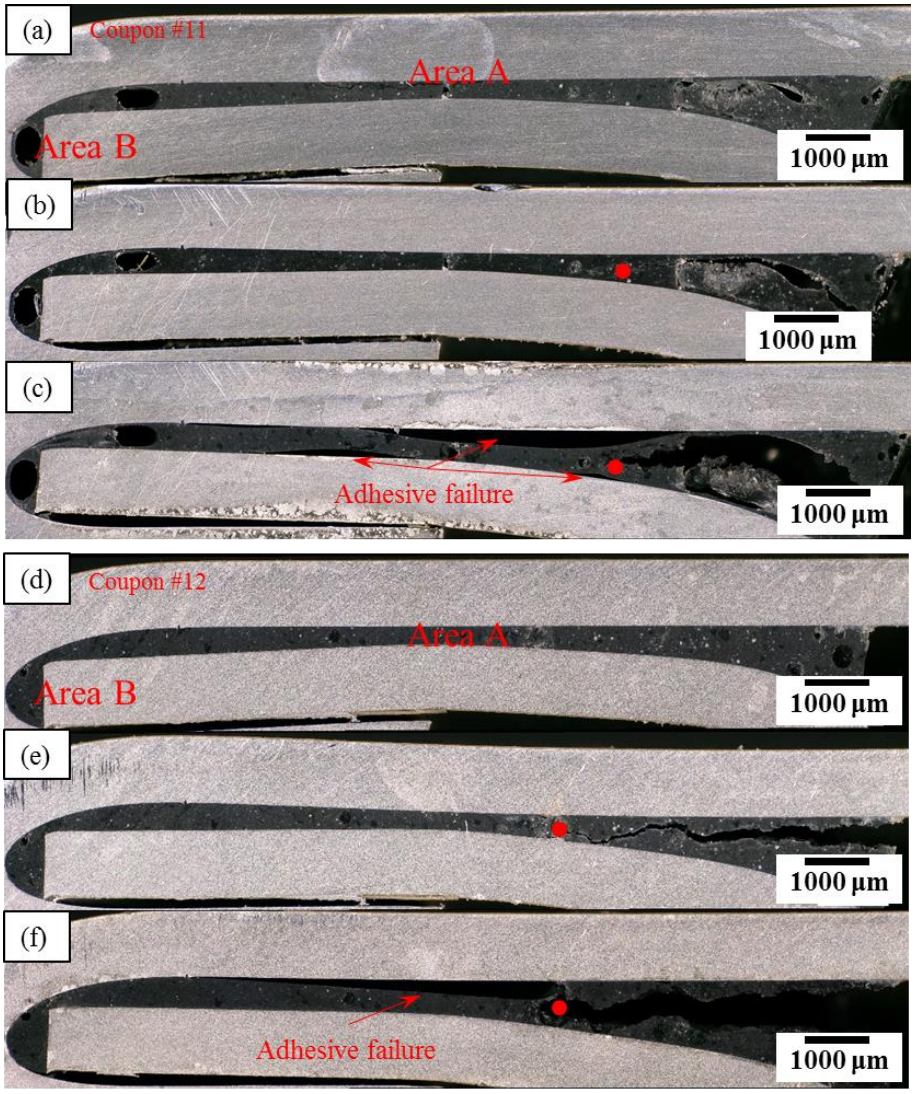

Figure 5.41: Side-view LOM images of the duplicate set of AA6022 coupons: coupon #11 after (a) 0 cycles without cyclic corrosion exposure, (b) 30,000 cycles without cyclic corrosion exposure and (c) 30,000 cycles with subsequent corrosion exposure (Ford L-3190 for 6 weeks) with static stress superimposed; coupon #12 after (d) 0 cycles without cyclic corrosion exposure, (e) 30,000 cycles without cyclic corrosion exposure and (f) 30,000 cycles with subsequent corrosion exposure (Ford L-3190 for 6 weeks) . The crack tips are marked by red dots (●).

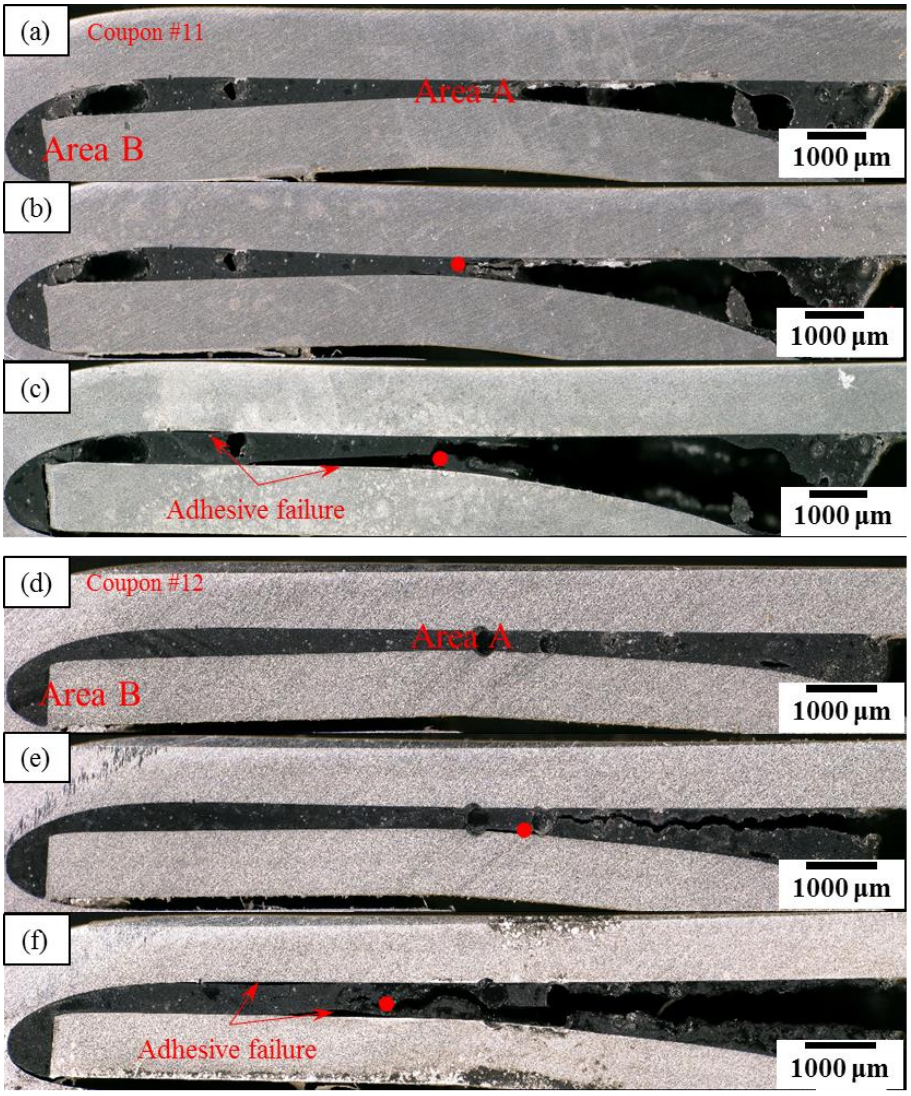

Figure 5.42: Side-view LOM images of the duplicate set of AA6111 coupons: coupon #11 after (a) 0 cycles without cyclic corrosion exposure, (b) 30,000 cycles without cyclic corrosion exposure and (c) 30,000 cycles with subsequent corrosion exposure (Ford L-3190 for 6 weeks) with static stress superimposed; coupon #12 after (d) 0 cycles without cyclic corrosion exposure, (e) 30,000 cycles without cyclic corrosion exposure and (f) 30,000 cycles with subsequent corrosion exposure (Ford L-3190 for 6 weeks) . The crack tips are marked by red dots (●).

All coupons exhibited significant adhesive cracking after 30,000 cycles of deformation (Figure 5.41(b), (e) and Figure 5.42(b), (e)). The adhesive crack length in three of the coupons did not change significantly after the six-week FORD L-3190 exposure: i.e. AA6022 coupon #11, 12, and AA6111 coupon #11. The adhesive crack length in AA6111 coupon #12 increased during the cyclic corrosion exposure. All coupons exhibited a change in the mode of cracking from being within the adhesive itself to the adhesive-metal interface, marked by red arrows in Figure 5.41 and Figure 5.42, after the six-week exposure.

Polished cross-sections revealing accumulated corrosion damage are shown in Figure 5.43. Majority of the corrosion damage was observed in area B for both alloys. Minor corrosion damage was observed in area A after the adhesive delaminated from the base metal (Figure 5.44).

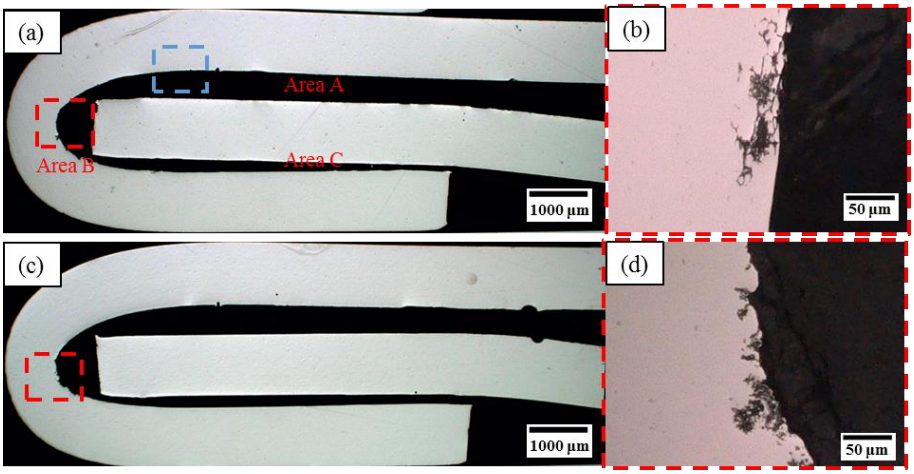

Figure 5.43: Cross-sectional LOM images of coupons after 30,000 cycles of deformation then 6 weeks of Ford L-3190 exposure with static stress superimposed: (a) AA6022 coupon #12 (b) higher magnification view of red frame, (c) AA6111 coupon

#12 and (d) higher magnification view of red frame. The blue frame in (a) is shown in Figure 5.43.

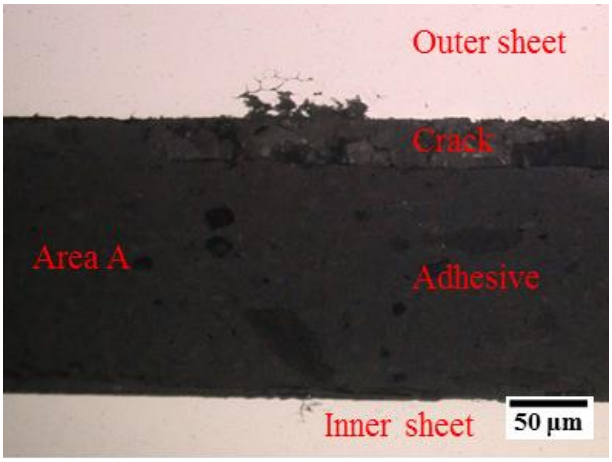

Figure 5.44: High magnification view of Figure 5.43(a) blue frame showing corrosion damage in area A after the adhesive delaminated from outer sheet.

The maximum depth of attack of AA6022 coupon #9, 12 and AA6111 coupon #10, 12 are compared in Figure 5.45. The maximum depth of attack values of regular coupons are also included in this figure as reference. In comparison with the as-received coupons (Figure 5.22), the pre-cracked coupons did not exhibit higher depth of attack (Figure 5.43). The superimposed static stress did not accelerate the corrosion attack in area B, but the delamination of adhesive created new sites for corrosion in area A.

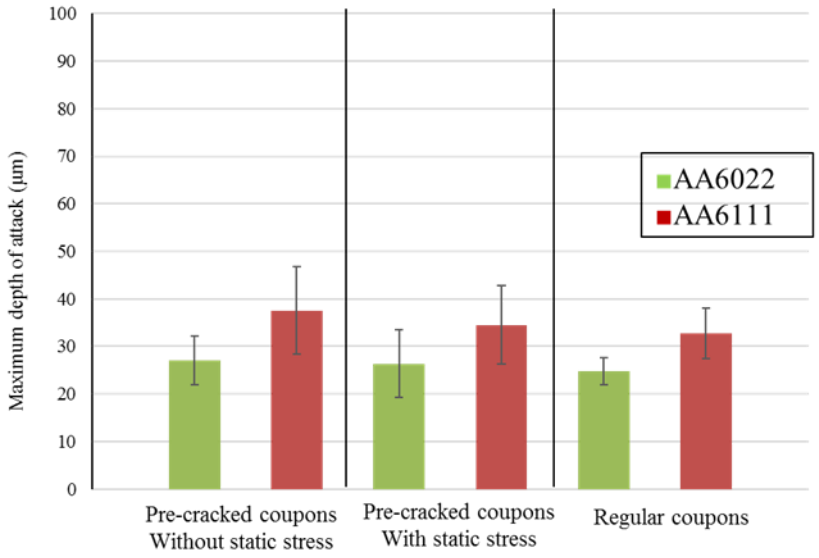

Figure 5.45: Maximum depth of attack in area B of pre-cracked coupons after six-week exposure in Ford L-3190 cyclic corrosion test. Without static stress: AA6022 #9 and AA6111 #10. With static stress superimposed: AA6022 #12 and AA6111 #12. Error bars represent 95% CI.

In order to verify the combined effect of static stress and cyclic corrosion exposure, a duplicate set of pre-cracked coupons (30,000 cycles) of both alloys with static stress superimposed were exposed to laboratory air for six weeks. The side-view LOM images of these control coupons at 0 cycles, 30,000 cycles, and 30,000 cycles with subsequent lab air exposure for six weeks with a static stress superimposed are shown in Figure 5.46. No crack length extension was observed for all experimental coupons, which confirmed that the combined effect of static stress and cyclic corrosion promoted additional failure in the adhesive.

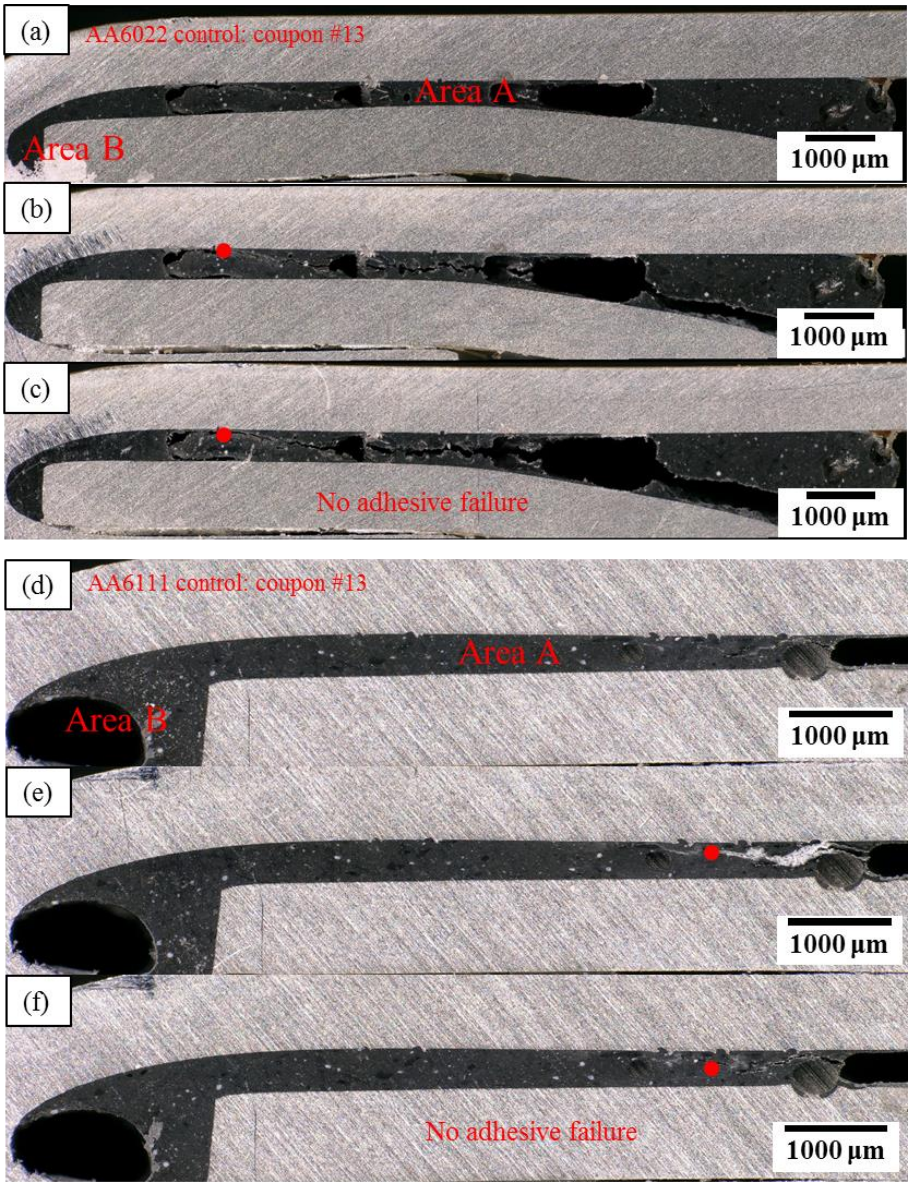

Figure 5.46: Side-view LOM images of duplicate sets of control coupons: AA6022 coupon #13 after (a) 0 cycles, (b) 30,000 cycles, and (c) 30,000 cycles with subsequent lab air exposure for 6 weeks with static stress superimposed; AA6111coupon #13 after (d) 0 cycles, (e) 30,000 cycles, and (f) 30,000 strain cycles with subsequent lab air exposure for 6 weeks with static stress superimposed. The crack tips are marked by red dots (●).

In summary, the damaging effect of cyclic corrosion was presented in Section 5.2.1. . The corrosion damage was restricted in the inner surface of the hem flange coupons (Figure 5.19 and Figure 5.20), whereas no corrosion damage was observed on the outer surface (Figure 5.18). Majority of the corrosion attack was observed in area B, whereas no attack was observed in areas A and C for six-week exposure and minor attack was observed in areas A and C for twelve-week exposure.

The damaging effect of cyclic deformation was presented in Section 5.2.2. . The applied nominal stress decreased gradually with increasing cycle count for the as-received coupons. For all coupons except AA6022 #2, cracks propagated through half of area A after 250,000 cycles.

The damaging effect of cyclic deformation on previously corroded coupons was presented in Section 5.3.1. . Sharp drops in nominal stress were observed for both exposure duration, six and twelve weeks. The sharp drops in nominal stress for the six-week coupons took place approximately at 100,000 cycles (Figure 5.28), whereas for twelve-week coupons before 50,000 cycles (Figure 5.32). For all the previously corroded coupons, cracks fully penetrating area A were observed after 100,000 cycles (Figure 5.29Figure 5.30,Figure 5.33Figure 5.34).

The damaging effect of cyclic corrosion on pre-cracked coupons was presented in Section 5.3.2. . After six-week exposure, the pre-cracked coupons had corrosion damage comparable to that of the as-received coupons (Figure 5.45). The cyclic corrosion did not increase the length of the cracks in all coupons (Figure 5.36 and Figure 5.37). The extension of cracks was observed only when corrosive environment and superimposed static stress

were both present (Figure 5.41 and Figure 5.42). When static stress was present, the cracking in adhesive changed from the bulk of adhesive to the adhesive-metal interface.

Chapter 6: Discussion

6.1. Effect of Cyclic Corrosion

The extent of corrosion attack of the three areas, A, B, and C, within a hem flange coupon were drastically different. For both exposure durations, six-week and twelve-week, area B was found to be the most susceptible to corrosion (Figure 5.19 and Figure 5.20). A schematic to account for the enhanced corrosion observed in area B relative to areas A and C is illustrated in Figure 6.1.

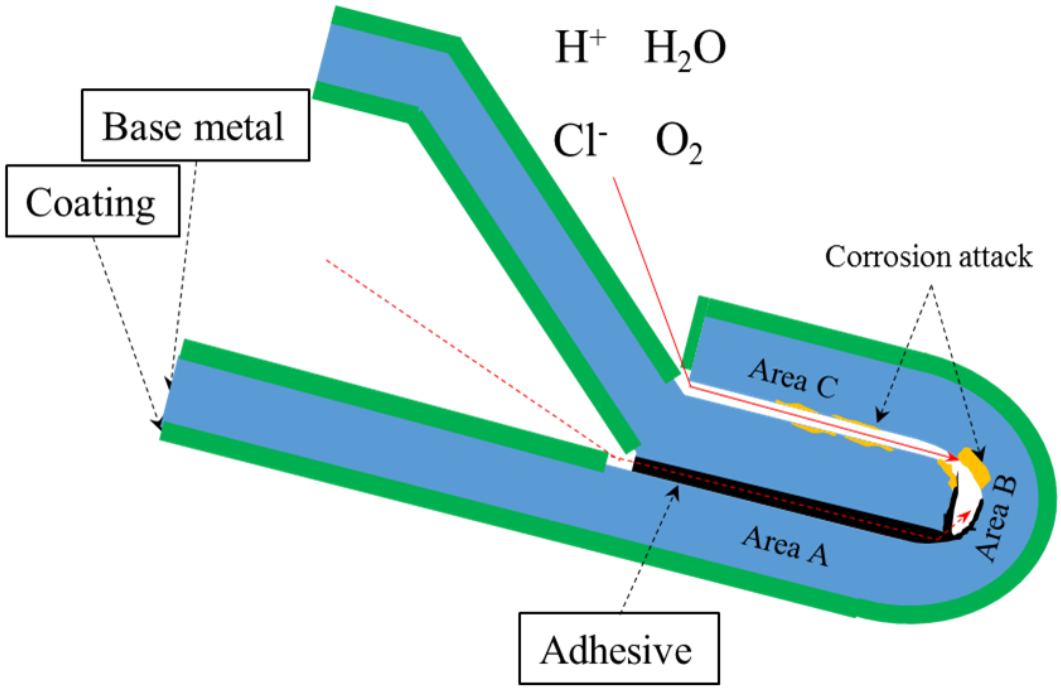

Figure 6.1: Schematic of the corrosion damage accumulated within the hem flange joint. The coupon is slightly tilted to reflect the sample geometry during the cyclic corrosion exposure.

The corrosive salt solution was capable of reaching area B via two pathways. The first pathway, marked by the dashed red arrow in Figure 6.1, was the interconnected pores in the adhesive layer in area A. This pathway was established in the case of the as-received coupons in Figure 5.10 and Figure 5.11 using NR combined with $Gd(NO_3)_3$ solution of the eight randomly selected as-received hem flange coupons subjected to the NR + $Gd(NO_3)_3$ solution examination (four for each alloy), only four had fully connected pores from area A to area B. For this reason, this pathway only sporadically existed and did not necessarily contribute to the corrosion of area B in every as-received coupon. Moreover, X-ray CT scans, as shown in Figure 5.14, revealed that most of the pores were isolated from the Al alloy substrate in the as-received coupons by a thin layer of adhesive, which protected the Al alloy substrate in area A from corrosion. When this pathway was closed, the Al alloy substrate in area A was also protected from corrosion. In either case, the adhesive served as a barrier between the Al alloy substrate and corrosive salt solution in the as-received coupons, which explains why area A was observed to have the least amount of corrosion damage.

The second pathway, marked by the red arrow in Figure 6.1, was the crevice between the inner sheet and the outer sheet in area C, which had no adhesive coverage. This pathway contributed to the corrosion of area B due to its existence for all coupons under all of the exposure conditions explored in this study. Since the Al alloy substrate in area C was neither covered by coating nor by adhesive, corrosion took place when the corrosive salt solution past through due to capillary flow into and through area C to area B, where the

feeding of solution into area C may have been aided by the slight tilting of the hem flange coupons during the cyclic corrosion exposure

Area B was also more susceptible to corrosion than area A or area C, due to the high degree of plastic deformation and micro-cracking present in the inner radius in this zone. Literature has shown that plastic deformation adversely affects the resistance of Al alloys to pitting corrosion and IGC [21, 74]. Furthermore, the pre-existing micro-cracks weakened the integrity of the passive film and could serve as initiation sites for localized corrosion to take place [20, 21]. In order to verify the adverse effect of plastic deformation on the localized corrosion resistance, potentiodynamic polarization tests were done on the outer tensile surface of the outer sheet of uncoated hem flange coupons. The inner compressive surface, the actual area B, was not tested due to it being a concave surface, which is very difficult to extract, and covered with adhesive. A direct comparison between the potentiodynamic polarization curves of the un-deformed surface and the outer tensile surface is shown in Figure 6.2. It shows that the outer tensile surface had a lower E_b, and higher i_{corr}, than that of the un-deformed surface. This indicates that corrosion initiation was easier and the corrosion rate higher in the plastically deformed area B than in the un-deformed areas A and C. Thus, combining the effect of plastic deformation, micro-cracking, and capillary flow due to coupon orientation, area B was more susceptible to corrosion than area A and C. The effect of gravity all ensured that there was a continuous supply of electrolyte into area B.

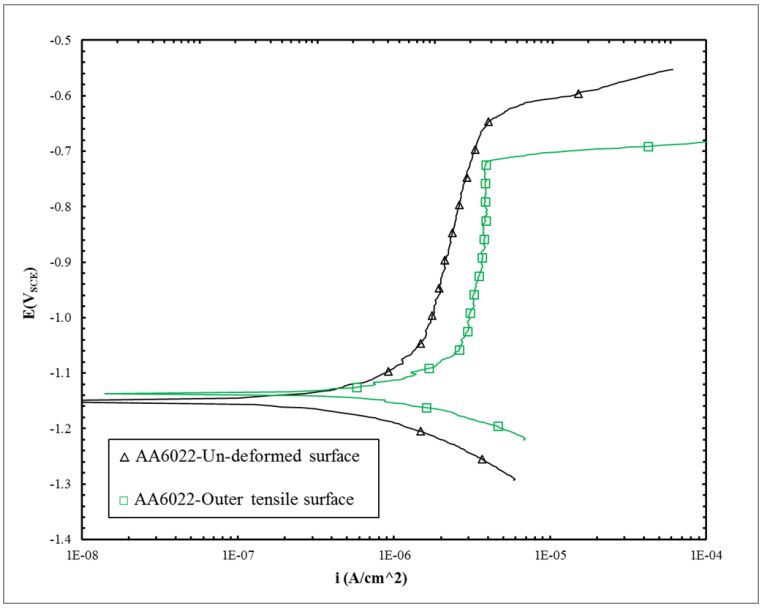

Figure 6.2: Typical potentiodynamic polarization curves for the un-deformed surface and the outer tensile surface of AA6022 hem flange coupon in 0.1 M deaerated neutral NaCl solution.

For both alloys, pitting corrosion was observed after six weeks of exposure, whereas pitting corrosion and IGC were observed after twelve weeks of exposure. The extent of the IGC was more pronounced in AA6111 than in AA6022 coupons. The SEM-EDS data (Figure 5.8 and Figure 5.9) indicated that the intermetallic particles of both AA6022 and AA6111 were Cu enriched. Furthermore, the matrix of AA6111 had a higher amount of Cu than that of AA6022, which led to the enhancement of anodic current as well as the increase of localized corrosion susceptibility. This observation is consistent with the literature, which reported the formation of micro-galvanic cells that formed between the cathodic Cu-bearing phases and the anodic surrounding Al matrix [28, 41].

The maximum depth of attack observed after the twelve-week exposure was three times larger than that observed after the six-week exposure for AA6022 and 2.7 times larger than that observed AA6111 (Figure 5.22). The majority of corrosion is assumed to have occurred during the daily wet-dry transition. During the wet phase, the salt solution would have flowed into and accumulated in area B. During the dry phase, the salt solution would have evaporated due to the relatively high temperature, leaving the solute and acid as remnants in area B. This would have allowed the salt solution to be progressively more aggressive during future cycles, which in turn would accelerate attack. Such a mechanism has been shown to be the case in cyclic corrosion testing of Al alloys [75].

The twelve-week exposure was not sufficient for the corrosion to penetrate the full thickness of the coupons. No corrosion damage was observed on the outer surface of the hem flange coupons.

6.2. Effect of Cyclic Deformation

Due to the large variation of coupon ACF in this work, established by NR, the term "nominal stress" was introduced in Equation (5.2) and (5.3) as a means of normalizing the load reading, collected during cyclic deformation tests, by the ACF value of each individual coupon. The nominal stress values were used to represent the stress applied to the adhesive layer, assuming the area of the adhesive layer did not change during the cyclic deformation test even when cracking took place. For this reason, the nominal stress is often referred to as the "applied nominal stress" in this work. Furthermore, the nominal stress values of a

particular coupon did not correlate to the strength of such coupon, instead, the loss of nominal stress signified the loss of load bearing ability of the coupon.

A correlation between the ACF and the initial applied nominal stress of the hem flange coupon seemed apparent. For example, the highest initial stress of 0.37 MPa was observed for the AA6022 coupon #2, which had an ACF value of 0.42. The lowest initial stress of 0.30 MPa was observed for AA6111 coupon #3, which had an ACF value of 0.63. This apparent correlation was explored in some detail by plotting the initial nominal stress versus the ACF, as shown in Figure 6.3. The coefficient of determination (R^2) is 0.9193. It is difficult to conclude that ACF had a linear correlation with the initial applied nominal stress solely based on this figure. However, a general trend of high ACF associating with low nominal stress can be observed. This indicates that, in the cyclic deformation test, the load applied onto the different hem flange coupons due to displacement was comparable to each other and lower ACF caused higher stress experienced by the adhesive layer.

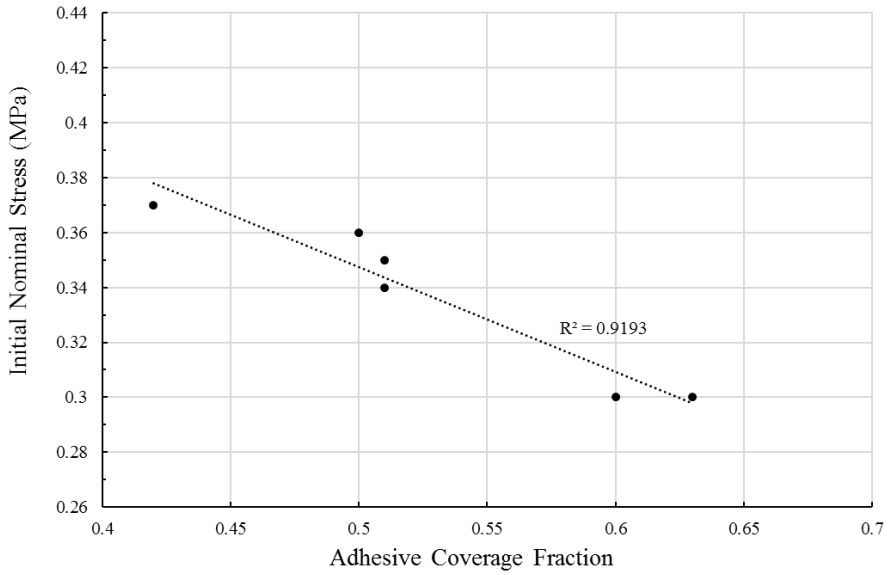

Figure 6.3: Initial nominal stress (MPa) vs. ACF plot of as-received hem flange coupons. Dashed line represents the trend line.

During cyclic deformation tests, as the cycle count increased, cracking events in area A started to take place. For this reason, it was important to define a metric to quantify the damage accumulated in area A. The side-view images showing the location of the crack tip in Chapter 5 provide a qualitative assessment on the approximate cracking status of a particular coupon. However, these side-view images provide little information regarding the remaining load bearing ability of a particular coupon at the cycle count where the side-view image was taken, since the side-view images only show the apparent cracking on one cross-section and were likely not representative of the entirety of the particular hem flange coupon. In addition, the crack propagation behaviour as the cycles increased was not able to be tracked by the side-view images, since multiple interruptions of the cyclic deformation test would have introduced numerous discontinuities on the nominal stress vs. total

cycle curve. For these reasons, the side-view images did not serve as a good metric to determine the damage accumulated in area A due to cyclic deformation.

Based on the previously presented nominal stress vs. total cycle curves, in conjunction with the previously presented side-view images, a qualitative metric to assess the extent of cracking in the adhesive layer for all tested coupons due to cyclic deformation based on retained nominal stress is summarized in Table 6.1. The extend of cracking was only determined approximately by examining the corresponding side-view images.

Table 6.1: Stages of retained nominal stress and corresponding extend of cracking of tested hem flange coupons.

Coupon status	Area A status	Retained nominal stress range
Intact coupon	No cracking	0.34 ~ 0.39 MPa
Compromised coupon	Minor cracking (less than 50% of area A)	0.29 ~ 0.34 MPa
Cracked coupon	Severe cracking (above 80% of area A)	0.20 ~ 0.25 MPa
Loose coupon	Full cracking (separation between inner sheet and outer sheet)	Below 0.15 MPa

For the as-received coupons, 250,000 deformation cycles typically yielded a compromised coupon, which had approximate retained nominal stress of 0.30 MPa, except in

the case of AA6022 #2 (Figure 5.24), which had its nominal stress dropped below 0.2 MPa after 250,000 cycles. The gradual drop of nominal stress observed in the as-received coupons is indicative of a slow loss of load bearing ability due to crack propagation. All of the cracks in area A of the as-received coupons had a zigzag pattern, indicating cohesive failure.

6.3. Effect of Cyclic Corrosion followed by Cyclic Deformation

6.3.1. Six-week Exposure

In comparison with the cyclic deformation of the as-received coupons, the coupons with six weeks of cyclic corrosion pre-exposure had similar initial cyclic deformation response: i.e. the initial nominal stress ranged from 0.35 MPa to 0.40 MPa (Figure 5.28). Unlike the as-received coupons, all of the six-week pre-exposed coupons had a significant drop in nominal stress before 100,000 cycles. After 100,000 cycles, the nominal stress of these coupons dropped to 0.23 ~ 0.26 MPa. Side-view images (Figure 5.29 and Figure 5.30) taken at 100,000 cycles revealed that area A of these coupons was almost fully-cracked. The side-view image observations were consistent with the nominal stress readings, indicating that the six-week pre-exposed coupons all had severe cracking area A, consistent with the qualitative criteria listed in Table 6.1, by 100,000 cycles. The sharp nominal stress drops before 100,000 cycles can be linked to the rapid propagation of cracks in area A. The cracks propagated through the bulk of the adhesive layer for all of the six-week pre-exposed coupons, indicating cohesive failure.

Between 100,000 ~ 250,000 cycles, the nominal stress of all coupons reached a relatively stable plateau. This stabilization of nominal stress can be attributed to the lack of load bearing ability in the hem flange coupons. The cyclic corrosion exposure resulted in the embrittlement of the adhesive layer. The initiation of cracks took place at a lower total cycle; and the subsequent propagation of cracks required less cycle to complete compared to the as-received coupons. When the cracks penetrated through most of area A, the outer and inner sheet of the hem flange coupon were allowed more movement relative to each other when subjected to displacement controlled cyclic deformation. For this reason, less nominal stress was experienced by the adhesive layer and causing the eventual plateau of nominal stress response.

A stepwise drop of nominal stress was observed on AA6022 coupon #4 and AA6111 coupon #6 (Figure 5.28). The stepwise drop of stress was not previously observed in the cyclic deformation of the as-received coupons, and can potentially be explained by the distribution of pores in the adhesive of these two coupons, as shown in Figure 6.4. In both coupons, the adhesive had three different “bands”. The first and third band had almost no pores in them (high ACF), whereas the second band had large amount of pores in it (low ACF). The first drop of nominal stress took place before 50,000 cycles for both of the coupons, which can be attributed to the cracking of the first band (high ACF). Similarly, the second drop, which took place around 100,000 cycles for AA6022 #4 and around 75,000 cycles for AA6111 #6, can be attributed to the cracking of the high ACF band near area B, or the third band counting from top of the figure. After the nominal stress response reached

a plateau after 100,000 cycles, the area A of both coupons were nearly fully cracked, as shown in Figure 5.29 (b) and Figure 5.30 (f).

This stepwise drop of nominal stress associated with the band-like distribution of pores in the adhesive was not reproduced likely due to the large variations in the ACF as well as the pore distribution among other coupons.

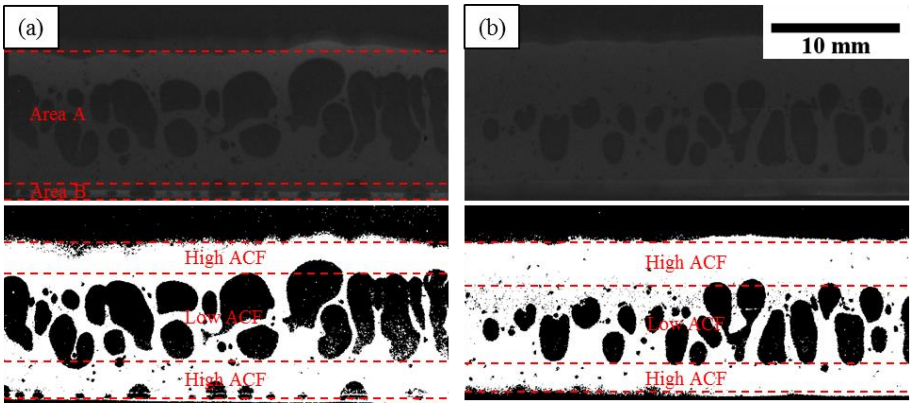

Figure 6.4: Neutron radiograph image and corresponding image after thresholding of (a) AA 6022 coupon #4 and (b) AA 6111 coupon #6.

6.3.2. Twelve-week Exposure

In comparison with the coupons exposed for six weeks, the coupons pre-exposed for twelve weeks had a similar initial nominal stress response i.e. 0.35 ~ 0.40 MPa (Figure 5.32). However, all of the twelve-week pre-exposed coupons had steep drop in nominal stress before 50,000 cycles. After 50,000 cycles, the nominal stress of the twelve-week coupons dropped to 0.23 ~ 0.27 MPa. Side-view images (Figure 5.33 and Figure 5.34) taken at 100,000 cycles revealed that the area A of these coupons were almost fully cracked. The side-view image observations were consistent with the nominal stress readings, indicating

that the six-week pre-exposed coupons all had severe cracking, consistent with the criteria outlined Table 6.1, in area A by 50,000 cycles. Similar to the six-week pre-exposed coupons, the nominal stress of the twelve-week pre-exposed coupons reached a plateau after a significant drop, which can be explained by the same reason stated for the six-week pre-exposed coupons.

As mentioned previously, the sharp drop of nominal stress was likely related to the initiation and subsequent propagation of cracks. Thus, the first sharp drop of nominal stress was likely related to the initiation of cracks. A plot of cycle to first stress drop vs. ACF is shown in Figure 6.5. The coefficient of determination (R^2) is 0.5871 for the coupons with six-week exposure and 0.8601 for the twelve-week exposure. The correlation between the cycle to first stress drop and ACF is not suggested by this plot due to the lack of linearity.

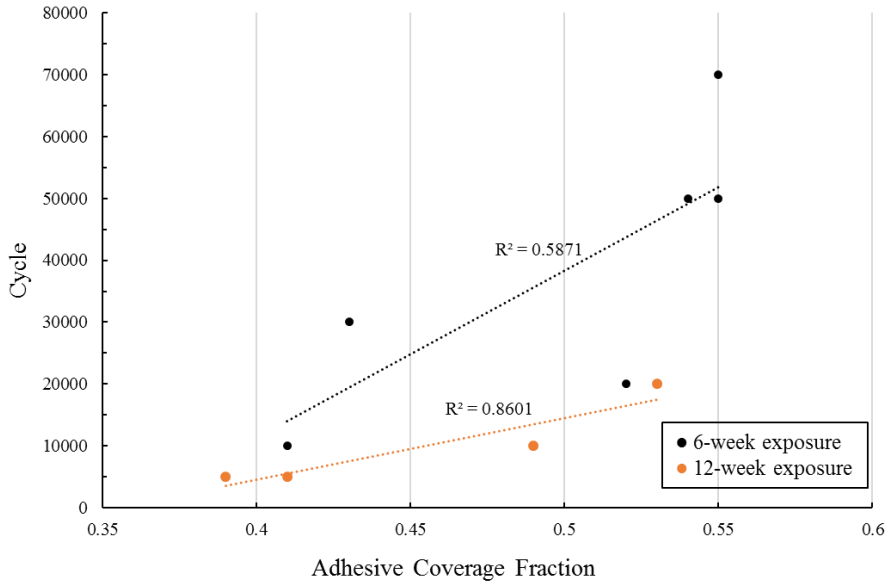

Figure 6.5: Cycles to first nominal stress drop vs. ACF plots of previously corroded coupons. Dashed lines represent the trend lines.

For the six-week pre-exposed coupons, the step-wise drop of nominal stress significantly influenced the linearity of this fit. For the twelve-week cases, all stress drops started before 20,000 cycles and were completed before 50,000 cycles. Despite the linearity of the twelve-week exposure data is higher than that of the six-week data, no correlation can be concluded. Since after twelve-week exposure, the adhesive was severely embrittled, which could diminish any potential effect of high ACF.

In summary, the damaging effect of prior cyclic corrosion on the cyclic deformation response was primarily manifested on the load bearing ability of the adhesive layer. For the as-received coupons, the nominal stress response, which was indicative of the load bearing ability of the adhesive, gradually decreased as the cycle increased. For the cyclically corroded coupons, the nominal stress response had sharp drops, which were not found in the as-received coupons. The sharp drops in stress response indicated the initiation and subsequent propagation of cracks in the adhesive layer. The longer duration of exposure further decreased the load bearing ability of adhesive. The prior cyclic corrosion exposure did not change the mode of failure. All of the cracks in the six-week and twelve-week coupons were “zigzag” shaped, indicating cohesive failure. This was expected considering the literature on the environmental failure of adhesive joints which reported that adhesive undergoes swelling and plasticization in corrosive environment and gradually embrittles as exposure time increases [58, 59, 60].

6.4. Effect of Cyclic Deformation followed by Cyclic Corrosion

Cracking of the adhesive layer occurred after 30,000 cycles for the as-received coupons. All of the coupons retained a significant portion of the initial nominal stress after 30,000 cycles (0.34 ~ 0.37 MPa), as shown in Figure 5.35. Based on the metrics defined in Table 6.1, all of these coupons only had minor cracking in area A. The pre-cracking of the adhesive layer could potentially activate the pathway within area A for the corrosive solution to enter the hem flange coupon, if the crack front reached a pore network that connects to area B. However, this potential pathway did not increase the corrosion susceptibility of the three areas of interest (A, B and C). As shown in Figure 5.39, no corrosion damage was observed in area A of the pre-cracked coupons after six weeks of exposure. The primary corrosion damage was found in area B, similar to the coupons without pre-cracking. A comparison of the maximum depth of attack between area B of as-received and coupons pre-cracked and then exposed is shown in Figure 5.45, which showed no statistical difference between the two cases. Thus, it can be said that the cyclic corrosion exposure did not induce additional cracking in the adhesive.

Based on the observation made above, the pre-cracking of adhesive did not contribute to the corrosion of areas A, B, and C. In the corrosion of the hem flange coupon, the pathway through area C was the dominating factor, since the pathway through area C was always open, and therefore was able to transport the greatest amount of solution into area B. The pathway through area A was only situational that required either an interconnected

pore network or a cracking event that fully penetrated area A. For this reason, at six-week exposure duration, the pre-cracked coupons did not exhibit higher corrosion susceptibility in area B compared to the as-received coupons. However, it is possible that the pre-cracking of area A will eventually come to effect at longer exposure durations. Since the activation of pathway through area A will lead to a larger amount of electrolyte being transported into area B. In addition, the corrosion damage was more pronounced at longer exposure duration, in which IGC took place. For this reason, the effect of pre-cracking in area A can be magnified and possibly observable at longer exposure durations.

6.4.1. Effect of Static Stress

When static stress was superimposed onto the pre-cracked coupons during cyclic corrosion exposure, clean cleavages at the adhesive-metal interface were observed in all coupons. The cleavage between the adhesive and metal substrate was indicative of adhesive failure (Figure 5.41 and Figure 5.42), which was not previously observed in any testing condition. In this test, the magnitude of the static nominal stress created by the plastic bolts was presumably comparable to the nominal stress experienced by the coupons at +2 mm position during cyclic deformation, which was around 0.34 ~ 0.36 MPa. However, the static stress, in combination with the corrosive environment, severely reduced the bonding strength between the adhesive and metal substrate, which enabled adhesive failure along the interface, whereas cyclic deformation along did not produce this effect. In addition, the cohesive crack did not propagate in three of the four coupons, except AA6111 #12 (Figure 5.42 (f)), which indicated that the propagation of cohesive cracks was predominately due to cyclic

stress, whereas static stress primarily contributed to cleavage along the interface. The pre-cracked coupons in the control group (exposure to lab air for 6 weeks) did not have any crack propagation. The lack of crack propagation in this case indicated that the static stress and the cyclic corrosive exposure had a synergic effect---the lack of either one will not induce further cracking. This suggests that the removal of either corrosive environment or static stress will effectively reduce the likelihood of adhesive failure.

The maximum depth of attack in area B of the pre-cracked coupons after six-week exposure with static stress superimposed is shown in Figure 5.45. Compared with the scenario without static stress and without pre-cracking, the coupons with static stress superimposed did not exhibit a higher susceptibility to corrosion attack in area B. Due to the delamination between the adhesive layer and the base metal, minor pitting damage was observed in a new site that was previously covered by adhesive in area A, as shown in Figure 5.44. This observation indicates that static stress can activate new pathways of ingress that were previously covered by adhesive.

Chapter 7: Conclusions and Recommendations

In this work, coated AA6022 and AA6111 hem flange coupons were characterized using microscopic, radiographic, and electrochemical techniques. Two possible sources of damage, cyclic corrosion and cyclic deformation, for the hem flange coupons were first investigated in isolation from each other, and then investigated in series, which included the cyclic deformation of previously corroded coupons and cyclic corrosion of pre-cracked coupons. The key findings of this work are listed below:

1) Neutron radiography and X-ray computed tomography were successfully employed to characterize the adhesive layer coverage fraction and the distribution of the pores in the adhesive layer.
2) The connectivity of pores was investigated using gadolinium(III) nitrate ($Gd(NO_3)_3$) solution, which is a novel methodology that was not previously reported. Half of the hem flange coupons were found to have fully interconnected network of pores from area A to area B.
3) The cyclic corrosion exposure revealed that area B was the weak link in the corrosion resistance of hem flange joints. The sample orientation during corrosion exposure facilitated the accumulation of electrolyte in area B. The base metal in area B was also more susceptible to localized corrosion than areas A and C due to the presence of a high degree of plastic deformation and micro-cracking. AA6111 (Cu-rich) was observed to be more susceptible to corrosion attack than AA6022 (Cu-lean), which was consistent with the literature [28, 41].

4) The occurrence of corrosion in area B of coupons that had no cyclic deformation damage in the adhesive layer depended on two independent pathways: pathway A through the adhesive layer in area A, and pathway C through the open crevice in area C. Pathway A was opened when an interconnecting pore network was present. Pathway C was always open due to the presence of the open crevice.
5) Cyclic deformation served to initiate and propagate cracking in the adhesive layer by a cohesive failure mode. Cracking due to cyclic deformation was not necessary to activate pathway A if an interconnecting pore network was present. Cracking due to cyclic deformation did not create new regions in area A that were not covered by adhesive, since crack propagation took place in the bulk of the adhesive rather than at the metal-adhesive interface.
6) The cyclic deformation of previously corroded coupons revealed that cyclic corrosion severely reduced the load bearing ability of the adhesive layer, resulting in a fast initiation and propagation of cracks, as indicative by the sharp drop in the nominal stress. An increase in prior cyclic corrosion exposure time further reduced the load bearing ability.
7) The cyclic corrosion response of pre-cracked coupons suggested that pre-existing cracks do not increase the corrosion susceptibility of hem flange coupons for the six-week exposure duration. Since cracking due to cyclic deformation in area A only served to activate pathway A, pathway C was independent of this process. For this reason, pathway C was the dominant factor that controlled the corrosion behaviour.

It is possible that the pre-cracking of area A will influence the corrosion behaviour at longer exposure durations.

8) The cyclic corrosion response of pre-cracked coupons with static stress superimposed revealed that static stress was synergic with cyclic corrosion exposure, since the combination induced a change in the adhesive layer failure mechanism: from cohesive (through the adhesive layer) failure to adhesive failure (along the adhesive-metal interface). The adhesive failure served to create regions of exposed metal substrate in area A, which, in turn, became potential sites for corrosion. However, under this condition, the metal substrate in area A was more resistance to corrosion than area B due to the lack of plastic deformation in this region.

In this work, conclusions (3), (4) and (7) do not agree with the research hypothesis that cyclic deformation works in combination with cyclic corrosion conditions (Ford L-3190 testing protocol) to increase the susceptibility of coated hem flange coupons to localized corrosion damage. The current conclusions suggest that the localized corrosion damage took place independent of the cyclic deformation condition.

It is recommended that future work on this topic employ a stronger corrosion environment or a longer exposure duration, as the current work did not produce significant corrosion damage comparable to the field corrosion damage. In addition, cyclic corrosion-cyclic deformation *in situ* can be conducted in future work. Doing so will enable a better simulation of the real world condition where the automotive hem flange is subject to corrosive environment and cyclic deformation simultaneously.

References

[1] L. C. Lau, K. L. Lee and A. R. Mohamed, "Global warming mitigation and renewable energy policy development from the Kyoto Protocol to the Copenhagen Accord—A comment," *Renewable and Sustainable Energy Reviews,* vol. 16, no. 7, pp. 5280-5284, 2012.

[2] S. C. Davis, S. W. Diegel and R. G. Boundy, Transportation Engery Data Book, 33rd ed., Oak Ridge, TN: Oak Ridge National Laboratory, 2014.

[3] I. N. Fridlyander, V. G. Sister, O. E. Grushko, V. V. Berstenev, L. M. Sheveleva and L. A. Ivanova, "Aluminum Alloys: Promising Materials in the Automotive Industry," *Metal Science and Heat Treatment,* vol. 44, no. 9-10, pp. 365-369, 2002.

[4] S. Birch, "Aluminium spaceframe technology," *Automotive Engineering,* vol. 102, no. 1, pp. 8-12, 1994.

[5] W. S. Miller, L. Zhuang, J. Bottema, A. J. Wittebrood, P. De Smet, A. Haszler and A. Vieregge, "Recent development in aluminium alloys for the automotive industry," *Materials Science and Engineering A,* vol. 280, pp. 37-49, 2000.

[6] Y. L. Ji, F. A. Guo and Y. F. Pan, "Microstructural characteristics and paint-bake response of Al-Mg-Si-Cu alloy," *Transactions of Nonferrous Metals Society of China,* vol. 18, pp. 126-131, 2008.

[7] Y. Birol, "Pre-aging to improve bake hardening in a twin-roll cast Al–Mg–Si alloy," *Materials Science and Engineering A,* vol. 391, pp. 175-180, 2005.

[8] J. E. Janse, L. Zhuang, J. Mooi and P. De Smet, "Evaluation of the Effect of Cu on the Paint Bake Response of Preaged AA6xxx," *Materials Science Forum,* Vols. 396-402, pp. 607-612, 2002.

[9] "Automotive Body in White Concept," aluMATTER, [Online]. Available: http://dev.aluminium.matter.org.uk/content/html/eng/default.asp?catid=199&pageid=2144416949. [Accessed Aug. 2016].

[10] A. Muderrisoglu, M. Murata, M. A. Ahmetoglu, G. Kinzel and T. Altan, "Bending, flanging, and hemming of aluminum sheet-an experimental study," *Journal of Materials Processing Technology,* vol. 59, pp. 10-17, 1996.

[11] H. Livatyali, A. Müderrisoğlu, M. Ahmetoğlu, N. Akgerman, G. L. Kinzel and T. Altan, "Improvement of hem quality by optimizing flanging and pre-hemming operations using computer aided die design," *Journal of Materials Processing Technology,* vol. 98, no. 1, pp. 41-52, 2000.

[12] Z. Hamedon, K. Mori and Y. Abe, "Fatigue strength of high strength steel sheets joined by hemming process," *Applied Mechanics and Materials ,* Vols. 773-774, pp. 282-286, 2015.

[13] C. S. Adderley, "Adhesive Bonding," *Materials & Design,* vol. 9, no. 5, pp. 287-293, 1988.

[14] R. Bach, "Aluminum in transport," 2015. [Online]. Available: http://www.aluminiumleader.com/application/transport/. [Accessed 9 2016].

[15] T. Norton, Private Communication, Sept. 3, 2016.

[16] R. A. Rodríguez-Diaz, J. Uruchurtu-chavarín, A. M. Cotero-Villegas, S. Valdez and J. A. Juárez-Islas, "Corrosion Behavior of AlMgSi Alloy in Aqueous Saline Solution," *International Journal of Electrochemical Science,* vol. 10, pp. 1792 - 1808, 2015.

[17] S. K. Kairy, P. A. Rometsch, K. Diao, J. F. Nie, C. H. J. Davies and N. Birbilis, "Exploring the Electrochemistry of 6xxx Series Aluminum Alloys as a Function of Si to Mg Ratio, Cu Content, Ageing Conditions and Microstructure," *Electochimica Acta,* vol. 190, pp. 92-103, 2016.

[18] R. K. Gupta, N. L. Sukiman, K. M. Fleming, M. A. Gibson and N. Birbilis, "Electrochemical Behavior and Localized Corrosion Associated with Mg2Si Particles in Al and Mg Alloys," *ECS Eletrochemical Letters,* vol. 1, no. 1, pp. C1-C3, 2012.

[19] A. Bautista, "Filiform corrosion in polymer-coated metals," *Progress in Organic Coatings,* vol. 28, pp. 49-58, 1996.

[20] J. R. Davis, Corrosion of Aluminum and Aluminum Alloys, Materials Park, OH: ASM International, 1999.

[21] E. Ghali, Corrosion Resistance of Aluminum and Magnesium Alloys: Understanding, Performance, and Testing, Hoboken, New Jersey: John Wiley & Sons, Inc., 2010.

[22] S. P. A., Atmospheric Degradation and Corrosion Control, New York: Marcel Dekker Inc. Press, 1999.

[23] M. K. and T. H., Handbook of Diesel Engines, Berlin: Springer-Verlag GmbH, 2010.

[24] P. M. Natishan and W. E. O'Grady, "Chloride Ion Interactions with Oxide-Covered Aluminum Leading to Pitting Corrosion: A Review," *Journal of The Electrochemical Society,* vol. 161, no. 9, pp. C421-C432, 2014.

[25] N. LeBozec, N. Blandin and D. Thierry, "Accelerated corrosion tests in the automotive industry: A comparison of the performance towards cosmetic corrosion," *Materials and Corrosion,* vol. 59, no. 11, pp. 889-894, 2008.

[26] "ASTM B117-16 Standard Practice for Operating Salt Spray (Fog) Apparatus," ASTM International, West Conshohocken, PA, 2016, http://dx.doi.org/10.1520/B0117-16.

[27] "ASTM G85-11 Standard Practice for Modified Salt Spray (Fog) Testing," ASTM International, West Conshohocken, PA, http://dx.doi.org/10.1520/G0085-11, 2011.

[28] W. J. Liang, P. A. Rometsch, L. F. Cao and N. Birbilis, "General Aspects Related to the Corrosion of 6xxx Series Aluminum Alloys: Exploring the Influence of Mg/Si Ratio and Cu," *Corrosion Science,* vol. 76, pp. 119-128, 2013.

[29] E. H. Hollingsworth and H. Y. Hunsicker, Metals Handbook, 9th edition, Vol. 2, edited by D. Benjamin, Materials Park, OH: ASM International, 1979.

[30] H. Bohni, Uhlig's Corrosion Handbook, edited by R. W. Revie, Hoboken, NJ: John Wiley & Sons, Inc., 2000.

[31] H. Kaesche, Pitting Corrosion of Aluminum and Intergranular Corrosion of Aluminum Alloys, edited by R. Staehle, B. F. Brown, J. Kruger, and A. Agrawal., Houston, TX: NACE International, 1974.

[32] A. E. Hughes, N. Birbilis, J. M. C. Mol, S. J. Garcia, X. Zhou and G. E. Thompson, Recent Trends in Processing and Degradation of Aluminium Alloys, Rijeka, Croatia: InTech d.o.o, 2011.

[33] N. Birbilis and R. G. Buchheit, "Electrochemical Characteristics of Intermetallic Phases in Aluminum Alloys: An Experimental Survey and Discussion," *Journal of The Eletrochemical Society,* vol. 152, no. 4, pp. B140-B151, 2005.

[34] N. LeBozec, D. Persson and D. Thierry, "In Situ Studies of the Initiation and Propagation of Filiform Corrosion on Aluminum," *Journal of The Electrochemical Society,* vol. 151, no. 7, pp. B440-B445, 2004.

[35] N. LeBozec, D. Persson, A. Nazarov and D. Thierry, "Investigation of Filiform Corrosion on Coated Aluminum Alloys by FTIR Microspectroscopy and Scanning Kelvin Probe," *Journal of the Electrochemical Society,* vol. 149, no. 9, pp. B403-B408, 2002.

[36] X. Zhou, G. E. Thompson and G. M. Scamans, "The influence of surface treatment on filiform corrosion resistance of painted aluminium alloy sheet," *Corrosion Science,* vol. 45, pp. 1767-1777, 2003.

[37] M. H. M. Huisert, E. P. M. Van Westing, J. H. W. De Wit and L. Katgerman, Corrosion and Corrosion Prevention of Low Density Metals and Alloys, edited by edited by B. A. Shaw, R. G. Buchheit, J. P. Moran, Pennington, NJ: The Electrochemical Society, Inc., 2000.

[38] H. Leth-Olsen and K. Nisancioglu, "Filiform corrosion of aluminium sheet. I. corrosion behaviour of painted material," *Corrosion Science,* vol. 40, no. 7, pp. 1179-1194, 1998.

[39] F. Eckermann, T. Suter, P. J. Uggowitzer, A. Afseth and P. Schmutz, "The influence of MgSi particle reactivity and dissolution processes on corrosion in Al–Mg–Si alloys," *Electrochimica Acta,* vol. 54, pp. 844-855, 2008.

[40] R. K. Gupta, N. L. Sukiman, K. M. Fleming, M. A. Gibson and N. Birbilis, "Electrochemical Behavior and Localized Corrosion Associated with Mg2Si Particles in Al and Mg Alloys," *ECS Eletrochemical Letters,* vol. 1, no. 1, pp. C1-C3, 2012.

[41] G. Svenningsen, J. E. Lein, A. Bjørgum, J. H. Nordlien, Y. Yu and K. Nisancioglu, "Effect of low copper content and heat treatment on intergranular corrosion of model AlMgSi alloys," *Corrosion Science,* vol. 48, pp. 226-242, 2006.

[42] A. K. Bhattamishra and K. Lal, "Microstructural studies on the effect of Si and Cr on the intergranular corrosion in Al–Mg–Si alloys," *Materials & Design,* vol. 18, pp. 25-28, 1997.

[43] G. Svenningsen, M. H. Larsen, J. H. Nordlien and K. Nisancioglu, "Effect of thermomechanical history on intergranular corrosion of extruded AlMgSi(Cu) model alloy," *Corrosion Science,* vol. 48, p. 3969–3987, 2006.

[44] S. K. Kairy, T. Alam, P. A. Rometsch, C. H. J. Davies, R. Banerjee and N. Birbilis, "Understanding the Origins of Intergranular Corrosion in Copper-Containing Al-Mg-Si Alloys," *Metallurgical and Materials Transactions A,* vol. 47, no. 3, p. 985–989, 2016.

[45] Y. Huang, Y. Li, Z. Xiao, Y. Liu, Y. Huang and X. Ren, "Effect of homogenization on the corrosion behavior of 5083-H321 aluminum alloy," *Journal of Alloys and Compounds,* vol. 673, pp. 73-79, 2016.

[46] M. Abdulstaar, M. Mhaede, M. Wollmann and L. Wagner, "Investigating the effects of bulk and surface severe plastic deformation on the fatigue, corrosion behaviour and corrosion fatigue of AA5083," *Surface & Coatings Technology,* vol. 254, pp. 244-251, 2014.

[47] P. Von Der Hardt and H. Röttger, Neutron Radiography Handbook, Dordrect, Holland: D. Reidel Publishing Co., 1981.

[48] "ASTM E748-16 Standard Guide for Thermal Neutron Radiography of Materials," ASTM International, West Conshohocken, PA, 2016, http://dx.doi.org/10.1520/E0748-16.

[49] J. D. Minford, Handbook of Aluminum Bonding Technology and Data, New York, NY: Marcel Dekker, Inc., 1993.

[50] P. Vontobel, E. Lehmann and G. Frei, "Neutrons for the study of adhesive connections," in *16th World Conference on Nondestructive Testing*, 2004.

[51] A. R. Reddy and M. V. N. Rao, "Neutron Radiography," *Defence Science Journal,* vol. 32, no. 3, pp. 259-273, 1982.

[52] H. U. Mast, T. Brandler, E. Knorr and P. Stein, Nondestructive Characterization of Materials: Proceedings of the 3rd International Symposium Saarbrücken, Berlin: Springer-Verlag GmbH, 1988.

[53] S. Ebnesajjad and A. H. Landrock, Adhesives Technology Handbook, 3rd edition, London: Elsevier Inc., 2015.

[54] G. T. Herman, Fundamentals of Computerized Tomography: Image Reconstruction from Projections, London: Springer-Verlag London Ltd, 2012.

[55] "ASTM E1441-11 Standard Guide for Computed Tomography (CT) Imaging," ASTM International, West Conshohocken, PA, 2011, http://dx.doi.org/10.1520/E1441-11.

[56] J. L. Paris, F. A. Kamke, R. Mbachu and S. K. Gibson, "Phenol formaldehyde adhesives formulated for advanced X-ray imaging in wood-composite bondlines," *Journal of Materials Science,* vol. 49, no. 2, p. 580–591, 2014.

[57] J. Banhart, Advanced Tomographic Methods in Materials Research and Engineering, Oxford: Oxford University Press, 2008.

[58] A. J. Kinloch, Adhesion and Adhesives: Science and Technology, London: Chapman & Hall, 1987.

[59] M. R. Bowditch and K. J. Stannard, "Adhesive bonding of GRP," *Composites,* vol. 13, no. 3, pp. 298-304, 1982.

[60] S. G. Prolongo and A. Urena, "Durability of Aluminium Adhesive Joints Bonded with a Homopolymerised Epoxy Resin," *The Journal of Adhesion,* vol. 83, p. 1–14, 2007.

[61] S. Popineau and M. E. R. Shanahan, "Simple model to estimate adhesion of structural bonding during humid ageing," *International Journal of Adhesion & Adhesives,* vol. 26, p. 363–370, 2006.

[62] R. A. Gledhill and A. J. Kinloch, "Environmental Failure of Structural Adhesive Joints," *Journal of Adhesion,* vol. 6, pp. 315-330, 1974.

[63] V. Poulain, J. P. Petitjean, E. Dumont and B. Dugnoille, "Pretreatments and filiform corrosion resistance of cataphoretic painted aluminium characterization by EIS and spectroscopic ellipsometry," *Electrochimica Acta,* vol. 41, no. 7-8, pp. 1223-1231, 1996.

[64] R. G. Buchheit, "Corrosion Resistant Coatings and Paints," in *Handbook of Environmental Degradation of Materials, edited by Myer Kutz*, Delmar, NY, Myer Kutz Associates, Inc., 2005, pp. 367-387.

[65] J. Forsmark, Private Communication, Sept. 1, 2014.

[66] J. Forsmark, Private communication, Sept. 3, 2016.

[67] "International Alloy Designations and Chemical Composition Limits for Wrought Aluminum and Wrought Aluminum Alloys," The Aluminum Assosiation, Arlington, VA, 2015. www.aluminum.org/sites/default/files/TEAL_1_OL_2015.pdf.

[68] "ASTM G5-14(2014) Standard Reference Test Method for Making Potentiodynamic Anodic Polarization Measurements," ASTM International, West Conshohocken, PA, 2014. http://dx.doi.org/10.1520/G0005-14.

[69] "ASTM E748-16(2016) Standard Guide for Thermal Neutron Radiography of Materials," ASTM International, West Conshohocken, PA, 2016, http://dx.doi.org/10.1520/E0748-16.

[70] B. L. MacDonald, J. Vanderstelt, J. O'Meara and F. E. McNeill, "Non-destructive investigation of a time capsule using neutron radiography and X-ray fluorescence," *Nuclear Instruments and Methods in Physics Research B,* vol. 367, pp. 46-52, 2016.

[71] "ASTM E1441-11(2011), Standard Guide for Computed Tomography (CT) Imaging," ASTM International, West Conshohocken, PA, 2011, http://dx.doi.org/10.1520/E1441-11.

[72] "ASTM B117-16(2016) Standard Practice for Operating Salt Spray (Fog) Apparatus," ASTM International, West Conshohocken, PA, 2016, http://dx.doi.org/10.1520/B0117-16.

[73] L. K. Huang and M. J. Wang, "Image thresholding by minimizing the measure of fuzziness," *Pattern Recognition,* vol. 28, no. 1, pp. 41-51, 1995.

[74] E. Ghali, Uhlig's Corrosion Handbook, 2nd edition, edited by R. W. Revie., Hoboken, NJ.: John Wiley & Sons, Inc., 2000, pp. 677–715..

[75] B. W. Lifka, Corrosion Tests and Standards: Application and Interpretation,2nd edition, edited by Robert Baboian, West Conshohocken, PA: ASTM International, 2005.

[76] J. D. Bryant, "The effects of preaging treatments on aging kinetics and mechanical properties in AA6111 aluminum autobody sheet," *Metallurgical and Materials Transactions A,* vol. 30, no. 8, pp. 1999-2006, 1999.

[77] "ISO 11997-1 Determination of resistance to cyclic corrosion conditions — Part 1: Wet (salt fog)/dry/humidity," International Organization for Standardization, Geneva, Switzerland, 2005.

[78] D. M. Brewis, J. Comyn and J. L. Tegg, "The durability of some epoxide adhesive-bonded joints on exposure to moist warm air," *Interantional Journal of Adhesion and Adhesives,* vol. 1, no. 1, pp. 36-39, 1980.